FAST PHOTOMETRIC IMAGING OF HIGH ALTITUDE OPTICAL FLASHES ABOVE THUNDERSTORMS

A DISSERTATION
SUBMITTED TO THE DEPARTMENT OF APPLIED PHYSICS
AND THE COMMITTEE ON GRADUATE STUDIES
OF STANFORD UNIVERSITY
IN PARTIAL FULFILLMENT OF THE REQUIREMENTS
FOR THE DEGREE OF
DOCTOR OF PHILOSOPHY

By
Christopher Paul Barrington-Leigh
September 2000

I certify that I have read this dissertation and that in my opinion it is fully adequate, in scope and quality, as a dissertation for the degree of Doctor of Philosophy.

Umran S. Inan
(Principal Advisor)

I certify that I have read this dissertation and that in my opinion it is fully adequate, in scope and quality, as a dissertation for the degree of Doctor of Philosophy.

Sebastian Doniach

I certify that I have read this dissertation and that in my opinion it is fully adequate, in scope and quality, as a dissertation for the degree of Doctor of Philosophy.

Martin Walt

Approved for the University Committee on Graduate Studies:

With respect for all those who have chosen less selfish pursuits than the study of upper atmospheric physics.

Abstract

Lightning in the Earth's troposphere is among the largest impulsive energy sources within the bounds of the magnetosphere, and with 50 to 100 cloud-to-ground discharges per second globally, provides a steady source of electrodynamic excitation. Lightning effects on the magnetosphere in the form of whistler-mode waves have been recognized for decades, and whistlers are known also to cause lightning electron precipitation in the ionosphere. Recently, however, a range of spectacular and more immediate lightning effects on the lower ionosphere and the mesosphere have been discovered. These were first detected by very low frequency (VLF) radio remote sensing, which inspired studies of possible optical effects at about the same time as two fortuitous discoveries in 1989 and 1990 revealed remarkable visual evidence of direct electrodynamic coupling between lightning and the upper atmosphere [*Franz et al.*, 1990; *Boeck et al.*, 1992]. These new phenomena were soon to be called "sprites" and "elves."

A novel photometric array with a high-speed triggered data acquisition system, bore-sighted image-intensified CCD video camera, and VLF radio receiver was built to detect a predicted signature of elves, the lower ionospheric (80 to 95 km altitude) flash due to heating by an impinging electromagnetic pulse launched by intense lightning currents. The narrow individual photometer fields-of-view of ($2.2^\circ \times 1.1^\circ$) provide a spatial resolution of ~20 km at a range of 500 km, enabling the documentation of rapid expansion occurring over a horizontal range of 200 km with a time resolution of ~15 μs [*Inan et al.*, 1997].

In 1997 data acquired by the array (named the "Fly's Eye") settled several questions regarding the relationship between elves and lightning and, by measuring the spatial extent of ionospheric heating and the frequency of occurrence of elves, demonstrated their significance in causing sustained and cumulative modification of the nighttime lower ionospheric electron density profile over large thunderstorm systems [*Barrington-Leigh and Inan*, 1999].

The Fly's Eye, along with a telescopic imaging system developed in 1998 [*Gerken et al.*, 2000], was also used to investigate sprites. Sprites are highly structured discharges lasting 5 to 100 ms and extending from 40 to 85 km altitude which result from intense electric fields following a major redistribution of electric charge in the troposphere — usually a positive cloud-to-ground return stroke. Photometric, video, and radio (30 Hz to 20 kHz) measurements were used to detect the first sprites directly associated with negative cloud-to-ground lightning, implying a breakdown process that can propagate in upward and downward electric fields; this is consistent with only a subset of the theoretical descriptions for sprites [*Barrington-Leigh et al.*, 1999a]. In addition, telescopic imagery shows clear evidence of both positive and negative corona streamer propagation in a sprite.

Detailed electromagnetic (finite difference time domain) modeling of both elves and sprites is used to interpret observations. Three events recorded by a high-speed (3000 frames per second) imaging system in 1997, combined with modeling results, led to the recognition of a widespread confusion in interpreting video signatures of elves and sprites and identified for the first time the diffuse upper portion of sprites, a hard-to-measure but likely ubiquitous form of heating and ionization in the upper mesosphere which is now called the sprite halo [*Barrington-Leigh et al.*, 2000].

Acknowledgements

How can I adequately thank everyone who has made the past five years the most fun period of my life? I truly could not have asked for a better advisor. Umran has been open, thoughtful, understanding, accessible, patient, and unendingly enthusiastic, besides his intellectual talents.

I have had especially rich interactions with Mark Stanley. Data taken while working together at Langmuir Laboratory, as well as Mark's own measurements analyzed collaboratively, form a major part of the work in this dissertation. In addition, Mark's knowledge of lightning and thunderstorm processes were very valuable to me, and we have enjoyed many sprite-related discussions.

I am very grateful to Victor Pasko for his exceptionally wide-open door and for the many exciting and illuminating discussions I've had with him. It has been a great privilege to be working so close to the preeminent theorist in our field, and many of the ideas presented in this work follow from Victor's research and what I have learned from him.

I would like to extend thanks to another coauthor, Steve Cummer, for his help with ELF current determination, for insightful discussions, for taking me mountain biking, and just for his outstanding contributions to this field. I am also grateful to Martin Füllekrug for sharing his superb ULF data, and for useful (email) conversations. Steve Reising has also extended valuable advice to me on numerous occasions, for which I am very grateful.

My thanks and respect go out to Jack Winckler at the University of Minnesota for his visit and consultation in designing the Fly's Eye. Rick Rairden has been consistently generous and outgoing in helping our efforts. He provided the camera each year of the Fly's Eye operation, as well as a calibrated light source on more than one occasion. Gary Swenson and Stephen Mende also both contributed to the Fly's Eye experiment through helpful discussion.

Ken Cummins of Global Atmospherics Inc. provided NLDN data, and the Astronomical Data Center's stellar database was used for interpreting star fields. Also, I am indebted to the Langmuir Laboratory for excellent support and the use of their facilities.

Elizabeth Gerken fielded the telescopic imager, and operated the Fly's Eye during observations on 6 August 1998. I am indebted to Sean Hansen for his outstanding diligence in operation of the juvenile Fly's Eye during the summer of 1996.

Working in a group with such a rich history in magnetospheric physics has been a joy. Inspiring and fascinating discussions with Don Carpenter, Bob Helliwell, Bill Trabucco, and many others from the group will remain strong in my memory. I am grateful for help from Jerry Yarbrough and from many of the students with whom I have overlapped in the VLF group, and for the support of many others in the community. I would also like to thank Martin Walt and Seb Doniach for kindly serving on my reading committee.

The logistical support of Shao Lan Min and Paula Perron have each been invaluable, and I have greatly appreciated their invariant efficiency and friendliness.

I would like to thank Peter Dourmashkin for inspiring, investing in, and believing in me during my first year at M.I.T., and to Al Lazarus, Karolen Paularena, and the many dedicated teachers I had there for their help and love of physics and teaching.

I left Stanford on two occasions for highly enriching summer schools. For my time in Vienna I am indebted to the Canadian Foundation for the International Space University and all the inspired teachers and administrators at I.S.U., and for my time in Greenbelt I am grateful to NASA and especially Steve Zalesak at GSFC.

In addition, my two trips to Antarctica were each fun and beautiful beyond my expectation and dreams and I consider myself to have been superlatively fortunate in all the field work I have been able to undertake. I shall always remember seeing my first naked-eye sprite on 27 July, 1997. My scientific curiosity has long been founded in such natural beauty.

I have enjoyed constant love and support from Esther Mecking, my sister Rosalind, my mother Iris, my father John, and my brothers Robert and Stephen. My family has been my biggest gift in life. Esther has my special gratitude for encouraging me to eat and sleep regularly, and exercise occasionally, during the six weeks prior to my defence.

I am most grateful to all my friends from the Stanford Outdoor Education Program and elsewhere who have helped to make my life whole and to keep me cognizant of the other two of Edward Teller's three questions. The wilds of California have been a constant inspiration; I am grateful to all those who have helped to preserve pieces of them.

This dissertation was brought to you by Matlab, Adobe Illustrator, and software that was built to work rather than to make money – LaTeX, Emacs, NoWeb, and Gnu's compiler for C++.

Christopher P. Barrington-Leigh
Stanford, California
September 22, 2000

This work was supported by the Office of Naval Research under grant N00014-94-1-0100 and AASERT grant N00014-95-1-1095 and by the National Science Foundation under grant ATM-9731170.

Contents

List of Figures

Chapter 1

Introduction

This work describes optical measurements of high altitude discharges which represent electrodynamic coupling between thunderstorms and the lower nighttime ionosphere of Earth. Over the last decade such processes have for the first time been studied extensively both experimentally and theoretically. These discharges occur high above the troposphere but overlie thunderstorm systems and are known to cause electron heating, modification of the electron density, and the production of optical emissions as a result of strong electric fields following lightning activity in the troposphere. Two distinct discharge mechanisms lead to detectable optical emissions in the lower ionosphere and correspond to two distinct optical phenomena, 'elves' and 'sprites.' In 'elves,' an electromagnetic pulse (EMP) launched by a cloud-to-ground (CG) lightning stroke impinges on the lower ionosphere, is partially absorbed, and causes optical emissions between 80 and 95 km altitudes over a horizontal region several hundred km wide and over a period of $\sim$1 ms. Sprites consist of longer lasting (up to $\sim$100 ms) emissions which may be highly structured and can extend from 40 to 85 km altitudes and over $\sim$10 km horizontally. Sprites occur in response to the intense electric fields developed in the high altitude, thin, conducting atmosphere following a major redistribution of electric charge in the troposphere — typically a positive cloud-to-ground lightning return stroke, which moves positive charge from a cloud to the Earth's surface.

Sprites and elves have sparked scientific interest in part as a result of their effect on the propagation of very low frequency (VLF) radio waves travelling between the ground and the ionosphere, their contribution to the natural radio frequency spectrum, their role in the global electric circuit, and their demonstration of a novel mechanism of coupling between atmospheric regions.

In this chapter some quantitative properties of cloud-to-ground lightning are outlined (Section 1.2) and an overview of the physical factors governing the existence of high altitude discharges is given in Section 1.3. We begin by mentioning some theoretical foundations.

1.1 Units and fundamental equations

The subject treated in this dissertation lends itself to analysis largely by classical electrodynamics. As a result, Maxwell's equations are fundamental to much of the theoretical discussion. The *Système Internationale* or "rationalized MKS" units are used throughout. In differential form, Maxwell's noble laws for electromagnetic fields are:

$$\nabla \cdot \mathbf{B} = 0 \tag{1.1}$$

$$\nabla \cdot \mathbf{E} = \frac{\rho}{\epsilon_0} \tag{1.2}$$

$$\nabla \times \mathbf{B} = \mu_0 \mathbf{J} + \mu_0 \epsilon_0 \frac{\partial \mathbf{E}}{\partial t} \tag{1.3}$$

$$\nabla \times \mathbf{E} = -\frac{\partial \mathbf{B}}{\partial t} \tag{1.4}$$

Here the permittivity of free space $\epsilon_0 = 8.854 \times 10^{-12}$ F m^{-1} and the permeability of free space $\mu_0 = 4\pi \times 10^{-7}$ H m^{-1} satisfy $c^{-2} = \epsilon_0 \mu_0$, where c is the speed of light in vacuum.

The force exerted on a non-relativistic charged particle of mass m and charge q due to these fields is given by the Lorentz force equation,

$$m \frac{\partial \mathbf{v}}{\partial t} = q(\mathbf{E} + \mathbf{v} \times \mathbf{B}). \tag{1.5}$$

Under conditions of high charged particle density and number, a group of charged particles takes on the properties of a plasma and may be described by its collective behavior. By defining a distribution function $f(\mathbf{r}, \mathbf{v}, t)$ describing the time-dependent occupation of phase space for each kind of charged particle, the Boltzmann equation

$$\frac{\partial f}{\partial t} + [\mathbf{v} \cdot \nabla_{\mathbf{r}}]f + \frac{q}{m}[(\mathbf{E} + \mathbf{v} \times \mathbf{B}) \cdot \nabla_{\mathbf{v}}]f = \left(\frac{\partial f}{\partial t}\right)_{\text{coll}} \tag{1.6}$$

follows from the Liouville theorem and is a fundamental point of departure for the study of plasma heating. In (1.6), $\nabla_{\mathbf{r}}$ and $\nabla_{\mathbf{v}}$ are gradient operators which act on the position and velocity spaces, respectively, of $f(\mathbf{r}, \mathbf{v}, t)$, and $\left(\frac{\partial f}{\partial t}\right)_{\text{coll}}$ is a term which accounts for all collisional changes to the distribution function.

1.2 Thunderstorms and cloud-to-ground lightning

The existence of liquid water in Earth's troposphere is primary among the special characteristics on this planet that are thought to have led to the development of complex life. One remarkable and still imperfectly understood [e.g., *Wettlaufer and Dash*, 2000] terrestrial process resulting from water's presence is the convective charge separation which causes thunderstorms. About 40,000 thunderstorms per day worldwide produce ~100 cloud-to-ground lightning flashes per second [*Chalmers*, 1967]. While these discharges have obvious impacts in the troposphere and to humanity, they also play a significant role in the global electric circuit. While lightning currents may flow with either an upward or downward electrical sense, ~90% of cloud-to-ground lightning has an upward current (i.e., negative charge moves from the cloud to the surface of the Earth), resulting in a steady net negative potential of the Earth with respect to the ionosphere and a steady fair-weather downward electric field at the surface of the Earth of ~100 V-m^{-1} [*Feynman et al.*, 1989, p. 9-3].

The return stroke of a cloud-to-ground discharge [*Uman*, 1987] lasts ~100 μs and generates the largest currents, brightest optical emissions, and peak radiated power of a lightning flash. Such currents are typically ~30 kA but may surpass 200 kA, and the radiated electromagnetic pulse may reach electric field amplitudes of 50 V-m^{-1} at a horizontal range of 100 km from the lightning [*Uman*, 1987, p. 110].

The largest amounts of charge transfer between cloud and ground occur on slower timescales. Following a return stroke, especially those of positive (downward current) cloud-to-ground flashes, "continuing current" flows on time scales of several to hundreds of milliseconds and may transfer more than 300 C of charge to ground [*Uman*, 1987, p. 200]. Large continuing currents in lightning are associated with the production of sprites [*Reising et al.*, 1996], as are storms with especially large reservoirs of charge, i.e., with large horizontal and vertical extent [*Lyons*, 1996]. Sprites are often recorded in association with mesoscale convective systems well over 100 km in horizontal extent [*Lyons*, 1996].

Sprites and elves have also for many years been reported in association primarily with large peak current positive cloud-to-ground flashes [e.g., *Lyons et al.*, 1998]. This particular association later proved to be an issue of misinterpretation (see Sections 4.2 and 5.1) in the case of elves, but sprites are still thought to occur most often in a downward electric field following one or more positive cloud-to-ground strokes. Detailed measurements of small samples of lightning suggest that nearly all positive strokes are followed by significant continuing current and that this current is an order of magnitude greater than that following negative strokes [*Uman*, 1987, p. 210]. This distinction may well be the sole reason for the predominant association of sprites with positive (rather than negative) discharges. The median charge transfer for positive cloud to ground discharges was found to be 80 C, with 5% of flashes lowering more than 350 C [*Uman*, 1987, p. 210].

The National Lightning Detection Network [NLDN; *Cummins et al.*, 1998b] analyzes radio pulses, or atmospherics (abbreviated to "sferics"), from cloud-to-ground lightning in and near the continental United States. The processed data specify the location to within ~300 m, the time of occurrence to within ~1 μs, and the peak current of each recorded stroke. These data not only facilitate real-time sprite hunting in the United States; they also are invaluable for providing lightning locations which help in the interpretation of video, photometric, and radio recordings of upper atmospheric discharges. However, the NLDN is only 80 to 90% efficient in detecting cloud-to-ground lightning, and the accuracy of reported peak currents has only been ascertained for values below 60 kA [*Cummins et al.*, 1998a,b].

1.3 Electrical environment of the nighttime upper atmosphere

In the mesosphere and the D region of the ionosphere the properties of the upper atmosphere begin their transition from those of a neutral gas to a those of a weakly ionized plasma, as the plasma frequency becomes significant compared with the effective electron-neutral collision frequency. This region has also sometimes been called the "ignorosphere" because of its inaccessibility to *in situ* measurements by either high-altitude aircraft or orbiting spacecraft, or to remote sensing by ground-based radar or top-side sounding. Use of sounding rockets, optical remote sensing through lidar or the photometric and imaging techniques described in this work, and VLF radio studies lend themselves to investigations of these awkward altitudes characterized by their relatively low ($\leqslant 5\times10^3$ cm^{-3}) electron densities.

Figure 1-1 compares frequencies and rates of some physical processes in the lower ionosphere. The vertical green line shows ω_c, the electron cyclotron frequency in the Earth's magnetic field. At 75 to 80 km, the nighttime electron density is similar to that of the solar wind at 1 AU. In great contrast to solar wind plasma, however, for altitudes up to ~70 km under ambient nighttime conditions, and up to 90 km under an applied electric field near the breakdown threshold (discussed below in Section 2.1), the effective collision frequency ν_{eff} for electrons is large compared to the cyclotron frequency. At night the electron number density is only 10^{-16} times the neutral density at 70 km and $<10^{-10}$ times at 90 km, and on timescales greater than 10 μs, the electrons are in thermal equilibrium with the neutrals, which are typically at <300 K. This region may thus be described as a cold, collisional, weakly ionized electron plasma.

Representative values of the nighttime electron density* (n_e) have been used in Figure 1-1. Shown in gray is the electron plasma frequency,

$$\omega_p = \sqrt{\frac{q_e^2 n_e}{\epsilon_0 m_e}} \tag{1.7}$$

where $-q_e$ and m_e are the charge and mass of the electron, respectively. In the D region, ω_p changes abruptly as a function of altitude over one wavelength for an electromagnetic wave of frequency similar to ω_p. For example, a radio wave of frequency 10 kHz has wavelength 30 km and thus sees an abrupt (i.e., over a spatial range $\ll$30 km) transition from essentially free space to the highly reflecting ionosphere (i.e., relatively high refractive index). Equivalently, the index of refraction μ for plane electromagnetic waves (ignoring collisions and the ambient magnetic field) is

$$\mu = \sqrt{\epsilon_0 \left(1 - \frac{\omega_p^2}{\omega^2}\right)}$$

and can be seen in this expression to change over less than one wavelength from $\sim$1 to 0 and then to an imaginary number. This sharpness accounts for the low-loss long distance propagation of VLF radio in the Earth-ionosphere cavity (Section 3.1). However, the effect of collisions greatly modifies the effective reflection height and causes some D region radio absorption (Section 2.1.5).

There are at least three different mechanisms by which thundercloud charge configurations may impose electric fields on the upper atmosphere. Thundercloud charging as a result of convective charge separation occurs on time scales of $\sim$100 s. (Research into the mechanisms of charge separation and into the nature of charge configurations in thunderstorms has been ongoing for decades.) Secondly, sudden and large changes in electrical currents may radiate electromagnetic fields in all directions. A primary example of such strongly radiating processes, at least in the frequency range of interest here, is the return stroke of cloud-to-ground lightning, whose radiation spectrum peaks with period 50 to 100 μs. Third, continuing currents flowing to ground through return stroke channels may redistribute large quantities of charge on time scales of $\sim$0.5 ms to $>$100 ms.

The low-frequency conductivity of the atmosphere determines whether the electric field due to these charge configuration changes in thunderstorms can penetrate to high altitudes. In the absence of significant magnetic fields ($\nabla \times \mathbf{B} = 0$), equation (1.3) along with the constitutive relation $\mathbf{J} = \sigma \mathbf{E}$ becomes

$$\frac{\partial \mathbf{E}}{\partial t} = -\frac{\sigma}{\epsilon_0} \mathbf{E} \tag{1.8}$$

indicating that an applied electric field locally relaxes exponentially with a time constant $\tau_{\mathrm{E}} = \epsilon_0/\sigma$, regardless of the complexities of conductivity gradients. Figure 1-1 shows this electric relaxation rate $\tau_{\mathrm{E}}^{-1} = \sigma/\epsilon_0$ due to the sum of the electron and ion conductivities, both under ambient conditions and with ambient electron density in the presence of an imposed electric field equal in magnitude to the conventional breakdown field E_k (see Section 2.1.4). These profiles are discussed further in Section 2.4.

From these simple considerations, some important phenomenological classifications of upper-atmospheric discharges can be presaged. Electric fields due to growing thundercloud charge configurations, which may involve charge centers of hundreds of coulombs [*Marshall et al.*, 1996] but which accumulate over time scales of many tens of seconds, do not affect altitudes much above the

---

*The International Reference Ionosphere can be found at: `http://nssdc.gsfc.nasa.gov/space/model/models/iri.html`

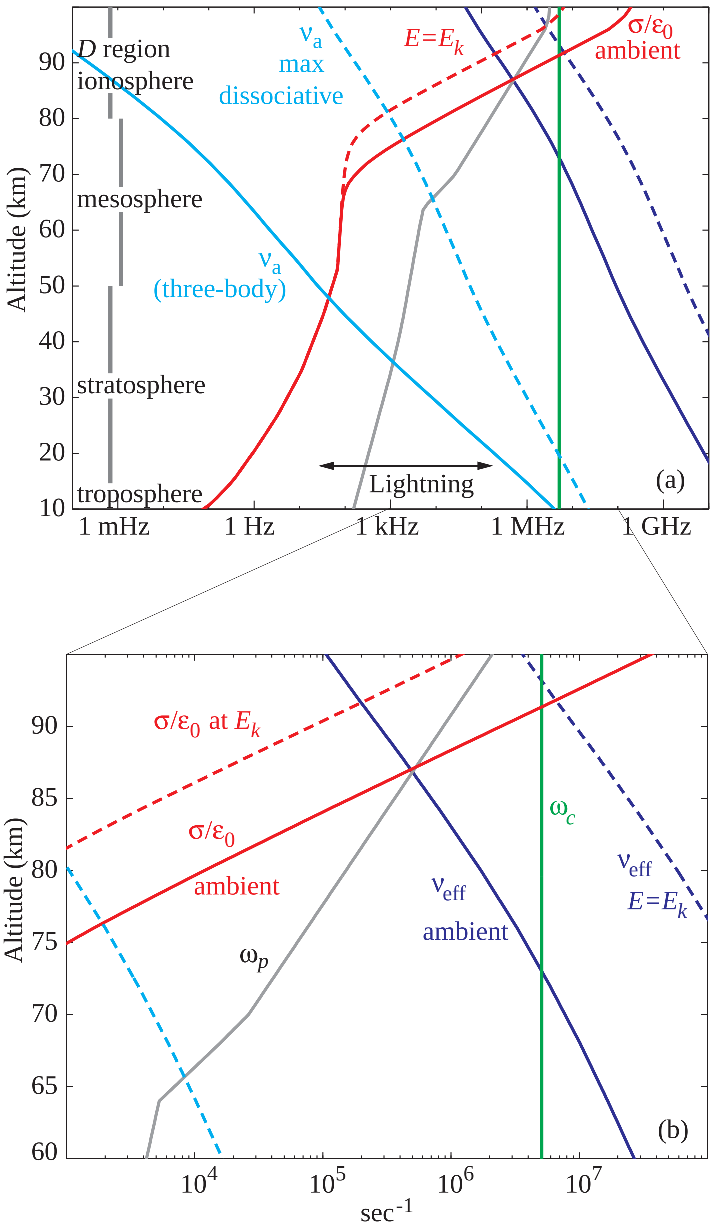

Figure 1-1: Important frequencies in the lower ionosphere. (a) Several characteristic frequencies between 50 and 100 km altitude. The red and gray curves show values for a "normal" nighttime ionosphere. In (b), the same values are shown with smaller axis ranges. ω_c is the electron cyclotron frequency, ω_p is the electron plasma frequency, ν_{eff} is the effective collision rate, ν_a is the attachment rate, and E_k is the conventional breakdown electric field (page 14).

troposphere. Space charge developed by currents flowing in accordance with equation (1.8) screen these fields from the thin upper atmosphere. In close vicinity to the tops of thunderclouds, however, such fields are thought to initiate upward streamer-like discharges which can propagate into the stratosphere; these have been denoted blue jets and blue starters [*Wescott et al.*, 1995; *Pasko et al.*, 1996a].

When these same thundercloud charge accumulations are partially neutralized or redistributed by lightning return strokes and their continuing currents on much faster timescales than those on which the charges are built up, the effects penetrate to much higher regions of the atmosphere. Because of the space charge that builds up in conjunction with thundercloud charge separation, the upper atmosphere sees an increase in electric field as a result of any sudden redistribution of charge, even if the new configuration causes reduced electric fields in the troposphere. For instance, a large positive cloud-to-ground return stroke may drain an extensive positive charge region of >100 C to the conducting Earth over 1 ms. On short time scales in the mesosphere, this is entirely equivalent to placing a negative charge of identical magnitude in the thundercloud. Considering the electric relaxation rates in Figure 1-1, a new charge configuration in the troposphere is effective in allowing the penetration of electric fields up to 85 km if the change occurs faster than ~1 ms, but only to 70 km if the change occurs on timescales on the order of $\leqslant$10 ms. This principle has been used in many theoretical studies of sprites (Section 2.3).

On even faster timescales, radiated electromagnetic fields at VLF frequencies may penetrate to a height[†] roughly determined by a comparison of their frequency with the time scale σ/ϵ_0. As discussed above, the electromagnetic pulse from lightning is largely reflected in the D region, but the penetration of these fields above the reflection height results, due to the finite conductivity, in heating of the electron population (Section 2.1.5). For strong radiated fields, this energy deposition can produce the phenomenon known as elves.

An important complication to the conclusions above results from the fact that the conductivity itself may change under an applied electric field. The isotropic conductivity due to electrons alone is $\sigma = |q_e| n_e \mu_e$, and the electron mobility $\mu_e = q_e \nu_{\text{eff}}^{-1} m_e^{-1}$ in turn is a decreasing function of the electric field. The application of an electric field heats the electron population (Section 2.1) and increases the collision frequency ν_{eff}, as shown in Figure 1-1 for a representative electric field value, E_k. Enhanced values of ν_{eff} in turn lead to the decrease of the mobility and thus the conductivity (Figure 1-1), thus allowing better penetration of transient electric fields to higher altitudes.

On the other hand, the electric field can also lead to the modification of the electron density n_e through impact ionization of the neutrals by accelerated electrons and through the enhancement of electron attachment to neutrals. For example, if $E > E_k$ then n_e increases, leading to enhanced conductivity and reversing the effect of heating described above. Ionization and heating effects both turn out to be of key importance in sprites and elves, hence the need arises for detailed modeling to account self-consistently for the nonlinear effect of an intense and varying electric field. Such modeling has now been carried out by several groups, as mentioned in Sections 2.2 and 2.3, and an electromagnetic model which accounts for these processes is described in Section 2.4.

Two more curves in Figure 1-1 require discussion. Under an appreciable electric field, the two-body reaction

$$\mathrm{O}_2 + e^- + 3.6\ \mathrm{eV} \longrightarrow \mathrm{O}^- + \mathrm{O} \tag{1.9}$$

is the dominant mechanism for the loss of free electrons. The rate ν_{a} of this “dissociative attachment” process exhibits a peak at an electric field value slightly below E_k, and the rate shown for ν_{a} in Figure 1-1 corresponds to its maximum. Under ambient electric field conditions, three-body

---

[†] In fact, despite the high electron density, they may couple all the way through the ionosphere as whistler-mode waves, evidence that the magnetization of the plasma does become significant at the upper altitudes shown in Figure 1-1.

attachment processes involving either O_2 and N_2 or two O_2 molecules dominate instead [*Glukhov et al.*, 1992], and also dominate over diffusion. As a result, it is the "three-body" rate shown in Figure 1-1 which defines the relaxation rate for ionization changes at high altitude following a discharge such as sprites or elves. For comparison, it may be noted that a typical time between lightning flashes in a given location in a storm is on the order of tens to >100 seconds, and a typical time between return strokes in a multiple-stroke flash is ∼40 ms [*Uman*, 1987, p. 14]. Therefore only above ∼80 km are ionization changes likely to accumulate from upper atmospheric discharges associated with successive lightning flashes. This possibility is discussed in Sections 2.5.3 and 4.4.

The intersection of the curves showing electric relaxation rate σ/ϵ_0 (a function of electron density) and maximum dissociative attachment rate ν_a (a function of neutral density) in Figure 1-1 also defines an important boundary for breakdown phenomena [*Pasko et al.*, 1998a]. Above this altitude (76 to 82 km) an applied electric field relaxes in accordance with equation (1.8) before much electron attachment can occur. Below this altitude the electric field relaxes slowly compared with the attachment rate; thus one can expect free electrons to be largely depleted (immobilized as negative ions) immediately after any transient electric field. As a result, any electron density enhancements are highly transient below ∼75 km. In addition, an electric field increasing in intensity on timescales comparable to the relaxation rate in this region causes a depletion of the free electron population before the electric field reaches its peak, so any resultant discharge process occurs in a gas nearly devoid of free electrons. This results in a diffuse region of sprites above 75 km and a streamer region below [*Pasko et al.*, 1998a], as observed in Section 5.1.

It may be concluded that the mesosphere and lower ionosphere is a region where both the average electron energy and the electron density may vary strongly in response to transient electric fields. The physics of discharges in a weakly ionized gas is treated more quantitatively in Section 2.1, and Section 3.1 further discusses low frequency radio propagation below the ionosphere.

1.4 Contributions

The major contributions of this dissertation are outlined below. The body of work described herein is primarily experimental, but Sections 2.4, 2.5, 3.2.1, 4.1.1, and parts of 5.1 also relate results from computer simulations and theoretical interpretations of observed phenomena.

1. A new technique for the remote sensing and identification of elves through optical and VLF signatures was developed. Motivated by the theoretical modeling of *Inan et al.* [1996c] and by a single observation of an elve from orbit [*Boeck et al.*, 1992], a new high-speed photometric array was designed and built. This instrument, named the "Fly's Eye," is described in Section 3.4 and records the output of 13 photometers with temporal resolution better than 30 μs, along with an image-intensified CCD video camera and a very low frequency (VLF) radio receiver. Deployed in the central United States during summer storm months each year from 1996 to 1999, the Fly's Eye was used to observe a predicted relationship between the VLF pulse radiated by lightning and the optical signatures of a briefly energized lower ionosphere. The discovery of this signature of elves, which also facilitates the location of the lower boundary of the optical flash, was reported by *Inan et al.* [1997] and is described in Section 4.1.2.

2. The empirical extent and prevalence of elves, and their relationship to causative lightning, was quantified for the first time. A number of theoretical studies have focused on horizontal intracloud currents [*Rowland et al.*, 1996] or currents in sprites [*Roussel-Dupre et al.*, 1998] as the cause for elves. In addition, until the execution of measurements reported in this dissertation, elves were reported to be associated primarily or only with positive cloud-to-ground lightning discharges. Chapter 4 reports experimental evidence, published in part by

Barrington-Leigh and Inan [1999], showing that observed elves were caused only by the return strokes of cloud-to-ground lightning, and with equal effectiveness by positive and negative discharges. In addition, a study of the spatial extent and frequency of this form of heating of the nighttime ionosphere's D region suggests the possibility for sustained or cumulative effects on the electron density at altitudes of ~80 to 95 km. Theoretical modeling described in Section 2.5.1 quantifies this effect.

3. A distinction between two observed classes of lower ionospheric optical flashes is detailed in Section 5.1 and published by *Barrington-Leigh et al.* [2000]. Modeling and new high time resolution video are used to point out a common misidentification made by many workers over the last ~5 years. Modeled emissions of the diffuse upper portion of sprites agree closely in form and timing with the diffuse flash seen frequently in intensified video and recently [*Barrington-Leigh et al.*, 2000] in a high speed imager. These "sprite halos," previously assumed to be signatures of elves, have implications for the frequency of sprite occurrence and may also be the cause of some "early/fast" VLF scattering events.

4. Using the Fly's Eye optical array to record the photometric signatures of sprites, a quantifiable feature of the optical relaxation of bright sprites is identified and related to the *in situ* electron density decay in Section 5.3. This result may form the basis for a possible new method of remote sensing mesospheric electron density changes and moreover may allow a determination of the *in situ* electric field.

Chapter 2

Direct Coupling Between Lightning and the Mesosphere/Lower Ionosphere

Lightning is known to have delayed effects on the lower ionosphere both in the vicinity of the lightning stroke and in the conjugate magnetic hemisphere as a result of energetic coupling to the magnetosphere in the form of whistler-mode waves. These waves may resonantly interact with trapped energetic electrons, scattering them in pitch angle and causing them to "precipitate" into the ionosphere, where they produce secondary ionization and thus alter the electron density 0.5 to 1 s after the lightning [*Lauben et al.*, 1999, and references therein]. This process, called lightning-induced electron precipitation, accounts for a class of perturbations in subionospherically propagating VLF signals and is considered to be an example of *indirect* coupling of lightning to the ionosphere.

In contrast, both sprites and elves involve *direct* modification of the electron population well above the troposphere by lightning-generated electric fields. This modification involves electron heating, electron density enhancement and depletion, and even propagation of filamentary waves of ionization in the tenuous upper atmosphere.

These processes are discussed below in Section 2.1. Sections 2.2 and 2.3 review the relevant theoretical and experimental literature concerning sprites and elves. Section 2.4 describes our own model for the electromagnetics, plasma heating, and optical emissions in sprites and elves, and Section 2.5 discusses the two-dimensional predictions of the model, including possible effects of the expected ionization changes. The model results are used in subsequent chapters to predict ground-based optical observations using three-dimensional geometry.

2.1 Electrical discharges in weakly ionized gases

In a weakly ionized gas, electron-neutral and electron-ion collisions greatly dominate over electron-electron collisions. As mentioned in Section 1.3, the electron densities encountered in this work are generally smaller than the neutral/ion density by a factor $>10^{10}$. The electric fields routinely found in models of sprites and elves would be adequate to completely ionize the gas if they were sustained for long enough, but they are necessarily transient. Indeed, the higher the electron density, the shorter can an electric field persist, as a result of enhanced conductivity σ and decreased relaxation time $\tau_{\mathrm{E}} = \epsilon_0/\sigma$.

Investigations pertaining to discharges in weakly ionized gases have historically focused on "glow discharges" in which the properties of the cathode and anode play an important role. These studies have been motivated largely by interest in high voltage insulators and, more recently, plasma processing. In the 1940's a theoretical understanding of a qualitatively different process, "streamer breakdown," emerged [*Bazelyan and Raizer*, 1998, p. 12]. In the following, generalizations applicable to the heating of an ionized gas under a moderate electric field are developed and related to high-altitude discharges. Section 2.1.5 applies some of these results to the absorption of a radio wave in a collisional and unmagnetized ionosphere.

2.1.1 Definitions

The meanings of "breakdown" and "discharge" are somewhat variable, and possibly unclear in a high-altitude context. *Bazelyan and Raizer* [1998] use "breakdown" to refer to the short-circuiting of some external voltage source. As such a consideration is not applicable to the case of lightning effects on the upper atmosphere, breakdown can alternately be defined as the "fast formation of a strongly ionized state under the action of applied electric or electromagnetic field" [*Bazelyan and Raizer*, 1998]. "Discharge" is a more general term describing the release of electric (or electromagnetic) energy into some medium.

In this section we discuss some semi-analytical considerations relating mostly to glow discharges. The complexities of the "spark" — comprising corona, streamer, leader, and arc processes — are still under considerable study. *Bazelyan and Raizer* [1998] provide a modern overview.

Below, we base our definitions of some important parameters on the most measureable macroscopic* quantities, namely the current density $\mathbf{J}$ (inferable from a total current), the electric field $\mathbf{E}$, the electron density n_e, and the neutral density N.

Since $\mathbf{J} \simeq -q_e n_e \mathbf{v}_d$, where $\mathbf{v}_d$ is the mean electron (drift) velocity, we define the electron mobility,

$$\mu_e \equiv \frac{|\mathbf{v}_d|}{|\mathbf{E}|} = \frac{|\mathbf{J}|}{|\mathbf{E}|} \frac{1}{q_e n_e}$$

in order that

$$\mathbf{v}_d = -\mu_e \mathbf{E}. \tag{2.1}$$

Here the approximation for $\mathbf{J}$ is to disregard both ion drift and (ambipolar) diffusion contributions to the current. These are small due to the mass ratio of electrons to molecular ions and due to the relatively rapid time scales of the processes considered.

In addition, we define an effective electron-neutral collision frequency ν_{eff}. Assuming no electron-electron or electron-ion ("Coulomb") collisions,† the force balance resulting in the net drift velocity $\mathbf{v}_d$ is the requirement that

$$\frac{d\mathbf{v}_d}{dt} = m_e \mathbf{v}_d \nu_{\text{eff}} - q_e \mathbf{E} = 0. \tag{2.2}$$

Here the effective collision frequency can be seen to be the rate at which the drift momentum is lost to collisions. Based on (2.2) and (2.1), we assign

$$\nu_{\text{eff}} \equiv \frac{q_e}{m_e \mu_e}. \tag{2.3}$$

This effective collision frequency ν_{eff} can be related to a more realistic frequency of collisions ν_{c} by assuming the collisions to be elastic. Then we may relate

$$\nu_{\text{c}} \equiv \frac{\nu_{\text{eff}}}{1 - \overline{\cos\theta}}, \tag{2.4}$$

---

[*] i.e., spatially averaged on a convenient scale which includes many electrons. n_e and $\mathbf{v}_d$ are of course directly defineable as moments of the electron distribution function.

[†] This proportionality of the conductivity to the electron density is in contrast to the behavior of a highly ionized plasma in which collisions between charged particles dominate, and the dependence of σ on n_e is lost [e.g., *Sturrock*, 1994, p. 176].

where $\overline{\cos\theta}$ represents the mean scattering angle cosine [*Bazelyan and Raizer*, 1998, p. 16]. Furthermore, in order to arrive at the sensible relation $\nu_\text{c} = N\overline{v}\sigma_\text{c}$, where the average "thermal" speed $\overline{v}$ is

$$\overline{v} \equiv \frac{1}{n_e}\int |\mathbf{v}| f(\mathbf{v})\mathrm{d}^\mathbf{3}\mathbf{v},$$

we define the collision cross section

$$\sigma_\text{c} \equiv \frac{\nu_\text{c}}{N\overline{v}}, \tag{2.5}$$

valid for $v_d \ll \overline{v}$.

In this way we may relate macroscopic observables to the fundamental calculable parameter σ_c and the electron distribution function $f(\mathbf{v})$. The latter, while conceptually fundamental, is not easily calculable from fundamental principles nor is it easily measureable; however, many macroscopic measurements may shed light on it.

Lastly, as a redundant parameter, the mean free path $\overline{\lambda}$ may be defined by

$$\overline{\lambda} \equiv \frac{1}{N\sigma_\text{eff}}, \tag{2.6}$$

where σ_eff is a convenient effective collision cross-section

$$\sigma_\text{eff} \equiv \sigma_\text{c}(1 - \overline{\cos\theta}). \tag{2.7}$$

2.1.2 Breakdown scaling laws

It remains to justify the assumption of a small drift velocity $\mathbf{v}_d$ in equation (2.5). In addition, we derive herein a fundamental scaling law and the time scale over which the electron distribution function thermalizes.[‡] Both in the following and preceding discussions, we ignore the weak velocity dependence of the scattering cross section, in order easily to deduce some approximate behaviors.

For an electron having an energy $\mathcal{E}$, a fraction δ of its energy is lost per effective collision. The rate of energy gain by the electron is thus the difference between the collision term $-\nu_\text{eff}\delta\mathcal{E}$ and that due to the electric field, $-q_e\mathbf{E}\cdot\mathbf{v}_d$, as long as $\delta \ll 1$. This condition remains to be justified below in the context of the following discussion for $\mathcal{E}\lesssim 3$ eV; however, if elastic collisions dominate the effective collision term, $\delta \simeq m_e/m_\text{air} \simeq 4\times10^{-5}$ for air [e.g., *Goldstein*, 1980, p. 118]. Using (2.1) and (2.3) for $\mathbf{v}_d$ we have

$$\frac{\mathrm{d}\mathcal{E}}{\mathrm{d}t} = \frac{q_e^2E^2}{m_e\nu_\text{eff}} - \nu_\text{eff}\delta\mathcal{E}. \tag{2.8}$$

Considering the ensemble average over all electrons to find $\overline{\mathcal{E}}$, the solution to (2.8) is

$$\overline{\mathcal{E}} = \frac{q_e^2E^2}{\delta m_e\nu_\text{eff}^2}\left(1 - \mathrm{e}^{-\delta\nu_\text{eff}t}\right) \tag{2.9}$$

for the initial condition $\overline{\mathcal{E}}=0$ at $t=0$.

Immediately apparent is the timescale

$$\tau_\text{th} = \frac{1}{\delta\nu_\text{eff}}$$

[‡] The electron distribution function reaches a thermal equilibrium with the neutral and ion population. This "thermal" distribution may not necessarily be a Maxwellian form.

over which the electron distribution function adjusts to a new electric field. Also, the final value of $\overline{\mathcal{E}}$ according to (2.9) is

$$\overline{\mathcal{E}} = \frac{q_e^2 E^2}{\delta m_e \nu_{\text{eff}}^2} = \Big(\frac{q_e}{\sigma_{\text{eff}}} \frac{1}{\sqrt{2\xi\delta}}\Big)\frac{E}{N} \tag{2.10}$$

where ξ is the proportionality between $\overline{v}^2$ and $\overline{v^2}$,

$$\overline{v}^2 = \xi \overline{v^2} \tag{2.11}$$

which is determined by the shape of the distribution function, and where we have used

$$\nu_{\text{eff}}^2 = (N\sigma_{\text{eff}}\overline{v})^2 = \xi \frac{2}{m_e} N^2 \sigma_{\text{eff}}^2 \overline{\mathcal{E}} \tag{2.12}$$

based on (2.3) to (2.7).

Equation (2.10) exhibits a key feature of electric discharges in a weakly ionized gas. Many discharge behaviors scale linearly as E/N, or for stronger fields as some other function of E/N. As a result, processes occurring in the relatively dilute upper atmosphere may be studied experimentally on smaller spatial scales by using stronger electric fields at atmospheric pressure.

For a Maxwellian distribution,

$$\xi = \frac{8}{3\pi}$$

and using (2.12) and values for ν_{eff} for E=E_k shown in Figure 1-1 on page 5, we obtain $\sigma_{\text{c}} \simeq 3\times 10^{-19}$ m^2, which varies weakly with energy. *Llewellyn-Jones* [1966, p. 43] reports an experimental mean electron energy of ~3.8 eV (>100 times ambient) in air for a value of E/N corresponding to an electric field of 10 V-m^{-1} at 90 km altitude. With these values in (2.10), we find δ=0.01 for this relatively strong heating case. While this value is several orders of magnitude larger than the value for elastic collisions, it is small enough to justify the assumptions made above for most of the electric field intensities expected to result in the mesosphere from lightning electromagnetic pulses.

To check whether $v_d \ll \overline{v}$, we use (2.1) and (2.3) to find $\mathbf{E} = -m\mathbf{v}_d\nu_{\text{eff}}/e$. With (2.11), (2.10) gives

$$\frac{v_d}{\overline{v}} = \sqrt{\frac{\delta}{2\xi}}, \tag{2.13}$$

which is small if $\delta \ll 1$.

Referencing Figure 1-1 again and using δ=0.01, we see that with $E \simeq E_k$ the thermalization time τ_{th} is ~10 μs at 90 km and much faster at lower altitudes. These simple considerations suggest that during heating driven at 90 km altitude by a <20 kHz electromagnetic pulse, the electron energy distribution is maintained essentially in equilibrium. However, at lower values of $\overline{\mathcal{E}}$ and δ, τ_{th} increases and may become slow compared with the electric field variation. This issue has been explored in detail and is discussed in Section 2.2.1. Using a detailed model for the electron distribution function, *Taranenko et al.* [1993a] found that an equilibrium mean energy of ~4.3 eV was reached in 10 μs for an electric field of 10 V-m^{-1} at 90 km altitude.

Lastly, we note that a pleasing form of (2.10) is obtained using (2.6):

$$\overline{\mathcal{E}} = \frac{q_e E \lambda}{\sqrt{2\xi\delta}}$$

showing that at "equilibrium" the average electron energy is nearly proportional to the energy $q_e E\lambda$ available from the electric field during a single inter-collision period.

2.1.3 Inelastic collisions

Following simply from the conservation of momentum and energy [e.g., *Goldstein*, 1980, p. 117] are the fundamental facts of classical mechanics:

- Two-body elastic (i.e., in which translational kinetic energy is conserved) collisions between particles of highly dissimilar mass are inefficient in transferring energy; the converse is true for particles of similar mass.
- An inelastic collision is efficient in transferring energy from a lighter particle to a heavier one if the collision is endothermic (i.e., if the reaction increases the potential energy of its constituents).
- A two-body exothermic (i.e., decreasing the potential energy) collision in which the product is a single particle is *impossible.*

As a result, on short timescales, ions and neutrals are in a separate thermal equilibrium from that of the electrons. The value $\delta \simeq m_e/m_{\text{air}}$ remains very small as long as only elastic collisions are accessible ($\mathcal{E}\leqslant 1.8$ eV), and the direct proportionality between $\overline{\mathcal{E}}$ and E/N from equation (2.10) remains strictly true. However, for $1.8<\mathcal{E}<3.3$ eV inelastic processes with N_2 become available, and for average energy $\overline{\mathcal{E}}>0.5$ eV, electrons lose $\gtrsim$90% of the energy gained from heating by an electric field to the excitation of molecular vibrations [*Bazelyan and Raizer*, 1998, p. 22]. For $\mathcal{E}$ in the range of 10 to 15 eV, electronic levels, which are largely responsible for optical emissions, are excited, and above 12.2 eV for O_2 and 15.6 eV for N_2, molecular ionization is possible. At these energies inelastic energy losses dominate over elastic ones and δ tends to 1, making modeling based on the simple considerations used in Section 2.1.2 essentially invalid.

Even for low enough electric fields such that the electron distribution function $f(\mathbf{v})$ remains highly isotropic ($v_d \ll \overline{v}$), an applied electric field can cause the shape of $f(v)$ to depart significantly from a Maxwellian. Because slower electrons participate only in elastic collisions (with inefficient energy transfer to neutrals) while energetic electrons may lose energy (or be attached) in inelastic processes, the high-speed end of the distribution can be greatly diminished as compared with a Maxwellian [*Chapman*, 1980, p. 124]. The resulting so-called Druyvesteyn distribution, in which $f(v) \propto \exp(-av^4)$ rather than the Maxwellian form of $f(v) \propto \exp(-av^2)$, has a steeper "tail" and has been often used in glow discharge studies [*Meek and Craggs*, 1978, p. 110]. However, a detailed calculation of the distribution function from the Boltzmann equation which takes into account an appropriate set of inelastic collisions may result in a slightly more complex and structured distribution, for instance that calculated by *Taranenko et al.* [1993a].

The dominant inelastic processes for energized electrons in weakly ionized air are ionization and electronic excitation of neutrals, as already mentioned above, and electron attachment to neutrals. As a result of the third classical mechanics fact listed above, electrons cannot combine with electronegative species such as O_2 or positive ions in a two-body collision. As a result, in order to recombine, cold electrons must undergo a three body collision such as

$$O_2 + e^- + A \longrightarrow O_2^- + A + 0.5 \text{ eV}, \tag{2.14}$$

where A is another neutral molecule. Only energetic electrons can overcome the 3.6 eV energy barrier of the dissocative attachment reaction (1.9). The fact that the rate of the three-body reaction (2.14) is slow (see Figure 1-1) has important ramifications for the persistence of ionization enhancements, as was also discussed on page 6 (Section 1.3).

2.1.4 Streamer breakdown and other energetic processes

In accordance with equation (2.10), the rate coefficients ν_a and ν_i for dissociative attachment and molecular ionization in an electrically heated ionized gas scale as a function of E/N. The electric field at which ν_i surpasses ν_a is known as the conventional breakdown electric field and denoted E_k; it follows that E_k is proportional to N. In a steady electric field above this threshold, $dn_e/dt > 0$ and, since the ionization rate is proportional to the electron density, n_e tends to increase exponentially. This electron avalanche process was first described by J. Townsend in 1910 [reprinted in *Rees*, 1973], and is applicable to all of the high altitude discharges modeled in this work. *Wilson* [1925] realized that at some altitude E_k would be less than the electric field due to the charge configuration in a thundercloud, as shown in Figure 2-1. He thus predicted an electrical breakdown and ensuing optical emissions.

At much higher electric fields or over long distances d and high neutral densities such that $Nd \gg 7\times10^{16}$ m^{-2}, air breakdown may occur instead in the form of (corona) streamers [*Bazelyan and Raizer*, 1998, p. 11] or for distances and durations adequate to significantly heat the neutral gas, in the form of leaders [*Bazelyan and Raizer*, 1998]. Streamers are ionization waves which can propagate as narrow channels through regions where $E<E_k$. This self-propagation is due to highly nonuniform electric fields which result from significant $\nabla \cdot \mathbf{J}$, or space charge. Streamer breakdown is not addressed in any detail in this work, but Section 2.3 provides references to recent overviews and to studies relating to sprites. Nevertheless, the issue of streamer initiation is addressed in the context of the observations presented in subsequent sections.

The requirements for streamer initiation have mostly been discussed in the context of spark-gap experiments. For instance, *Raizer et al.* [1998] and *Bazelyan and Raizer* [1998, p. 77] describe the critical number of avalanching electrons and a critical (minimum) radius of the avalanche region needed to transition from an avalanche to a streamer. Such considerations are appropriate for an avalanche starting from a narrow point and expanding in a gas of uniform density. In the case of sprites, streamers may sometimes form at the boundary of very large regions of enhanced ionization (Sections 2.5.1 and 5.1). *Raizer et al.* [1998] suggest that streamers in sprites are initiated by patches of electron temperature and density perturbations caused by the interference pattern from radiation due to complex horizontal intracloud lightning channels. An observed spatial association between a bulk discharge in the lower ionosphere and the formation of streamer channels is discussed in Section 5.1, and is not consistent with the proposal of *Raizer et al.* [1998].

Figure 2-1 shows electric field thresholds required for air breakdown as a function of altitude. Conventional breakdown occurs at $\sim$32 kV-cm^{-1} at ground level and follows the neutral density to $\sim$2 V-cm^{-1} at 70 km and $\sim$8 V-m^{-1} at 90 km altitude. Once a streamer is initiated, it may propagate in electric fields lower than E_k. As shown, positively charged streamers, which propagate parallel to the electric field, have a lower propagation threshold than negatively charged (antiparallel to $\mathbf{E}$) ones. The electric field threshold for runaway avalanche varies between the "relativistic" and "thermal" limits, and depends on the energy of available high-energy electrons. Above the relativistic runaway threshold, electrons with $\mathcal{E} > 1$ MeV do not thermalize because the electric force outweighs that due to collisions. At the thermal runaway threshold, this is true for electrons with $\mathcal{E} > 100$ eV, and above this threshold, it is true for all electrons. At tropospheric pressures streamers may develop into leaders, which can propagate in even lower electric fields than streamers can, due to thermal ionization of the neutral gas; lightning is an example. This leader development is seen to occur in electric fields greater than 1 kV/cm [*Bazelyan and Raizer*, 1998, p. 256]. This value does not scale simply with neutral density and leaders are not thought to occur at high altitudes [*Pasko et al.*, 1998a].

Also shown in Figure 2-1 is the electric field magnitude that would be observed in free space due to a charge of 200 C placed at 10 km altitude above a conducting ground. The field drops off with

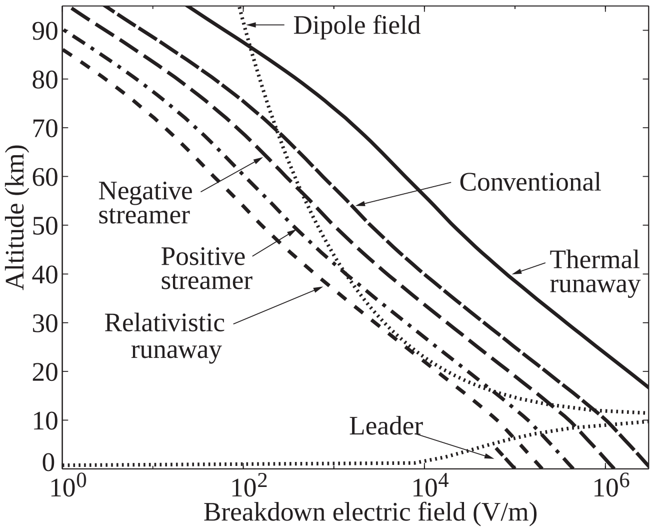

Figure 2-1: Electric field thresholds for air breakdown mechanisms. Breakdown electric field as a function of altitude is shown for conventional and relativistic runaway breakdown. In addition, minimum fields required for propagation of several discharge processes are shown.

altitude h as $\sim h^{-3}$ due to the dipole resulting from the single image charge. When combined with the electric relaxation times shown in Figure 1-1 and discussed in Section 1.3, these considerations point to three likely scenarios for breakdown in the mesosphere and lower ionosphere. Transient electric fields following large charge redistributions (>1000 C-km) in clouds may

1. initiate relativistic runaway breakdown above ~30 km (terrestrial gamma ray flashes) [*Lehtinen et al.*, 1999],
2. cause conventional breakdown above ~70 km with streamer propagation to much lower altitudes (sprites), and
3. launch radio pulses in the peak of the lightning spectrum around 15 kHz and having wave electric field strengths of ~20 V-m^{-1} at 70 km from the source [*Krider*, 1992; *Taranenko et al.*, 1993a], which may cause conventional breakdown at 90 km altitude (elves).

Experimental evidence for scenario (1) consists only of gamma radiation collected in orbit above thunderstorms [*Fishman et al.*, 1994; *Inan et al.*, 1996b; *Nemiroff et al.*, 1997]. For theoretical studies see *Lehtinen et al.* [1999] and references therein. Literature concerning scenarios (2) and (3) is discussed in Sections 2.2 and 2.3.

2.1.5 VLF absorption and reflection

The first term on the right hand side of Equation (2.8) on page 11 gives the power per electron lost by an electric field. Multiplying by the electron density gives the rate of loss of electric field energy density, and dividing by the total electric field energy density $u = \epsilon_0 E^2/2$ gives

$$\begin{aligned}\frac{1}{u}\frac{\partial u}{\partial t} &= -\frac{2}{\epsilon_0 E^2} n_e \frac{q_e^2 E^2}{m_e \nu_{\text{eff}}} \\ &= -\frac{2q_e^2}{\epsilon_0 m_e}\frac{n_e}{\nu_{\text{eff}}}.\end{aligned}$$

This value is the fractional rate of decrease of the electric field energy density due to 'ohmic' losses, i.e., losses due to the collisions of free electrons with neutrals. For an electromagnetic wave, this rate is significant in attenuating the wave electric field if it is fast compared to the wave frequency ω; that is, if

$$\frac{2q_e^2}{\epsilon_0 m_e}\frac{n_e}{\nu_{\text{eff}}} > \omega$$

the wave is largely absorbed by a collisional plasma, rather than propagating through it. In terms of the plasma frequency defined in equation (1.7), this condition is simply

$$2\frac{\omega_p^2}{\nu_{\text{eff}}} > \omega.$$

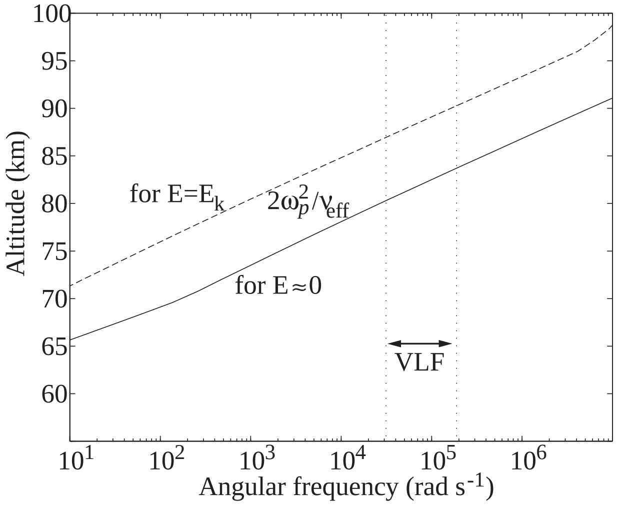

Figure 2-2: Ionospheric absorption. An electromagnetic wave is highly absorbed in a collisional, isotropic (unmagnetized) ionosphere where $2(\omega_p^2/\nu_{\text{eff}}) \simeq \omega$, an altitude known as the reflection height.

The value $2\omega_p^2/\nu_{\text{eff}}$ is plotted in Figure 2-2 using values of ν_{eff} both under ambient electric field and at $E = E_k$ (see Figure 1-1 on page 5). It can be seen that wave energy in the VLF frequency range, where the spectrum of lightning peaks, is largely absorbed over a very narrow altitude range. For low wave electric fields, this altitude is at 80 to 84 km, while for wave electric fields strong enough to cause a considerable ionization ($E \simeq E_k$), the altitude is near 87 to 90 km.

These conclusions take into account collisions not considered in the discussion on page 4 (Section 1.3), but still ignore the Earth's magnetic field. *Inan* [1990] discusses reflection and absorption of the ordinary and extraordinary wave modes using the index of refraction given in a full magnetoionic treatment [e.g., *Budden*, 1985].

2.2 Heating of the lower ionosphere by the lightning electromagnetic pulse: elves

Remarkably, both sprites and elves were predicted theoretically before they were scientifically documented through observation. In the case of elves, which lend themselves to relatively straightforward modeling but are difficult to observe and identify without highly specialized equipment, the theoretical literature is considerably more extensive than the experimental. Many of the studies are similar and provide only incremental advances or parallel model development between different research groups. Nevertheless, the progression of the theoretical literature is briefly outlined below, followed by a discussion of experimental reports. The early idea [*Inan et al.*, 1991] that optical flashes (now called elves) may result from molecular excitation due to a lightning electromagnetic pulse heating and increasing the electron population in the lower ionosphere has not varied among the majority of theoretical studies.

2.2.1 Theoretical studies of elves

Interest in the subject of the immediate effects of lightning electromagnetic pulses (EMPs) on the lower ionosphere arose in recent times in conjunction with VLF radio scattering studies rather than with optical phenomena. The first experimental evidence of detectable heating of ambient D region electrons by VLF waves was realized serendipitously [*Inan*, 1990], leading to the suggestion that VLF energy produced in lightning may heat the D region and produce optical emissions [*Inan et al.*, 1991]. The heating of the ambient electron population was calculated by *Inan et al.* [1991] and *Rodriguez et al.* [1992] in one and two dimensions, respectively, in order to assess whether resultant electron density enhancements could be sufficient to cause subionospheric VLF signal perturbations similar in amplitude to those seen in lightning electron precipitation events. This model assumed a Maxwellian distribution function for electrons, considered only elastic collisions in calculating electron heating, and calculated the effects of EMP-induced heating only in terms of a modified wave attenuation rate as given by the imaginary part of the refractive index. An estimate of ionization enhancements was made based on the final electron temperature, and these were found to be sufficient to affect VLF propagation. The possibility of airglow enhancement was mentioned [*Inan et al.*, 1991] and the shapes of affected ionospheric regions for horizontal and vertical lightning currents were assessed [*Rodriguez et al.*, 1992].

Taranenko et al. [1992] used the same model (in one spatial dimension) as *Inan et al.* [1991] to predict optical emissions from the EMP-ionosphere interaction. This work was motivated by the observations of *Boeck et al.* [1992], discussed below. *Taranenko et al.* [1992] compiled optical line excitation rates for atmospheric species, and suggested that the optical bands N_2(1P) and N_2(2P) in elves could be seen from the ground and should be measured using an instrument with 50 μs or better resolution. This instrument could be triggered by large lightning sferics.

The calculations published before 1993 did not properly treat the modified shape of the distribution function under an applied electromagnetic wave (or electric field), nor did they propagate the EMP using self-consistent solutions to Maxwell's equations in the presence of a nonlinearly varying conductivity. *Taranenko et al.* [1993a,b] developed an essentially modern description of the interaction of lightning EMP with the lower ionosphere, including its optical emissions, though in only one spatial dimension. A simplified Boltzmann equation was solved, including inelastic collisions, for an initially thermal (Maxwellian) weakly ionized plasma in a constant electric field. It was found that the electron distribution function attained a steady-state shape in $\sim$10 μs. Because an EMP electric field at 10 kHz varies slowly compared to 10 μs, "equilibrium" values of relevant physical parameters (current density, ionization and attachment rates, and optical excitation rates) from this calculation could be tabulated for various altitudes and electric field magnitudes for use in the simulation. The lightning EMP was propagated using Maxwell's equations and self-consistent (i.e., modified throughout the calculation) conductivity, allowing reflection and thus constructive interference of the wave electric field. Results from this model differed quantitatively from past work, and also showed the effects of two-body attachment, which in some regions lead to a decrease in the electron density below its ambient value (see Section 2.5.1). *Taranenko et al.* [1993a] also calculated (in one dimension) the cumulative ionization for multiple lightning strokes, a concept which was not addressed again until results described in this dissertation (Section 2.5.3).

Rowland et al. [1995] presented a similar model in two spatial dimensions to calculate ionization changes but using experimental swarm data rather than the results of a solved Boltzmann equation. Optical emissions were not considered and attachment processes were neglected, resulting in an overestimate of ionization changes in the lower ionosphere.

The next, and arguably the latest, major advance in modeling elves came from *Inan et al.* [1996c] who investigated the dynamics of the ionospheric optical emissions due to a vertical lightning current using a two-dimensional code and correctly predicted the rapid lateral expansion of the optical luminosity at 80 to 90 km altitudes. This study used Maxwell's equations self-consistently to propagate the EMP and, like *Rowland et al.* [1995], used experimental data for conductivity, ionization, and attachment rates. The results were also used to interpret the first ground-based optical detection of elves by *Fukunishi et al.* [1996b]. *Inan et al.* [1996c] and all subsequent works refer to the optical emissions from lightning EMP heating of the lower ionosphere as "elves."[§] This work was flawed by a limitation in the radial extent of the model, and thus of the resultant emissions. Nevertheless, its primary conclusions and the underlying physical process of elves as described therein have not changed since this publication, which inspired the development of the Fly's Eye (Section 3.4).

Rowland et al. [1996] used the *Rowland et al.* [1995] model to investigate elves due to horizontal and vertical lightning. They also noted the effect on elves of neutral density fluctuations due to atmospheric gravity waves.

Glukhov and Inan [1996] used a (Monte Carlo) particle code to assess the validity of the quasi-stationary distribution function used by *Taranenko et al.* [1993a,b] and the quasi-stationary assumption of those employing experimental swarm data. They confirmed that the electron distribution function relaxes rapidly enough in response to electric field changes to justify the assumptions in models using lightning current input with spectral content up to 50 kHz.

Sukhorukov et al. [1996] presented a similar Monte Carlo particle model, and similar conclusions. *Fernsler and Rowland* [1996] extended the *Rowland et al.* [1995] model to include the full Maxwell's equations and thus the effects of the static electric field from model lightning currents. *Inan et al.* [1997], an experimental paper, was the first to show modeled optical emissions as they would be seen from the ground. Model video and photometric array signatures were given and compared with observations. *Taranenko et al.* [1997] and *Roussel-Dupre et al.* [1998] both suggested that elves may be caused by sprites; in particular, *Roussel-Dupre et al.* [1998] suggested that a relativistic runaway mechanism may cause sprites, and the resultant forward-focused VLF radiation may cause elves. More recent calculations indicate that, on the contrary, radiation electric fields from the relativistic runaway process are small as compared with the thundercloud quasielectrostatic field [Nikolai Lehtinen, *private communication*, 2000]. *Rowland* [1998] reviewed the theoretical literature on elves to date.

Cho and Rycroft [1998] gave a two-dimensional fully electromagnetic model, like *Fernsler and Rowland* [1996], but included optical emissions. They presented extensive plots of brightness and

---

[§] The singular noun has come to be "elve" but may be pronounced as "elf". The odd spelling of the singular form is intended to discriminate it from the acronym, ELF.

power profiles. *Veronis et al.* [1999] provided a fully electromagnetic version of the model used by *Inan et al.* [1996c], including a larger grid extent and simulated views of optical emissions from the ground.

2.2.2 Experimental optical studies of elves

The first photometric recordings of elves may have occurred well before they were recognized or adequately discriminated. A number of studies have sought evidence of broad nighttime atmospheric light pulses caused by fluorescence from supernovae gamma-rays [e.g., *Charman and Jelley*, 1972; *Ogelman*, 1973] or other particle precipitation [*Li et al.*, 1991] and found more than one class of anomalous flash, some of which remain unexplained. *Nemzek and Winckler* [1989] reviewed the studies to date and explained those flashes of $\sim$1 ms duration as scattered light from lightning, based on their association with low frequency sferics in a new study. *Winckler et al.* [1993] further described the equipment used in this study and discussed the possibility that upper-atmospheric discharges may contribute to anomalous optical events.

The first unambiguous recording of elves is shown in Figure 2-3. *Boeck et al.* [1992] described this phenomenon as an "airglow brightening" and suggested the mechanism of *Inan et al.* [1991] as an explanation. This event was, however, rather unique among the Space Shuttle data.

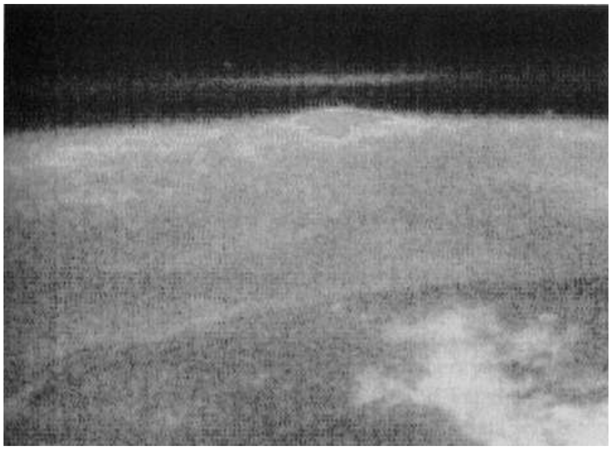

Figure 2-3: The first observed elve. Video image of "airglow brightening" taken from the Space Shuttle and reported by *Boeck et al.* [1992].

In 1996 *Fukunishi et al.*, using just three photometers, reported the first ground-based evidence of elves which convincingly differentiated their flash from that of a Rayleigh-scattered lightning flash or that due to sprites. The authors proposed the name of "elves" for the flash, and this name has since become standard. Figure 3 of *Fukunishi et al.* [1996b] shows an event which would now likely be recognized as the halo region of a sprite, rather than an elve [*Barrington-Leigh et al.*, 2000]. *Fukunishi et al.* [1996b] reported that elves occur in response almost exclusively to large positive cloud-to-ground lightning discharges, while it is now known [*Barrington-Leigh and Inan*, 1999] that elves are produced by both positive and negative discharges. *Fukunishi et al.* [1996b] interpreted their data in terms of possible downward motion of the optical emissions while *Inan et al.* [1996c] showed that this apparent downward motion would result from the predicted rapid lateral expansion of the optical luminosity.

The definitive photometric determination of the rapid lateral expansion was realized using an instrument especially designed for this purpose, namely the photometric array referred to as the Fly's Eye. Measurements with the Fly's Eye constitute the bulk of this dissertation, the first results of which were reported by *Inan et al.* [1997].

Fukunishi et al. [1997] used, but did not show, data from a vertically-arrayed sixteen-anode photomultiplier tube as well as a low-light-level CCD camera and a framing/streak camera with exposures at 0.5 or 1 ms intervals. These optical measurements were used to identify and discriminate between elves and sprites for a study of ultra-low frequency magnetic field transients. It was concluded that elves are associated almost exclusively with clustered sprites with bead-like fine structure and never with "carrot-like" sprites, and that ULF signatures differed for these two classes of event.

Armstrong et al. [1998a] used photometers with two blue filters having different degrees of response to emissions from neutral and ionized N_2, in an attempt to differentiate between elves, sprites, and lightning based on the ratio of photometer responses. No explanation is given for how elves were identified, but for the "very few" cases observed, their data suggest little ionization in comparison with sprites.

Barrington-Leigh and Inan [1999] described explicit criteria for the identification of elves using the Fly's Eye and studied 39 elves from one storm to determine their relationship to causative lightning. The spatial extent of each optical event was assessed and possible effects of large thunderstorm systems on D region ionization were discussed. This work is detailed in Sections 4.2 and 4.4.

Watanabe [1999], in his Master's thesis, presented data from studies using the optical equipment mentioned by *Fukunishi et al.* [1997]; these results had previously only appeared at conferences. The analysis concerning elves consists largely of the conclusion that "column-sprites" are always preceded by elves.

2.3 Lightning quasielectrostatic fields and mesospheric discharges: sprites

While elves are produced by electromagnetic radiation, the intensity of which is proportional to the time deriative of a lightning current moment, sprites occur in response to the time integral of the current moment, where the integral is taken over a period of approximately the local relaxation time ϵ_0/σ.

The theoretical and experimental literature concerning sprites is large and continues to develop significantly. Recent reviews exist of theoretical [*Rowland*, 1998] and experimental [*Boeck et al.*, 1998; *Rodger*, 1999; *Heavner*, 2000] studies. Several subjects of particular interest for this work are briefly addressed below.

Significant topics not treated below include the role of relativistic runaway breakdown in sprites and lightning-magnetosphere coupling [*Fishman et al.*, 1994; *Inan et al.*, 1996b; *Roussel-Dupre and Gurevich*, 1996; *Taranenko and Roussel-Dupre*, 1996; *Lehtinen et al.*, 1997; *Roussel-Dupre et al.*, 1998; *Lehtinen et al.*, 1999; *Lehtinen*, 2000], the discovery and explanation of blue jets [*Wescott et al.*, 1995, 1998; *Pasko et al.*, 1996a, 1997b; *Yukhimuk et al.*, 1998], VLF scattering effects of electron temperature and density changes in the ionosphere caused "directly" by lightning [*Inan et al.*, 1988, 1993, 1995, 1996a,d; *Dowden et al.*, 1996, 1998; *Johnson et al.*, 1999; *Sampath et al.*, 2000], and HF radar detection of transient ionization changes in the mesosphere [*Roussel-Dupre and Blanc*, 1997; *Tsunoda et al.*, 1998].

History and nomenclature

Sprites properly entered the scientific arena in 1989 [*Franz et al.*, 1990] but were not given their modern name until 1994 [*Sentman et al.*, 1995]. Indeed, reports of exotic upward lightning and high-altitude discharges date to more than 100 years ago [see *Rodger*, 1999; *Heavner*, 2000, p. 10], and efforts by Vaughan and Vonnegut in the 1980's to consolidate eyewitness accounts revealed that aircraft pilots also had knowledge of such phenomena [e.g., *Vaughan and Vonnegut*, 1989]. *Chalmers* [1967, p. 377] includes a section entitled "Discharges from Cloud to Electrosphere" which discusses many studies giving possible visual, electrical, and even radar evidence for what might today be called sprites.

The theoretical foundations for the modern theories of sprites were laid by *Wilson* [1925], who predicted that thundercloud static electric fields would exceed the breakdown threshold of air at some altitude, that electrons could run away to highly relativistic energies above thunderstorms, and that these high altitude discharges would "doubtless give rise to atmospherics." These insights correspond to modern quasielectrostatic field (QE or QSF) conventional breakdown theories [*Pasko et al.*, 1995, 1996b, 1997a,b, 1998a; *Winckler et al.*, 1996; *Fernsler and Rowland*, 1996], relativistic runaway theories [*Fishman et al.*, 1994; *Roussel-Dupre and Gurevich*, 1996; *Inan et al.*, 1996b; *Lehtinen et al.*, 1997, 1999; *Lehtinen*, 2000], and the calculation and measurement of extremely low frequency (ELF) radiation from sprites [*Farrell and Desch*, 1992; *Pasko et al.*, 1998b, 1999b; *Cummer et al.*, 1998b; *Cummer and Stanley*, 1999; *Cummer and Inan*, 2000; *Reising et al.*, 1999; *Stanley et al.*, 2000].

Through a number of studies in the 1990's from the ground, aircraft, and Space Shuttle, the term "sprites" has come to refer to a mostly cohesive set of observations, largely in relation to optical emissions between ∼40 km and ∼90 km altitude [*Lyons*, 1994, 1996; *Lyons et al.*, 1998; *Boeck et al.*, 1995; *Winckler*, 1995; *Winckler et al.*, 1996; *Sentman and Wescott*, 1993, 1995; *Sentman et al.*, 1995; *Rairden and Mende*, 1995; *Boccippio et al.*, 1995; *Inan et al.*, 1995, 1996b]. Nomenclature has continued to play an important role in the understanding of sprites and the experimentally associated phenomena of blue jets (which propagate upward to <40 km) and elves. This is both because it serves to identify new phenomenology before it is understood theoretically ("hair," "tendrils") and because it may be used to group phenomena which are shown to have a common physical cause (sprites versus elves). Classifications such as "carrot," "column," and "angel" sprites are often not well-defined [*Sentman et al.*, 1995; *Wescott et al.*, 1998; *Stanley et al.*, 1999] but may foster important insights to come. These terms are not used in the present work. Because of the rich diversity of sprite forms, there has been a tendency to invent new terms to describe phenomena which, if at all possible, ought to be understood and described as features or variations of already-named concepts.

The diffuse region of sprites

Theories of sprites based on the electromagnetic pulse mechanism [*Milikh et al.*, 1995] and runaway electron breakdown [*Taranenko and Roussel-Dupre*, 1996] have not found much support in optical measurements. Other than these, theoretical studies accounting for the optical, electric, and plasma properties of sprites may be classified into two groups — those which describe bulk gas breakdown and those which make use of a corona streamer model to account for the fluid behavior of electrons. The former group generally does not produce modeled optical emissions below ∼60 to 70 km [*Pasko et al.*, 1995, 1996b, 1997a,b, 1998a; *Winckler et al.*, 1996; *Fernsler and Rowland*, 1996]. *Pasko et al.* [1998a] first placed this region into context and named it the diffuse upper region of sprites. As discussed in Section 5.1, virtually all studies in which elves were identified by means of ground-based video recordings have incorrectly referred to this upper diffuse region of sprites as 'elves' and have presumed it to be due to the EMP mechanism, when it actually is manifested by quasielectrostatic fields which may or may not also lead to streamer formation [see Section 5.1 and *Barrington-Leigh et al.*, 2000].

In 1999 the name of "halos" was agreed upon [*Barrington-Leigh et al.*, 1999b; *Heavner*, 2000, p. 31] for the luminosity in this region, even though it had since 1996 been well modeled and understood by the name of “sprites” in the theoretical literature.

Corona streamers in sprites

The physical reason for the existence of upper diffuse and lower streamer regions in sprites was described on page 7 (Section 1.3). Streamers have been discussed and modeled in the context of upper atmospheric discharges by *Pasko et al.* [1997b, 1998a, 2000] and *Raizer et al.* [1998].

Pasko et al. [1998a] predicted a transverse scale for streamers of ∼10 m at 70 km altitude, and *Raizer et al.* [1998] predicted a maximum velocity of $\sim 1.2\times 10^7$ m/s. These predictions have been assessed experimentally by *Stanley et al.* [1999] and *Gerken et al.* [2000].

ELF determination of current moments

As predicted by *Wilson* [1925] but not realized again until 1996 [*Stanley et al.*, 2000; *Cummer and Inan*, 1997], the currents flowing in sprites may radiate as strongly as their associated lightning return strokes. This radiation occurs primarily in the ELF band (30 Hz to 3 kHz) in accordance with the several-to-tens of milliseconds lifetime of sprites.

In addition, ELF currents in cloud-to-ground lightning are thought to be most significant in setting up the large quasielectrostatic fields which initiate sprites [*Cummer and Inan*, 1997; *Bell et al.*, 1998; *Williams*, 1998; *Huang et al.*, 1999]. The method for determining source current moments from radiated electromagnetic fields was pioneered by *Cummer and Inan* [1997] and is described in a refined form by *Cummer and Inan* [2000]. This method uses Earth-ionosphere waveguide mode theory and can make use of a large number of lightning strokes to determine first the ionospheric propagation parameters [*Cummer et al.*, 1998a]. Determination of lightning electrical input to the upper atmosphere is of prime importance in comparing models and observations of sprite breakdown and development.

Recently, multi-site ULF (<30 Hz) measurements were made in conjunction with sprite observations, and currents in sprites and lightning were determined in this frequency range too.[¶]

Spectral studies

The acquisition of optical spectra of sprites was among the prime objectives of early high-altitude ground-based and airborne sprite campaigns. Spectra of sprites were reported generally to be dominated by the neutral band $N_2(1P)$ [*Mende et al.*, 1995; *Hampton et al.*, 1996; *Heavner*, 2000, p. 100]. Occasional contributions were detected from ionized species [*Heavner*, 2000, p. 87]. Multispectral photometric studies have concluded that ionized emissions likely occur during a brief pulse during the onset of sprite luminosity [*Armstrong et al.*, 1998a, 2000; *Suszcynsky et al.*, 1998] and that the degree of ionization in sprites varies greatly [*Armstrong et al.*, 2000; *Heavner*, 2000, p. 98].

Spectroscopic studies may be compared with theoretical models [*Pasko et al.*, 1995, 1997b; *Milikh et al.*, 1997, 1998; *Morrill et al.*, 1998]. It is found that the average electron energy which dominates observed emissions is near 1 eV [*Green et al.*, 1996].

2.4 Electromagnetic model

The effect of vertical tropospheric lightning currents on the electron population at altitudes up to 100 km is modeled in this dissertation with a finite-difference time domain calculation in cylindrical coordinates, adapted from that used by *Veronis et al.* [1999]. The model solves Maxwell’s equations

---

[¶] Reported by Steve Cummer and Martin Füllekrug at the June 2000 CEDAR meeting in Boulder, Colorado, U.S.A.

around a vertical symmetry axis, solving for the vertical and radial electric field, azimuthal magnetic field, electron density, and ion and electron conduction currents. The Earth's magnetic field is neglected, as justified in Figure 1-1 for altitudes up to ∼95 km. Optical emissions are calculated from the electron density and the net electric field, and instrumental response to the emissions is calculated for a given geometry and field-of-view.

These calculations are carried out in three steps. The electron density n_e and electric field E are calculated as a function of time and space in the cylindrical geometry. Next, the volume optical emission rates are calculated from n_e and E in the same geometry. Finally, the optical signal seen from a chosen vantage point is calculated using three dimensional geometry. The curvature of the Earth is taken into account only in this last step; however, the resulting inaccuracy is small for radial distances $<\sim$300 km in the cylindrical geometry.

A cloud-to-ground lightning return stroke (CG) is modeled by imposing a current between the ground and a spherical gaussian charge distribution at 10 km altitude. For lightning currents of ∼30 μs duration, mesospheric electric fields are dominated by those of the lightning electromagnetic pulse (EMP), while for ∼500 μs currents, radiation effects are negligible and the quasielectrostatic (QE) field dominates. Both EMP and QE fields are inherently accounted for in this fully electromagnetic model [*Veronis et al.*, 1999].

The initial conditions of ρ=0, $\mathbf{E}$=0 allow $\rho(t)$ not to be recorded explicitly in the calculation. Instead, all changes to the charge density are accounted for implicitly by the displacement current, and the resulting fields are fully in accord with Maxwell's equations, including contributions to the current density $\mathbf{J}$ from both electrons and ambient (not modified) ion conductivity.

However, this model is not faithful to the Boltzmann equation (1.6). The $[\mathbf{v} \cdot \nabla_{\mathbf{r}}]f$ term, which accounts for diffusion, is ignored, as is the vector velocity dependence of the distribution function f. The effect of the total electric field $|\mathbf{E}|$ along with all inelastic collisions is accounted for only through the swarm parameters for mobility, attachment, and ionization rates. As a result, changes to the explicitly calculated n_e result from ionization and attachment, but not from the relatively small contribution of $\nabla \cdot \mathbf{J}$. Nevertheless, "space charge" effects on the electric field are accounted for via equation (1.3) and are evident in the results shown below.

Even more than this absence of fluid (electron transport) properties, the primary feature which renders the model used here incapable of reproducing streamer behavior is the impracticality of numerical solutions with extremely high spatial resolution. The huge conductivity gradients which intensify the electric field at the head of a streamer must be resolved (and managed in a numerically stable way) in order to produce a "self-propagating" discharge [*Dhali and Williams*, 1985; *Pasko et al.*, 1998a]. While this can be done for modeling streamer development at a given altitude and for a given externally applied initial electric field [*Pasko et al.*, 1998a], it is impractical to model simultaneously the full temporal and spatial development of the QE field over the full mesospheric altitude range. Our model also does not account for a wide variety of inelastic processes, such as photoionization, which can play a role in creating free electrons ahead of a streamer and which become important for the distribution function at the high values of E/E_k in a streamer head. While ambipolar diffusion is not accounted for in the current densities used here, it has been shown to be a negligible consideration even in streamers [*Dhali and Williams*, 1985], as compared with the electrostatic effects of unbalanced charge.

Sections 2.4.1, 2.4.2, and 2.4.3 give the numeric values of various coefficients and cross sections used to account for elastic and inelastic collision processes and to calculate optical emissions in the model. The ionization and attachment coefficients and the rates of molecular excitation responsible for optical emissions have been updated from those used by *Veronis et al.* [1999], and are based on the compilations and calculations of *Pasko et al.* [1999a].

2.4.1 Heating

Aside from those involving sources and losses of free electrons, all changes to the electron distribution function are accounted for in the model by changes to the electron mobility. We use the form of $\mu_e(E/N)$ provided by *Pasko et al.* [1997b], which is a polynomial fit to experimental data. *Pasko et al.* [1997b] provide references to the experimental data, as well as a comparison with kinetic calculations.

The electron conductivity follows from the mobility and electron density as $\sigma = q_e n_e \mu_e$. Conduction current in the model is calculated using both electron and ambient ion conductivity [*Pasko et al.*, 1997b].

2.4.2 Ionization

Changes in electron density due to electron impact ionization and dissociative attachment are calculated using

$$\frac{dn_e}{dt} = (\nu_\mathrm{i} - \nu_\mathrm{a})n_e, \tag{2.15}$$

where

$$\nu_\mathrm{i} = \begin{cases} 0 & \text{for } \frac{E}{N/N_0} < 1122000 \text{ V-m}^{-1}, \\ \dfrac{N}{N_0}10^p & \text{otherwise,} \end{cases}$$

and where

$$p = \sum_{i=0}^{3} a_i \left[\log_{10}\left(\frac{E}{(1 \text{ V-m}^{-1})}\frac{1}{N/N_0}\right)\right]^i$$

with N/N_0 being the neutral density normalized to sea level, and a_i given as follows:

i	0	1	2	3
a_i	-624.68	249.60	-32.878	1.4546

Similarly,[‖]

$$\nu_\mathrm{a} = \begin{cases} 0 & \text{for } \frac{E}{N/N_0} < 316200 \text{ V-m}^{-1}, \\ \dfrac{N}{N_0}10^p & \text{otherwise,} \end{cases}$$

where

$$p = \sum_{i=0}^{4} b_i \left[\log_{10}\left(\frac{E}{(1 \text{ V-m}^{-1})}\frac{1}{N/N_0}\right)\right]^i$$

and b_i is as follows:

i	0	1	2	3	4
b_i	-3567.0	1992.68	-416.601	38.7290	-1.35113

Values of ν_i and ν_a are shown in Figure 2-4. The point at which $\nu_\mathrm{i} = \nu_\mathrm{a}$ corresponds to $E = E_k$. The fits given here are appropriate for $E \lesssim 5E_k$ [*Pasko et al.*, 1997b].

For small electric fields, the three-body attachment process dominates attachment (Section 1.3), and

$$\nu_{\mathrm{a(3\text{-}body)}} \simeq \left(\frac{N}{N_0}\right)^2 4\times10^7 \text{ s}^{-1} \tag{2.16}$$

[‖] The effects of three-body attachment, given in equation (2.16), are negligible over the time scales modeled.

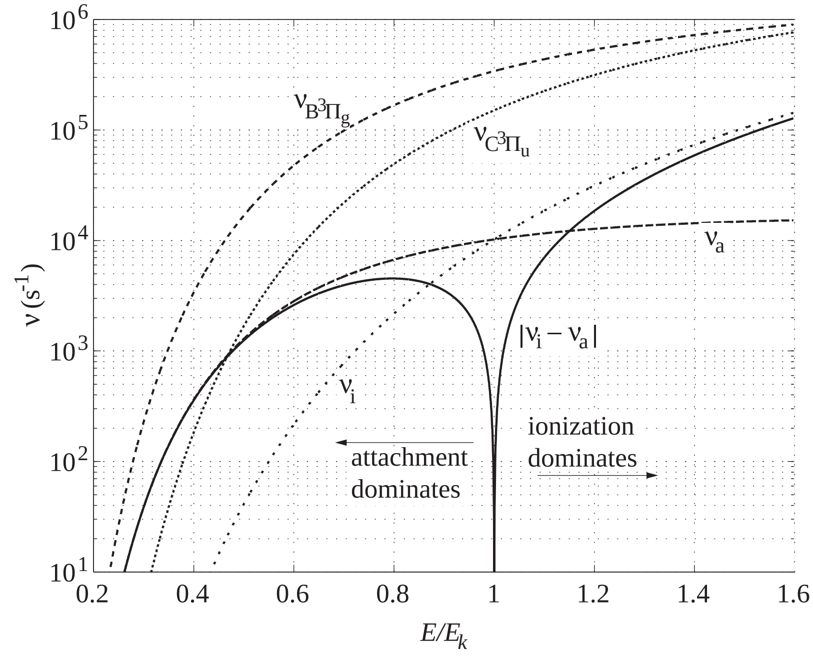

Figure 2-4: Model ionization and dissociative attachment rates. Also shown are the electron impact excitation coefficients for the states producing optical emissions in the N_2(1P) and N_2(2P) bands.

[*Glukhov et al.*, 1992, and Victor Pasko, *private communication*]. However, neither this relatively slow effect nor steady-state ionization processes which determine the ambient ionization level are included in the model.

2.4.3 Optical emissions

Optical emissions are calculated only from two molecular bands of neutral N_2 which are expected to dominate the instrument responses of our photometers (*Taranenko et al.* [1992] and Section 3.3). These optical bands are known as the first positive (1P) and second positive (2P) bands and they result from transitions between electronic states of N_2 which have the following designations and threshold energies:

$$\begin{aligned} \mathrm{N_2(2P)}: &\quad \mathrm{C^3\Pi_u} \quad (11\ \mathrm{eV}) \quad \xrightarrow[\text{UV,blue}]{50\ \text{ns}} \quad \mathrm{B^3\Pi_g} \quad (7\ \mathrm{eV}) \\ \mathrm{N_2(1P)}: &\quad \mathrm{B^3\Pi_g} \quad (7\ \mathrm{eV}) \quad \xrightarrow[\text{red,IR}]{5.9\ \mu\text{s}} \quad A^3\Sigma_\mathrm{u}^+ \quad (6\ \mathrm{eV}) \end{aligned} \tag{2.17}$$

The spectra from these transitions are complex as a result of vibrational sub-states with additional energies of up to ~2 eV [*Stanton and St John*, 1969; *Green et al.*, 1996].

The excitation, quenching, and cascading processes involved in emission in these bands are discussed by *Pasko et al.* [1997b]. We make use of the fact that the lifetimes of the states $C^3\Pi_u$ and $B^3\Pi_g$, given in (2.17), are fast compared with the variations in electric field and with the thermal relaxation time τ_{th} of the distribution function. This fact justifies the assumption that instantaneously the population n_k of the excited state k is constant: $\partial n_k/\partial t \simeq 0$, where k corresponds to $\mathrm{B}^3\Pi_\mathrm{g}$ or $\mathrm{C}^3\Pi_\mathrm{u}$. The population and depopulation terms for excited state k are [*Sipler and Biondi*, 1972]:

$$\frac{\partial n_k}{\partial t} = \nu_k n_e - n_k(A_k + \alpha_1 N_{\mathrm{N}_2} + \alpha_2 N_{\mathrm{O}_2}) + \sum_m n_m A_m$$

where $\nu_k n_e$ is the electron impact excitation rate, A_k is the Einstein coefficient for radiative relaxation, and α_i are the coefficients for collisional deexcitation (commonly called "quenching") with nitrogen and oxygen. The sum is carried out over other states which radiatively relax ("cascade") into state k; for instance, N_2(2P) emission populates the state $\mathrm{B}^3\Pi_\mathrm{g}$, which in turn may radiate in the N_2(1P) band.

The stationary condition mentioned above gives

$$n_k \simeq \frac{n_e \nu_k + \sum n_m A_m}{A_k + \alpha_1 N_{\mathrm{N}_2} + \alpha_2 N_{\mathrm{O}_2}} \tag{2.18}$$

and the volume photon emission rate is $A_k n_k$. The numerical values of the various coefficients used for the two bands studied are as follows [*Pasko et al.*, 1997b]:

	α_1	α_2	A_k	m(cascade)
N_2(2P)	0	3×10^{-16} m^{3}s^{-1}	2×10^7 s^{-1}	none
N_2(1P)	10^{-17} m^{3}s^{-1}	0	1.7×10^5 s^{-1}	by N_2(2P)

The values of the excitation coefficient ν_k were calculated according to the following polynomial fits [*Pasko et al.*, 1999a]:

$$\nu_{\mathrm{C}^3\Pi_\mathrm{u}} = \begin{cases} 0 & \text{for } \frac{E}{N/N_0} < 10^5 \text{ V-m}^{-1}, \\ \text{(not calculated)} & \text{for } \frac{E}{N/N_0} > 1.6\times10^7 \text{ V-m}^{-1}, \quad \text{i.e., } E > 5E_k \\ \frac{N}{N_0}10^p & \text{otherwise,} \end{cases}$$

where

$$p = \sum_{i=0}^{4} c_i \left[\log_{10}\left(\frac{E}{(1\text{ V-m}^{-1})}\frac{1}{N/N_0}\right)\right]^i$$

and b_i is as follows:

i	0	1	2	3	4
c_i	−3668.69	2044.92	−426.910	39.6648	−1.38351

The coefficient $\nu_{\mathrm{B}^3\Pi_\mathrm{g}}$ is calculated the same way but with the substitution of d_i for c_i:

i	0	1	2	3	4
d_i	−3501.49	1909.46	−390.447	35.5826	−1.21911

These calculations are done assuming the same air composition (i.e., 78% N_2, etc.) at high altitude as at sea level, a good assumption for the altitudes of interest. The quenching rate terms in the denominator of (2.18) become comparable to the Einstein coefficient A_k only below altitudes of 32 km for N_2(2P) and 50 km for N_2(1P) so that the emissions produced in the lower nighttime ionosphere are not significantly quenched.

2.5 Model Results

Snapshots of electric field strength and optical emissions calculated with the model for two different input currents are shown in Figures 2-5 and 2-6. The calculation was run on a 350 km×110 km grid with ∼1 km×1 km resolution. The time step of 16 ns was constrained by the conductivity at the upper altitude limit (see Figure 1-1) rather than by the grid size and the usual Courant condition [e.g., *Taflove*, 1995, p. 46 and 49]. The region below 50 km was assumed to be free space.

Figure 2-5 shows snapshots at various times over the course of ∼1 ms following the onset of a short-duration vertical lightning return stroke current flowing between 10 km altitude and the ground. The color scale shows only the magnitude of the vector electric field, while the red contour lines indicate the intensity of optical emissions in the N_2(1P) band. There are two regions of strong electric field evident in the simulation results. One is visible directly overlying the model lightning (at zero radius) and is due to the static field of the electric charge configuration modified by the return stroke current. The other region, evident as two outward-expanding arcs (or shells in three dimensions), is in this simulation much stronger above 60 km altitude than the static field. This is the radiated lightning electromagnetic pulse, and it is strong as a result of the fast-changing input current. The model current rises linearly over 30 μs to 120 kA and then decays exponentially with a time constant of 60 μs. Peaks in the electric field (proportional to the rate of change of the current moment) due to both the rise and fall of the current are visible, and an enhancement in the second such peak, especially at 0.470 ms, is evidence of constructive interference with the ionospheric reflection of the first half of the pulse.

Optical emissions from N_2(1P) are seen to occur in an expanding annulus that is instantaneously narrow both in vertical and radial thickness. The radial extent is on the order of $c(30\ \mu\text{s} + 60\ \mu\text{s}) \simeq 30$ km, while the photon emission rate exceeds 2×10^6 cm^{-3}s^{-1} between 82 and 96 km altitude. The flash extends outward as far as 250 km in less than 1 ms, implying a horizontal extent of >500 km. Optical flashes produced in this way are indeed the phenomenon discussed earlier and called elves [*Fukunishi et al.*, 1996b], and modeled optical signatures as they would be seen by instrumentation below the discharge are calculated from these results and discussed in Section 4.1.1.

The radiated electromagnetic pulse and its reflections continue to propagate in the Earth-ionosphere cavity and can be measured at large distances, as discussed in Section 3.1.

Figure 2-6 shows snapshots from a calculation using the same model with a slower input lightning current. The electric field strength and the optical emissions are now dominated by those due to the static electric field resulting from the changed charge configuration. In this case the model lightning current rises linearly over 300 μs to 100 kA and then decays exponentially with a time constant of 600 μs. The current flows between the ground and a distribution of charge located at 10 km altitude and having a Gaussian shape with half-peak width and half-peak height of ∼6 km. Three-dimensional lightning measurements indicate that a disc of charge at 7 to 8 km altitude would be a more realistic distribution [*Stanley*, 2000, p. 80]. However, these details do not greatly affect the electric field distribution at high altitudes and thus the outcome of the model, which in the quasielectrostatic case is sensitive primarily only to the total charge moment change [*Pasko et al.*, 1999b].

The three inset boxes in Figure 2-6 show that the source current continues to flow throughout the simulated period, and well after the onset of the optical emissions. Optical emissions exceeding an intensity of 2×10^6 cm^{-3}s^{-1} extend more than 80 km horizontally, and persist in the region overlying the causative lightning current for 1 ms or longer. The emitting region also descends in altitude noticeably over time as a result of enhanced ionization, which causes increased conductivity and a reduced relaxation time τ_E, effectively ‘expelling’ the electric field. These optical emissions correspond to the diffuse upper region of sprites [*Pasko et al.*, 1997b, 1998a] and their form as seen from the ground is discussed in detail in Section 5.1.

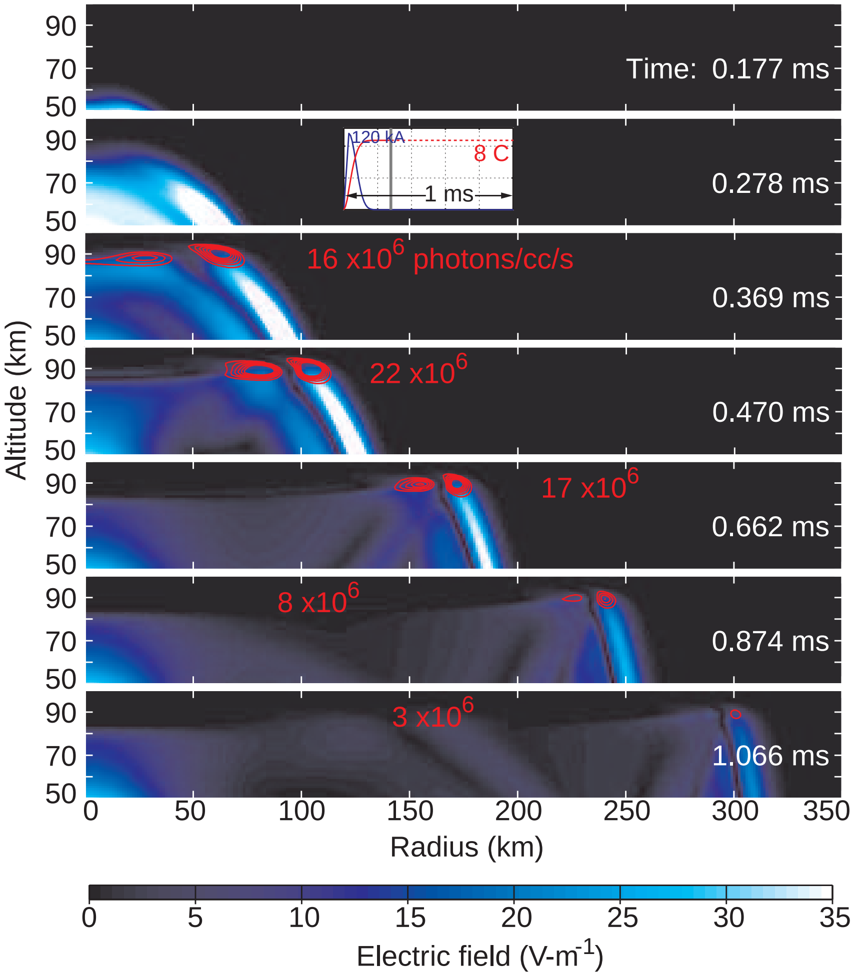

Figure 2-5: Cross section of electric field and $N_2(1P)$ **optical emissions for EMP.** The color scale indicates magnitude of the electric field, while red contours show intensity of optical emissions. The contour values are at $2, 4, 6, \ldots \times 10^6$ photons cm^{-3} s^{-1}. Time is measured from the onset of the return stroke current. The inset box shows the injected model lightning current and its integral over time.

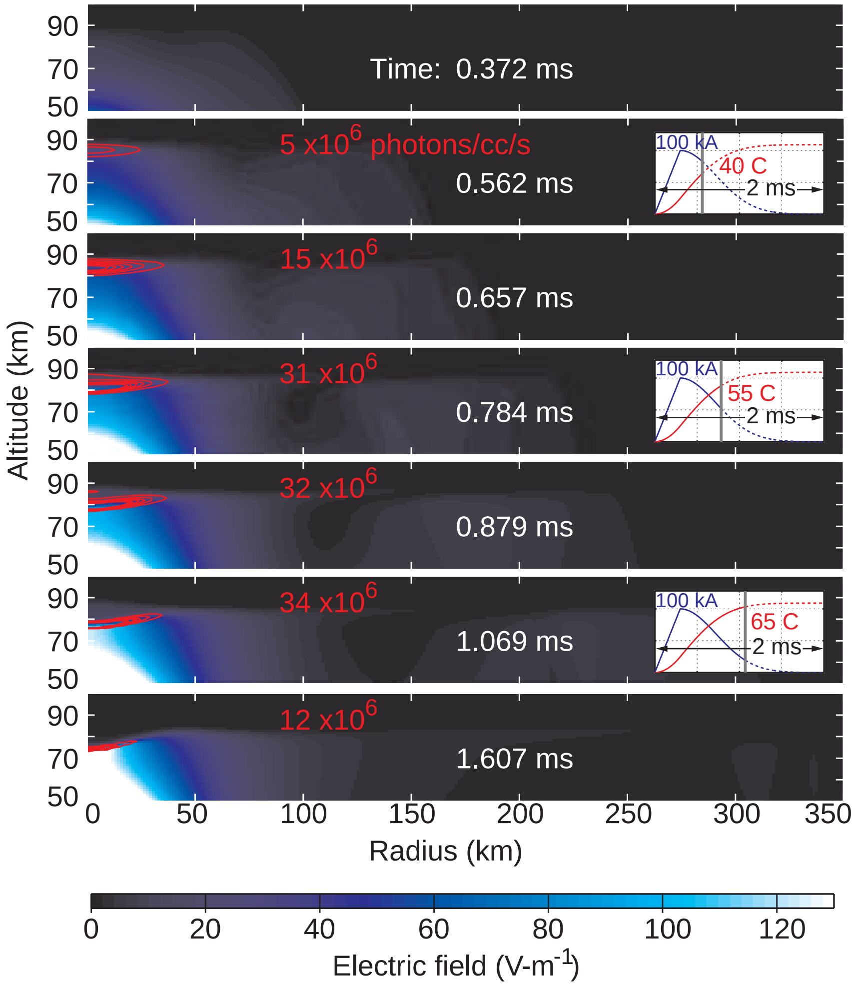

Figure 2-6: Cross section of electric field and $N_2(1P)$ **optical emissions for QE.** The format is similar to Figure 2-5 but the input current is much slower.

2.5.1 Ionization changes in the lower ionosphere

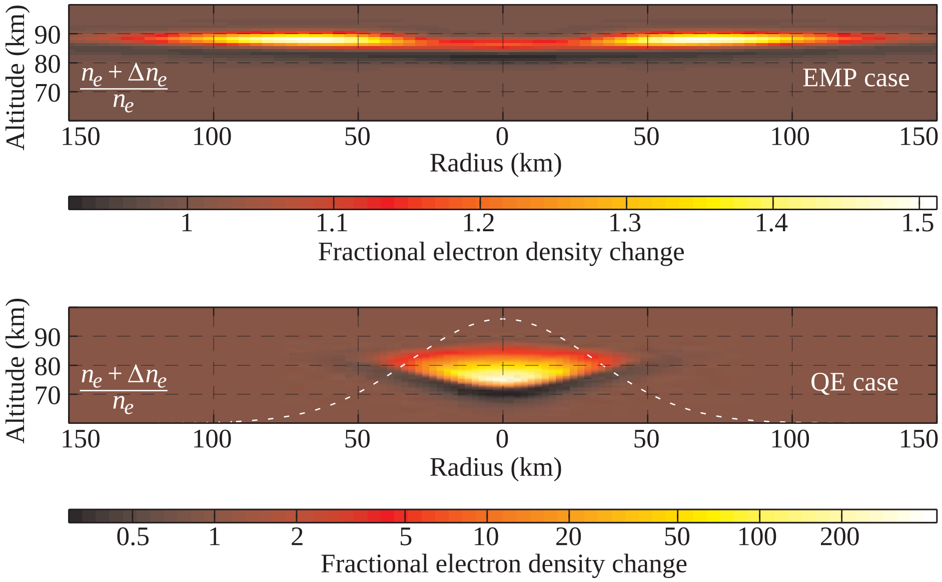

Figure 2-7: Model cross sections of ionization enhancement due to elves (EMP case) and the diffuse portion of sprites (QE case) 2 ms after the lightning stroke. The line shows the shape of the disturbed region deduced by *Johnson et al.* [1999]. The effect of dissociative attachment is evident in the dark band below each bright region.

Figure 2-7 compares the ionization changes produced in elves and in the diffuse upper portion of sprites. The central minimum in the EMP case is due to the radiation pattern of a vertical dipole, and it suggests that even when elves and sprites occur together, the extra ionization in elves is not likely to affect significantly the breakdown processes in sprites occuring overhead the causative CG. On the other hand, it would not be surprising for the large ionization enhancements evident in the QE case to affect the formation of any subsequent streamer breakdown. Indeed, observations in Section 5.1 show a correlation betweeen the tops of the columnar features and the curved lower boundary of the observed diffuse region. The shape of the spatial distribution of the optical emissions is also discussed further in Section 5.1.

Also, it is interesting to note in this regard that at the later times shown in Figure 2-6, the spatial resolution of the model becomes inadequate to resolve the large gradients evident in electric field (and conductivity) which arise at the lower boundary of the region of enhanced ionization. This behavior is indicative of the need for a prohibitively higher spatial resolution in order to reproduce streamer behavior.

2.5.2 Early/fast VLF perturbations

Johnson et al. [1999] determined that the lateral extent of the ionospheric disturbance responsible for so-called "early/fast" VLF perturbations was 90±30 km, suggesting that clusters of ionization columns in sprites were not the cause. Instead, the authors suggest that a quiescent (rather than transient) heating (rather than ionization) mechanism [*Inan et al.*, 1996a] could explain the observations. However, as shown in Figure 2-7, the diffuse upper region of sprites may produce significant ionization enhancements with a horizontal scale of ~80 km and at an altitude of 70 to 85 km, below the nighttime VLF reflection height and where the time scale for relaxation of electron density enhancements is 10 to 100 s [*Glukhov et al.*, 1992]. These characteristics qualify the diffuse sprite region as a candidate for a cause of at least some of the VLF scattering events as resolved by *Johnson et al.* [1999].

In addition, "post-onset peaks" lasting ~1 s may speculatively be ascribed [*Inan et al.*, 1996d] to the heating and ionization change evident in Figure 2-7 at lower altitude (down to 70 km), where the three-body electron attachment time scale is <10 s [*Glukhov et al.*, 1992]. However, this would predict a broader VLF scattering pattern for the post-onset peak portion of the event, and may also require a temporary lowering of the VLF reflection height [*Wait and Spies*, 1964].

VLF early/fast events are observed with both +CG and −CGs, and do not correlate well with lightning return stroke peak current, as reported by NLDN. This, in part, led *Inan et al.* [1996a] to propose a less exotic cause than electrical breakdown. However, many lightning discharges of both polarities may produce significant charge moment changes on 0.5 ms time scale and may produce sprite halos but no further sprite breakdown, for which additional charge moment changes, possibly accumulating over some milliseconds, may be necessary. Many of these events may be invisible when integrated on a 17 ms video field. As mentioned by *Inan et al.* [1996a], a combination of quiescent, EMP, and QE effects is likely necessary to explain all observed VLF early/fast events.

2.5.3 Multiple events

In view of the relatively high lightning rate in many thunderstorms, it is of interest to evaluate possible cumulative effects of electromagnetic pulses from successive lightning strokes. As mentioned in Section 1.3, such a study is also motivated by (1) the common occurrence of several return strokes in the same location within a few hundred milliseconds (a cloud-to-ground "flash") and (2) by the possibility of elves affecting a large enough area that consecutive cloud-to-ground flashes (separated by tens of seconds) in a large storm system may heat the same region of the ionosphere.

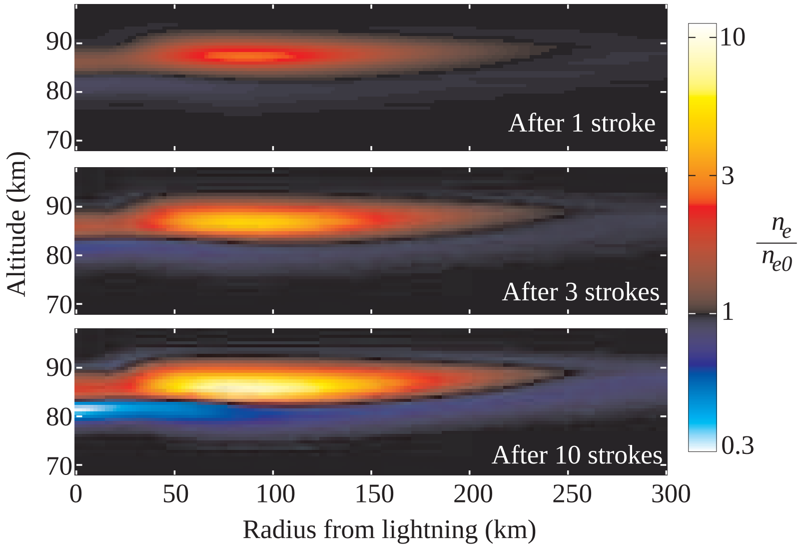

Figure 2-8: Effect of multiple lightning strokes on ionization in elves. Blue regions show net electron depletion, while red shows ionization enhancements. Unlike in Figure 2-7, the axes are not to scale.

Figure 2-8 shows the electron density changes resulting from 1, 3, and 10 successive cloud-to-ground strokes with 2 ms separation. The color scale shows net attachment in blue and net ionization in red. Changes to the electron density are locally as high as a factor of 8 increase and a factor of 3 decrease after 10 strokes. The electron density enhancement peaks at a radius of ~80 km [*Rowland*, 1998] and the attachment peaks in the vicinity overlying the lightning.

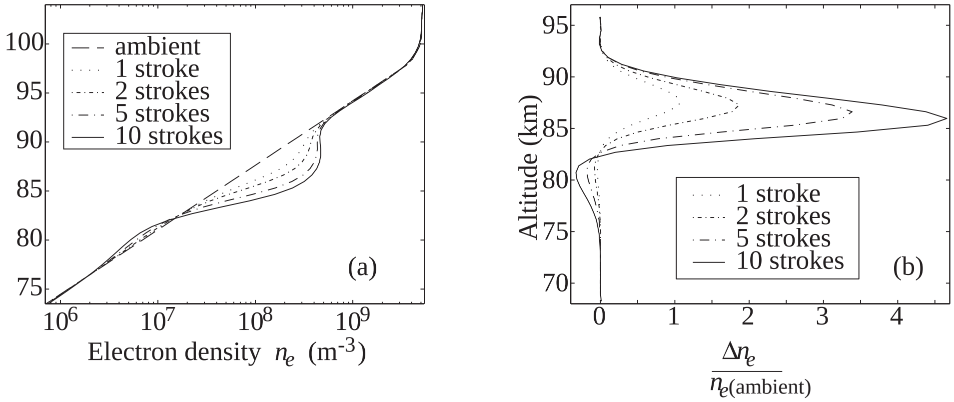

Figure 2-9: Multiple-stroke ionization changes area-averaged over $r < 150$ km. In (a), the differential changes of Figure 2-8 are put into the context of absolute electron densities in the lower ionosphere. (b) The same data but presented in the format used by *Taranenko et al.* [1993a].

Figure 2-9 presents the same data but averaged over the 300 km diameter region overlying the causative lightning. This is relevant for consideration of the large-scale effects of an intense and distributed lightning storm such as a mesoscale convective system. Figure 2-9(b) shows normalized electron density changes and provides direct comparison with the one-dimensional results of *Taranenko et al.* [1993a], though using a different model lightning current. The altitude distribution of electron density enhancements and depletions agrees well for a single return stroke. For multiple successive strokes, however, the two dimensional model used here shows that the altitude of peak enhancement drops with successive strokes by ~2 km after 10 strokes.

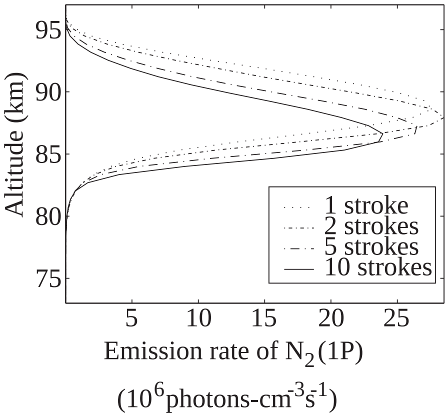

Figure 2-10: Multiple-stroke $N_2(1P)$ emissions area-averaged over $r < 150$ km.

Figure 2-10 shows a similar area-averaged altitude scan of optical emissions. These are seen to decrease in intensity and mean altitude for multiple incident electromagnetic pulses.

Chapter 3

Instrumentation and Atmospheric Optical Propagation

A variety of strategies have been employed to remotely sense changes in the upper atmosphere due to sprites and elves. These include the use of low-light video imagery, cooled CCD cameras, radio receivers from ultra-low to very-high frequencies, photometers, radar systems, spectrographs, and high speed imagers. The primary method used in this work involves an array of high speed photometers designed specifically for the detection of elves, but the photometric measurements are supplemented by ELF/VLF radio recordings and various image-intensified video systems.

The atmospheric propagation of radio and optical signals is discussed below in Sections 3.1 and 3.2. Section 3.3 addresses the theory of photometric measurements made over a wavelength range that is large compared with details in the observed spectrum and with variations in the instrument response. The subsequent sections cover the optical instrumentation used and discuss calibration and determination of pointing direction.

3.1 ELF and VLF sferic recordings

Electromagnetic recordings of lightning radiated pulses, or "sferics" in the frequency range 30 Hz to 25 kHz were made using wide (10^3) dynamic range impedance-matched receivers and air-core loop antennae, generally far from the source lightning. Such an instrument is sensitive to the rate of change of the horizontal magnetic field at the ground. An alternative method for recording lightning sferics is to measure the vertical electric field using a pair of parallel conducting plates or a vertical monopole antennae.

Sferic data are primarily used to identify the time and polarity of cloud-to-ground lightning, and also to infer the vertical currents flowing in the lightning. While the onset polarity of a sferic in vertical electric field data always unambiguously indicates whether lightning is positive or negative cloud-to-ground, this information is also determined for our loop antenna (i.e., horizontal magnetic field) if the loop orientation and the approximate direction to the lightning (with precision adequate to specify the quadrant of the signal arrival azimuth angle) are known. In the cases shown in this work, the precise locations of cloud-to-ground lightning were available from the National Lightning Detection Network.

The lightning radiated spectrum peaks in the ELF and VLF (3 Hz to 30 kHz) radio bands [*Uman*, 1987, p. 119]. Because the Earth-ionosphere cavity is bounded by a highly conducting ground and the conducting ionosphere at these frequencies, electromagnetic pulses from lightning may propagate long distances in modes analogous to the modes (TE, TM, and TEM) of an ideal parallel-plate waveguide [e.g., *Inan and Inan*, 1999, p. 739]. In the imperfect (lossy and anisotropic) waveguide of the ground and ionosphere, all three mode families contribute to the horizontal magnetic field and vertical electric field at higher frequencies [*Cummer*, 1997, p. 32]; however below ~1.5 kHz, only the TEM mode propagates. This frequency corresponds to the TE and TM lowest mode cutoff frequency, equal to $c/2h$ in the ideal waveguide, where c is the speed of light and h is the separation of the conducting plates.

Techniques were recently developed for remotely sensing D region properties using TE and TM modes in lightning sferics [*Cummer et al.*, 1998a] and for deducing vertical source current moments using the TEM mode at frequencies below 1.5 kHz [*Cummer and Inan*, 2000]. The latter technique is used in Section 5.2. Horizontal currents at cloud heights are inefficient at exciting the TEM mode in the Earth-ionosphere waveguide since the radiation pattern of a horizontal antenna above conducting ground exhibits a null at low elevation angles [*Jordan and Balmain*, 1968, p. 641-644]. As a result, horizontal current determination for frequencies below ~1.5 kHz is not possible using long-range receivers.

Sferics were recorded in digital format on magnetic tape or in triggered snapshots onto compact disks. The antenna gains were deduced from their geometric properties and the receiver was calibrated by injecting known currents into the preamplifer while it was connected to a lumped 'dummy' load having the same input impedance as the actual loop used for measurements. Sferic waveform magnitudes shown in this work are expressed as magnetic field amplitudes B which correspond to the measured $\partial B/\partial t$ in an electromagnetic wave in free space.

3.2 Atmospheric optical propagation

Ground-based optical observations of sprites and elves are often carried out at viewing elevation angles near horizontal and as a result are subject to particularly strong effects of Rayleigh-scattering and refraction along the line of sight. These effects and some other causes of extinction are investigated below.

3.2.1 Cloud and Rayleigh-scattering: temporal considerations

Figure 3-1 shows calculations of Rayleigh-scattering between a source at 5 km altitude and 675 km range (great circle distance) and a receiver on the ground, located at the origin of the plots. The axes are aligned with the observer's local horizontal and vertical and show values of the various quantities as a function of position in the vertical plane that includes the source and the observer. Because the source (lightning) and receiver are beyond each other's horizons, no direct light can be observed and any light originating at the source can reach the receiver only after Rayleigh-scattering from the sky. We only consider single-scattering for reasons that will be clear in the following discussion. Thus the region in which received light is scattered is bounded by the lines of local horizontals of the source and observer. The top panel in (a) shows with a logarithmic color scale the Rayleigh-scatter coefficient* for light with 700 nm wavelength, which is proportional to the atmospheric density. The curvature of the atmosphere is evident. The second plot shows the intensity of the direct flash, which is diminished as r^{-2} and attenuated by Rayleigh-scattering.

The third plot shows the analogous quantity as seen from the observer's point of view — that is, the fraction of light which, if scattered towards the observer at each given point, would reach the observer. In this case r^{-2} does not play a role for an optical detector with a fixed solid angle of acceptance.

---

*The isotropic Rayleigh-scatter coefficient β is defined such that the transmitted fraction of light is $T = e^{-\int \beta(r)dr}$, where the integral is carried out over the line of sight. The optical depth, mentioned below, is simply $\int \beta(r)dr$.

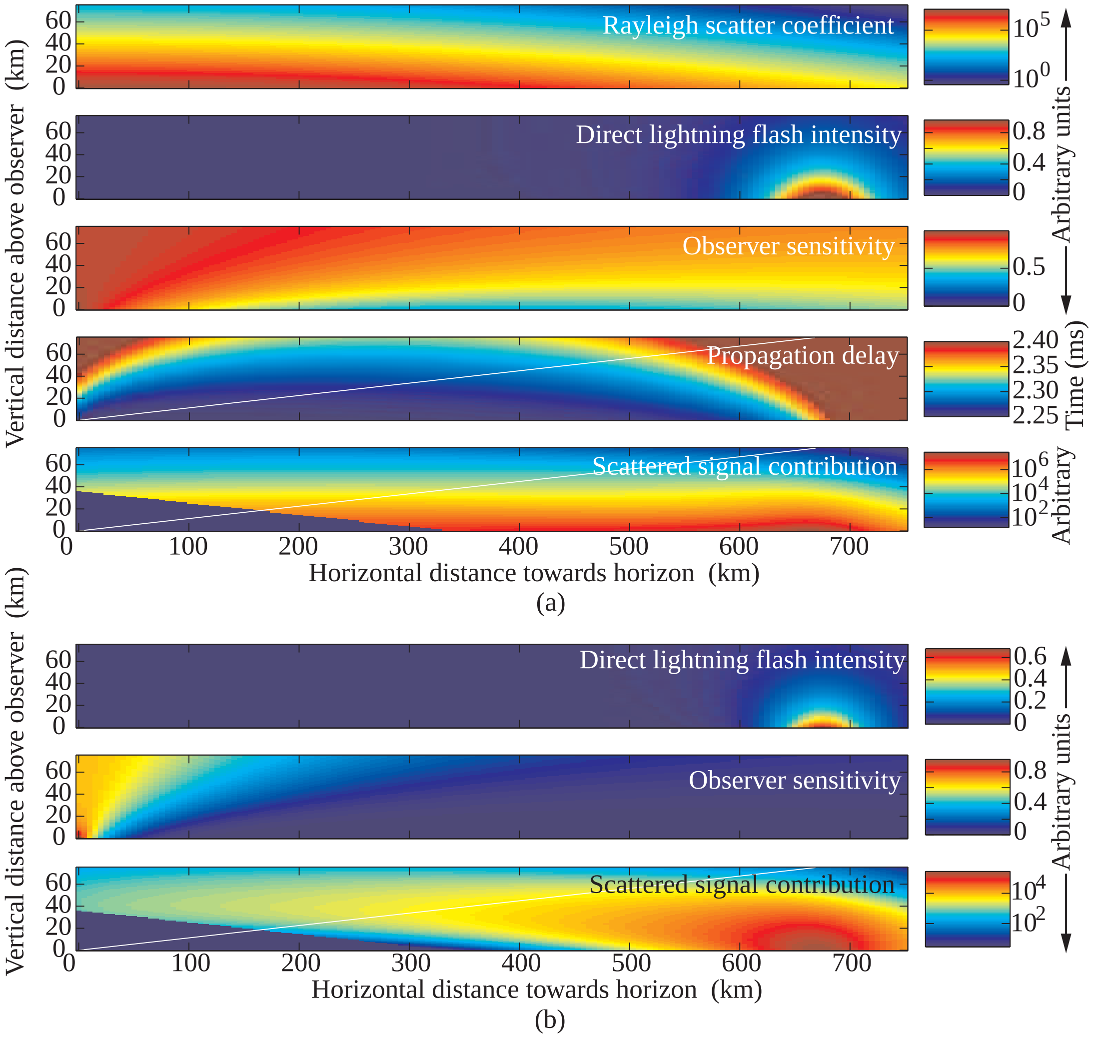

Figure 3-1: Factors affecting intensity and timing of Rayleigh-scattered lightning flashes. The observer is located at coordinates (0,0) and the observer's horizontal is aligned with the abscissa. The white lines show the viewing direction used for the cases in Figures 3-2 and 3-3. Only single-scattering is considered. (a) Scatter coefficient and calculations for red light at 700 nm wavelength. (b) Calculations for blue light at 400 nm.

The fourth plot shows the propagation time for singly-scattered light. The ground-path (that taken by a lightning sferic) propagation time for this distance is 2.25 ms. The white line indicates a typical photometer line of sight elevation of 6°. The fifth plot shows the product of the values in the second and third plots, illustrating that a Rayleigh-scattered lightning flash seen at all elevation angles comes primarily from light scattering relatively near the observer, and thus from the lower (<30 km altitude) atmosphere. As a result, the signal seen by a photometer arrives with minimal delay with respect to the causative flash (time of sferic). This observation also justifies the single-scattering assumption for red light. Figure 3-2 shows the signal which would be seen by a photometer pointed along the white line (6° elevation). There is an inevitable onset delay as compared with the radio pulse, but nevertheless an instantaneous lightning flash results in an optical signal which peaks within no more than ∼20 μs of the arrival of the sferic.

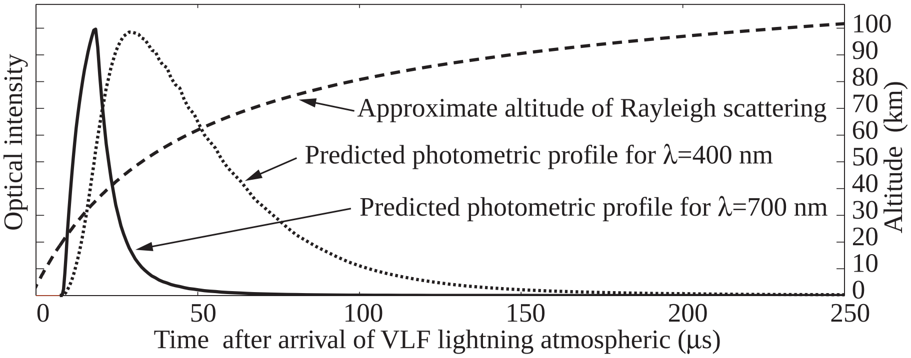

Figure 3-2: Predicted photometric signatures of a Rayleigh-scattered lightning flash. The model flash is perfectly impulsive in time.

Figure 3-1(b) shows the analogous plots for light with 400 nm wavelength, for which the Rayleigh-scatter coefficient is ∼9.9 times that for 700 nm. This case shows a qualitatively different outcome. The signal contribution shows scattering primarily near the source, and up to mesospheric altitudes, suggesting that for blue light single-scattering is likely a poor assumption, and that, therefore, optical flashes seen in blue from over the horizon should appear especially diffuse. Another way to state this difference is to say that the optical depth of the entire atmosphere looking out at 6° elevation is ∼0.35 for 700 nm light and ∼3.5 for 400 nm light. Figure 3-2 shows the modeled photometer response for a blue photometer. The delay due to scattering is at least 30 μs, and the impulsive flash is seen to be spread out considerably in time (∼70 μs).

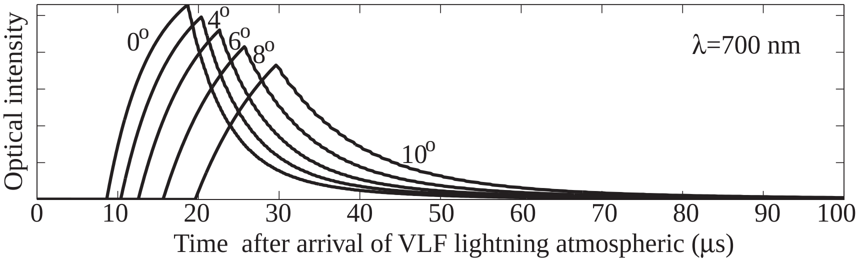

Figure 3-3: Flash onset delay variation with viewing azimuth. Values shown are for 700 nm wavelength, 675 km range, and 6.5° degree viewing elevation.

Figure 3-3 shows the results of a similar model for singly-scattered light at 700 nm but where the third dimension is included, and the dependence on the photometer viewing azimuth is investigated. This result shows that the effect of Rayleigh-scattering does add some azimuthal dispersion to an observed scattered lightning flash, but only amounting to about 10 μs for a photon directed 10° (in azimuth) away from the source lightning flash.

These simple calculations show that for red light (700 nm wavelength) the photometric onset delay with respect to the arrival of a lightning sferic is only on the order of 10 μs. Similarly, the delay between photometers viewing different azimuths up to 10° away from the lightning flash is only on the order of 10 μs. These two results are important considerations for Section 4.1, where the larger delay and azimuthal dispersion seen by a photometric array is shown to be a unique signature of elves.

The modeled time-broadening resulting from long-distance atmospheric propagation is small compared with the ~1 ms duration often seen for scattered lightning flashes when viewed towards their source azimuth. The duration and shape of such optical pulses is instead dominated by multiple elastic scattering within the clouds of the thunderstorm [*Thomason and Krider*, 1982; *Guo and Krider*, 1982].

3.2.2 Scattering and absorption as a function of wavelength

A full account of the extinction processes important at visible and near-visible wavelengths includes Mie scattering due to small aerosol particles and spectral absorption by O_2 and other species [e.g., *Erlick and Frederick*, 1998]. These complex effects are quantifiable with available models but the importance of aerosols can vary greatly with atmospheric conditions. Aerosol content cannot be easily recorded along each viewing path and at each time, leading to significant uncertainties in optical transmission properties for low viewing elevation angles.

In addition, attenuation at blue wavelengths is highly sensitive to the viewing elevation angle and to the observer altitude. Figure 3-4 shows examples of calculations using the Plexus interface to the MODTRAN3 model for atmospheric extinction.[†] Most of the observations reported in this dissertation were realized from Langmuir Laboratory, situated at ~3.2 km altitude, providing a considerable advantage over lower sites, as shown in panel (b) of Figure 3-4.

3.2.3 Atmospheric refraction

The net effect of atmospheric refraction is to elevate the apparent position of distant objects. As viewed from a given altitude, this effect varies with temperature profiles and weather conditions in the lower atmosphere, but may typically be as large as ~0.6° for objects above the atmosphere seen at the horizon from sea level. For example, this effect causes stars to set later than would be expected based on the geometry of the solid Earth.

At low viewing elevation angles, atmospheric refraction is significant for interpreting sprite and elve features, especially in video observations. In the interpretation of video images used in this dissertation, a simple empirical form for the dependence of refraction on viewing elevation angle adapted from *Montenbruck and Pfleger* [1998, p. 46] is used. A more detailed discussion of this subject may be found in the work of *Stanley* [2000, p. 141].

[†] This software was provided by Thomas M. Myers of the U.S. Army Phillips Laboratory.

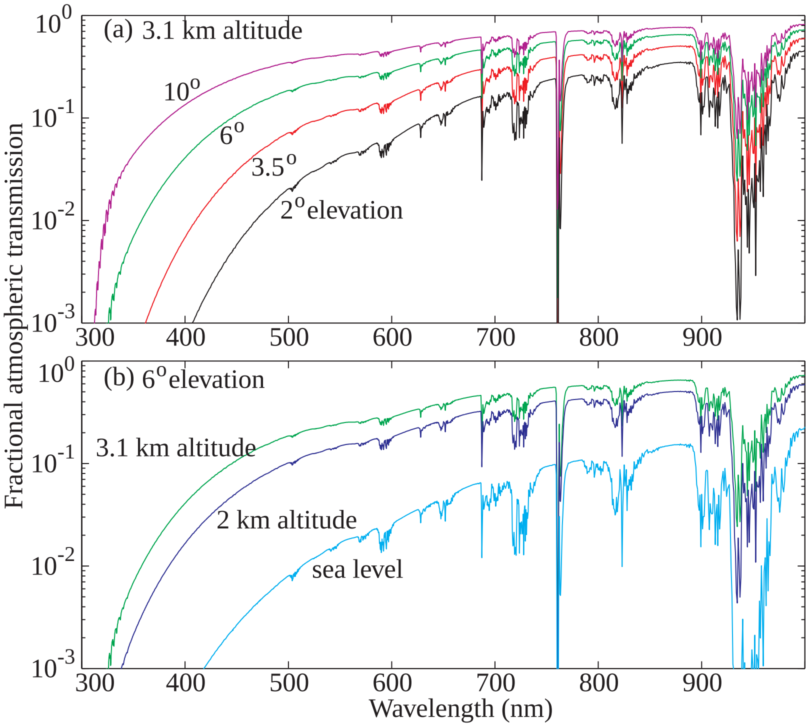

Figure 3-4: Atmospheric transmission calculated with MODTRAN3. (a) Variation with viewing elevation angle. (b) Variation with observer altitude.

3.3 Broadband photometry

Physically, the most useful and interesting quantities that one seeks to determine in quantifying upper atmospheric discharges are the electric field **E** and the electron distribution function $f(\mathbf{v})$. As mentioned in Section 1.3, direct *in situ* measurement of these or other quantities in the mesosphere and lower ionosphere is rather difficult, as is remote sensing by means of radar [*Tsunoda et al.*, 1998].

The intensity and spectrum of optical emissions from excited neutral and ionized species depend on both n_e and **E**, providing access to both of these quantities and others which can be derived from them. In the following, we consider the factors affecting long range passive optical remote sensing. A useful spectral emission line should have a radiation lifetime as fast as the variations in electric field due to a VLF pulse, for reasons discussed in Section 1.3, and fast compared to the time scale for relaxation of the electron distribution function . As it turns out, the primary emissions from elves come from excited states with lifetimes of ∼6 μs and <1 μs (Section 2.4.3), while the electron distribution thermalizes in ∼10 μs.

When enough natural signal is available, it is desirable to achieve maximum spectral, as well as temporal, resolution. Spectra of sprites have been measured [*Mende et al.*, 1995; *Hampton et al.*, 1996; *Heavner*, 2000], but the limited total optical output in elves is not conducive to spectrophotometric measurements. More practical alternatives for detecting a band of spectral lines such as $N_2(1P)$ are either to (1) use very narrow optical filters to maximise the signal to noise ratio obtainable from a single spectral line, or, if such a signal is insufficient to overcome fundamental instrument
]

noise or an adequately narrow filter is not available, (2) a broadband filter may be used to benefit from the extra signal available over several spectral lines of a given molecular band. This latter strategy was pursued for high time resolution photometry of elves, and more than one such filter is used on different photometers to achieve at least some spectral information. Section 3.3 treats the subject of broadband photometric measurements.

In the following, we define the surface brightness which is used in all optical observations reported in this dissertation, and discuss the calibration of an instrument (such as the Fly's Eye) with a broadband optical response.

3.3.1 Surface Brightness

The brightness in Rayleighs of an optical transition line is defined as [*Chamberlain*, 1978, p. 213]

$$I_k = 10^{-6} \int A_k n_k dr, \tag{3.1}$$

where n_k is the number density [cm^{-3}] of excited particles in state k, A_k is the radiation transition rate [s^{-1}] mentioned in Section 2.4.3, and the integral is taken over the line of sight [cm]. The units of I_k as given in (3.1) are 10^6 photons-s^{-1}cm^{-2}str^{-1}. The radiation is assumed to be isotropic.

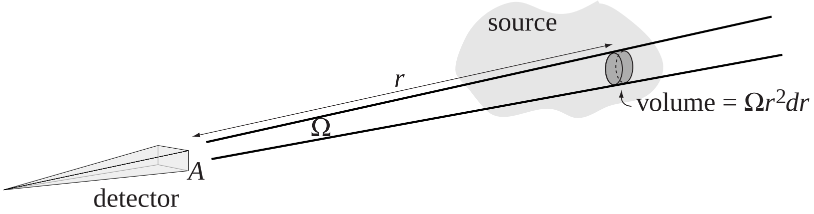

Figure 3-5: General geometry of a photometer and extended source.

A photometer with an optical aperture A and a field-of-view subtending a solid angle $\Omega \ll 1$ responds to optical emissions along its line of sight, as shown in Figure 3-5. Let a unit volume of the optical source isotropically radiate photons at rate $\mathcal{F}(\lambda)d\lambda$ in the wavelength range λ to $\lambda + d\lambda$; that is,

$$\mathcal{F}(\lambda) = \sum_k A_k(\lambda) n_k. \tag{3.2}$$

Here $A_k(\lambda)$ is now the radiation transition rate per unit wavelength [for example in units of s^{-1}nm^{-1}]. This value defines the spectrum and radiation rate for a certain spectral band, for instance that of N_2(1P) in Figure 3-6, which includes lines due to a number of vibrational substates. Note that the quantity A_k in (3.1) is in fact the rate integrated across the wavelength range of interest, i.e., $A_k = \int A_k(\lambda) d\lambda$. Photons of all wavelengths enter the detector at rate [s^{-1}]

$$\begin{aligned} \nu_{\text{det}} &= \int\int \Omega \mathcal{F}(\lambda, r) \frac{A}{4\pi r^2} T(\lambda, r) r^2 dr d\lambda \\ &= \int\int \frac{A\Omega\mathcal{F}(\lambda, r)}{4\pi} T(\lambda, r) dr d\lambda, \end{aligned}$$

where $T(\lambda, r)$ is the fraction of photons (originating at a given point) which are not scattered or absorbed before reaching the detector (see Section 3.2.2). We divide this incident photon rate by the "geometric factor" $A\Omega$ [cm^{2}str] to attain a photometer-independent measure, and by $10^6/4\pi$ for convenience to find once again the surface brightness in Rayleighs,

$$\begin{aligned} I &= \nu_{\text{det}} \frac{1}{A\Omega} \frac{4\pi}{10^6} \\ &= 10^{-6} \int \int \mathcal{F}(\lambda, r) T(\lambda, r) dr d\lambda. \end{aligned} \tag{3.3}$$

In this form the photon count rate is integrated over all wavelengths and accounts for any transmission losses.

Thus the Rayleigh unit provides a measure which is convenient experimentally, via (3.3), and which relates easily via (3.1) to theoretical calculations determining volume emission rates in given molecular bands.

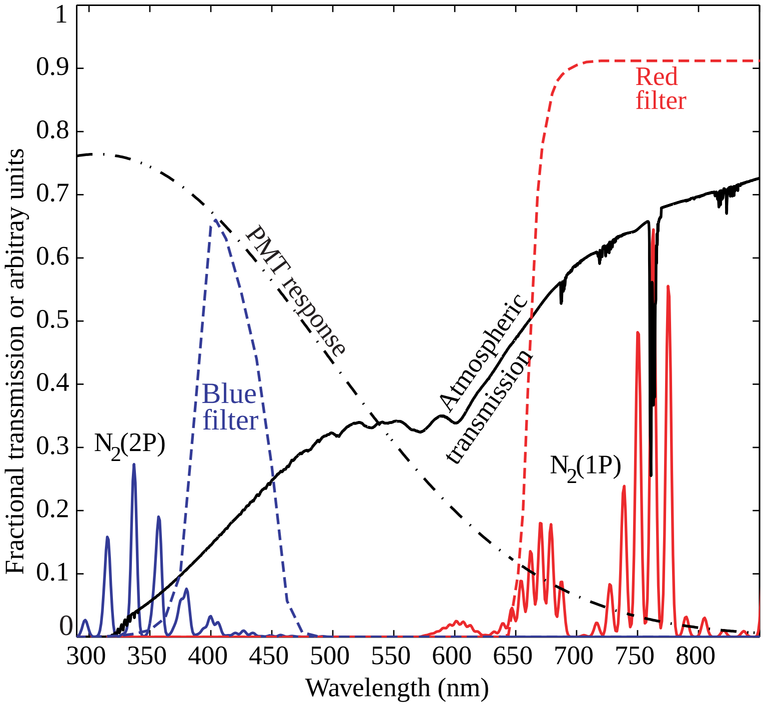

Figure 3-6: Factors affecting the photometric response to the N_2(1P) and N_2(2P) optical bands. The band fine structure represents transitions between individual vibrational substates of the electronic states which define the band. The three groups of such spectral peaks discernable in the N_2(1P) spectrum correspond to groups of transitions with the same net change in vibrational excitation number.

We note for reference that to express a surface brightness in W-cm^{-2}str^{-1}, we multiply the value in Rayleighs at wavelength λ by $(10^6/2)(\hbar c/\lambda)$, where $\hbar$ and c are the fundamental constants. We thus have,

$$\begin{aligned} 1 \text{ kR} \simeq \quad & 22.6 \text{ pW-cm}^{-2}\text{str}^{-1} \quad \text{at } \lambda = 700 \text{ nm} \\ & 39.5 \text{ pW-cm}^{-2}\text{str}^{-1} \quad \text{at } \lambda = 400 \text{ nm} \end{aligned}$$

Photometric observations are reported as an apparent brightness, without explicit knowledge or consideration of $T(\lambda, r)$. In addition, they typically represent measurements valid over a restricted wavelength range, dependent on the sensor response range. In contrast, theoretical calculations typically report emission intensities integrated over an entire spectral band, based on equation (3.1); for instance, N_2(1P) spans the wavelength range 575 nm to 2300 nm. An ideal instrument, with spectral resolution, can thus instead provide a more fundamental measure, the spectral surface brightness, given as

$$S(\lambda) = 10^{-6} \int \mathcal{F}(\lambda, r) T(\lambda, r) dr.$$

For instance, the clear night sky background for visible wavelengths is approximately 20 R-nm^{-1} without the moon and 60 R-nm^{-1} with a full moon [Gary Swenson, *private communication,* 1995]. Note that $I = \int S(\lambda) d\lambda$.

3.3.2 Calibration

A real photometer responds with a count rate somewhat less than that given by equation (3.3), depending on the quantum efficiency of the detector. The voltage response V_{obs} of a photosensitive device, for instance the anode of a photomultiplier or a pixel of an intensified CCD, is given by

$$V_{\mathrm{obs}} = G_{V_{\mathrm{H}}} \frac{10^6}{4\pi} A\Omega \int_{\lambda} S(\lambda) f(\lambda) q(\lambda) d\lambda \tag{3.4}$$

where

$G_{V_{\mathrm{H}}}$ is the gain, measured in volts per photoelectron-s^{-1}, of the proportional photometer (and amplifier) when operated with a high-voltage of V_{H},

$A\Omega$ is the geometric factor for the photometer, where A is its aperture and Ω is the smaller of the solid angles subtended by either the photometer's field-of-view or the extent of the light source,

$S(\lambda)$ is the apparent spectral surface brightness at wavelength λ, measured in Rayleighs (R) per nm,

$f(\lambda)$ is the fractional transmittance of any optical filters, and

$q(\lambda)$ is the quantum efficiency of the photometer's photocathode.

When making broadband optical measurements of a source whose optical output may vary with wavelength, we cannot unambiguously determine the optical intensity if the instrumental $q(\lambda)$ also varies with wavelength. Thus to express experimental intensities based on (3.4) we assume that

$$S(\lambda) = I \, \delta(\lambda - \lambda_0) \tag{3.5}$$

where $\delta(\cdot)$ is the Dirac delta function and λ_0 is an appropriate wavelength which dominates the integral in (3.4). Observations can then be calibrated and expressed at the chosen wavelength λ_0 by

$$\begin{aligned} I_{\lambda_0} &= \frac{V_{\mathrm{obs}} G_{V_{\mathrm{H(cal)}}} [A\Omega]_{\mathrm{cal}} \int S^{\mathrm{cal}}(\lambda) f(\lambda) q(\lambda) d\lambda}{G_{V_{\mathrm{H(obs)}}} [A\Omega]_{\mathrm{obs}} \, f(\lambda_0) q(\lambda_0) V_{\mathrm{cal}}} \\ &= \alpha_{\lambda_0} V_{\mathrm{obs}} \frac{G_{V_{\mathrm{H(cal)}}}}{G_{V_{\mathrm{H(obs)}}}} \\ &= \alpha_{\lambda_0} V_{\mathrm{obs}} \left(\frac{V_{\mathrm{H(cal)}}}{V_{\mathrm{H(obs)}}} \right)^{\epsilon} \end{aligned} \tag{3.6}$$

where we have assumed that $G_{V_{\mathrm{H}}}$ is proportional to $(V_{\mathrm{H}})^{\epsilon}$ for some ϵ, as is true for electron multipliers such as photomultipliers or multichannel plates, and we have defined the calibration factor

$$\alpha_{\lambda_0} \equiv \frac{[A\Omega]_{\mathrm{cal}} \int S^{\mathrm{cal}}(\lambda) f(\lambda) q(\lambda) d\lambda}{[A\Omega]_{\mathrm{obs}} f(\lambda_0) q(\lambda_0) V_{\mathrm{cal}}}. \tag{3.7}$$

Here the value I_{λ_0} is averaged over the entire field-of-view of the photometer or pixel.

In summary, to calibrate a broadband photometer we must choose an appropriate wavelength λ_0 which dominates the integral in (3.4), determine the calibration factor α_{λ_0} for that wavelength, and determine the instrument gain behavior (e.g. the value of ϵ) in order that a variety of gains can be used in observations.

3.3.3 Band brightness at the source

The measure of optical intensity discussed above is used in this work because, although not an accurate count of photon flux, it does not require any assumptions about the optical spectrum under observation. However, as can be seen from Figure 3-6, the expected responses to sprite luminosity in our instrument are dominated by narrow spectral ranges. For blue photometers sensitive to the N_2(2P) band, the dominant wavelength region is near 375 to 400 nm and is determined mostly by the competing factors of the atmospheric transmission and the blue filter response. For red photometers, the PMT (photocathode) response and the longpass red filter select a portion of the N_2(1P) spectrum near 700 nm. The dominance of a narrow spectral region in each photometer justifies the use of equation (3.5) and endows the measure I_{λ_0} with physical significance. I_{λ_0} can be taken to be an approximate measure of the true brightness near the dominant optical wavelength λ_0.

A more direct experimental comparison with the theoretical surface brightness of equation (3.1) can be made if (1) one band strongly dominates the instrument response, (2) its spectrum $A_k(\lambda)$ is known, and (3) the atmospheric transmission $T(\lambda, r)$ is known.

From these assumptions and equations (3.2), (3.4), (3.5), and (3.6), the total source brightness in band k can be inferred from a wideband measurement:

$$I_k = A_k I_{\lambda_0} \frac{f(\lambda_0) q(\lambda_0)}{\int A_k(\lambda) T(\lambda, r) f(\lambda) q(\lambda) d\lambda}$$

In a similar manner, the relative excitation rate of two bands can be assessed through two-color photometry. For instance, the red and blue optical filters shown in Figure 3-6 can be used to assess the average excitation ratio of states $C^3\Pi_u$ and $B^3\Pi_g$ through their emissions in the N_2(1P) and N_2(2P) bands.

$$\begin{aligned} \left\langle \frac{n_{C^3\Pi_u}}{n_{B^3\Pi_g}} \right\rangle &\equiv \frac{\int A_{N_2 1P}\, n_{C^3\Pi_u} dr}{\int A_{N_2 2P}\, n_{B^3\Pi_g} dr} \\ &= \frac{I_{700}}{I_{400}} \, \frac{f(700\ \mathrm{nm}) q(700\ \mathrm{nm})}{f(400\ \mathrm{nm}) q(400\ \mathrm{nm})} \, \frac{\int A_{N_2 2P}(\lambda) T(\lambda, r) f(\lambda) q(\lambda) d\lambda}{\int A_{N_2 1P}(\lambda) T(\lambda, r) f(\lambda) q(\lambda) d\lambda} \end{aligned} \tag{3.8}$$

where I_{700} and I_{400} are observed surface brightnesses expressed according to equation (3.6) for wavelengths 700 nm and 400 nm.

3.4 The Fly's Eye

The Fly's Eye photometric array was specifically designed to detect the optical emission wavelengths and space-time development predicted for elves. The spectral emissions were expected to be

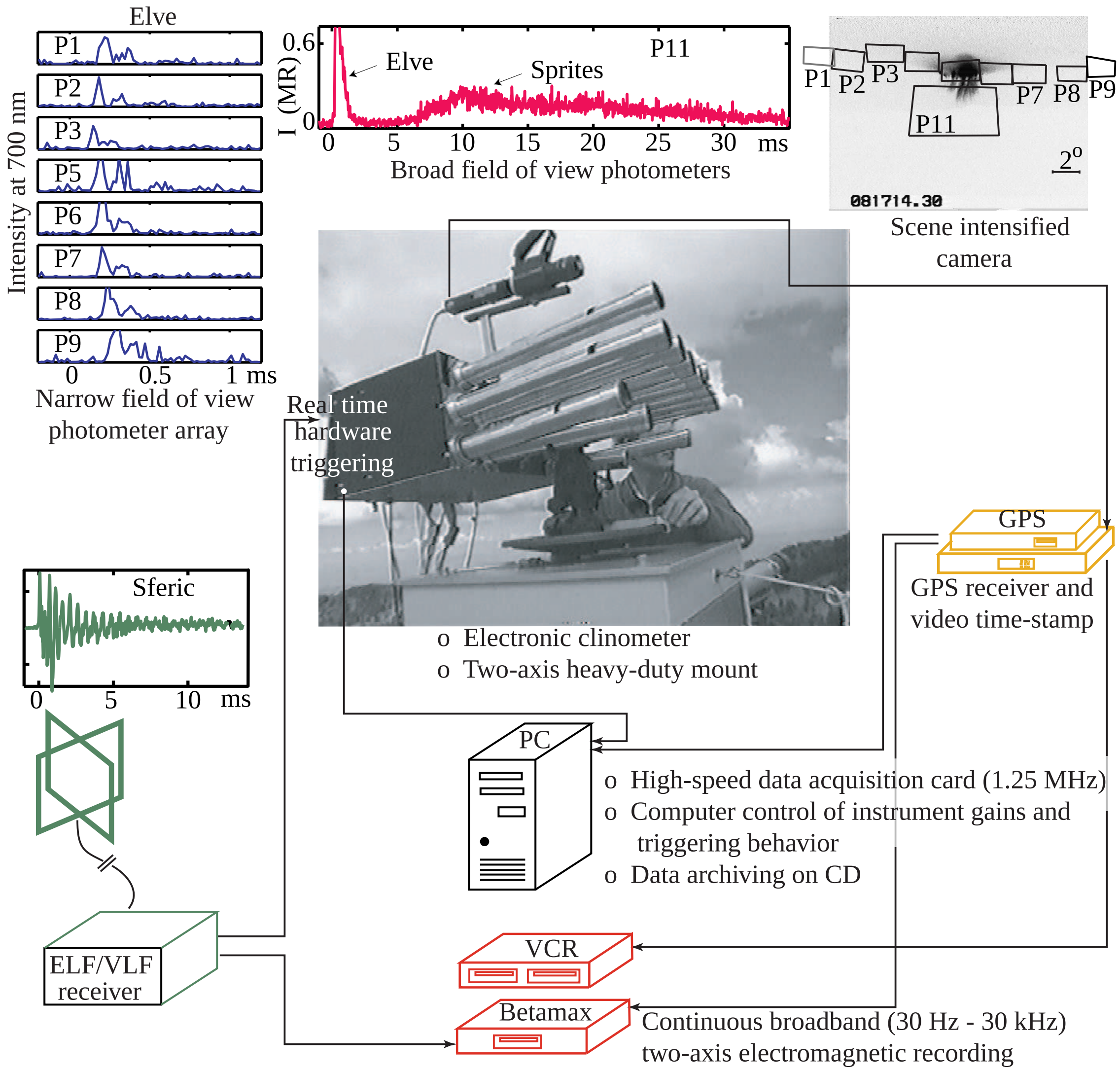

Figure 3-7: Overview of the Fly's Eye photometer array. The center image shows the photometric array, intensified CCD video camera, triggering electronics box (which includes signal filters, analog trigger circuitry, digital triggering logic, and high voltage control circuitry), and the author.

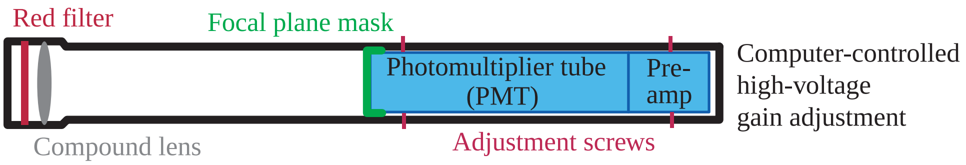

Figure 3-8: A single photometer of the Fly's Eye array. P1-P9, P11, and P13 bear red filters, while P10 and P12 bear blue ones.

dominated by N_2(1P) [*Taranenko et al.*, 1993b], especially as observed from the ground (Figure 3-6). The primary temporal and spatial requirement was to resolve an apparent motion of luminosity over ~200 km in ~1 ms [*Inan et al.*, 1996c]. To resolve such an event with 10 detectors from a range of 500 km (a typical distance for demonstrated successful observation of sprites overlying distant storms) requires a temporal resolution of ~50 μs and an angular resolution in at least one dimension of ~2.3°.

An elegant arrangement to achieve such a measurement would be to use one large lens to image the sky onto an array of focal plane detectors. However, because of the difficulty in obtaining an appropriately large and convex (Fresnel) lens, and moreover because of the advantage of being able to have truly contiguous and even overlapping detector fields-of-view of arbitrary shape and varying sizes, separate optics were built for each detector. Photodiodes, photomultiplier tubes (PMTs), and charge-coupled devices (CCDs) could all have met the speed criterion, but photodiodes have inferior sensitivity and the cost and time required to develop a custom CCD high-speed clocking circuit were prohibitive.

Figure 3-9: The Fly's Eye deployed at Langmuir Laboratory. The Fly's Eye (shown here with the video system removed and with fellow student Elizabeth Gerken) is mounted on a rack which contains power supplies and the control/data acquisition computer. The video recorders and the GPS receiver are located inside the laboratory.

Figure 3-7 shows a schematic overview of the Fly's Eye instrument designed and built by the author, and Figure 3-9 shows the instrument deployed at Langmuir Laboratory. Nine individually mounted photometers (P1-P9) provide the angular resolution (∼2.2°) to resolve flash features 20 km wide at a range of 500 km, and four additional photometers (P10-P13) survey larger fields-of-view. Each detector consists of a single compound lens, optical filter, and a Hamamatsu HC-124-01 or HC-125-01 PMT with built-in transimpedance preamplifier, as shown in Figure 3-8. The pointing direction of each photometer is determined by its mechanical mount, and the shape of its field-of-view is determined by a focal plane mask. The PMT photocathodes are sensitive between 185 nm and 800 nm wavelength (see PMT response curve in Figure 3-6), in and near the visible range. Two different kinds of optical filter, detailed in Figure 3-6, are used on different photometers, and may be used to determine excitation ratios, as outlined in Section 3.3.3. Empirical determination of the photometer responses and fields-of-view is discussed in Sections 3.4.1 and 3.4.2.

In addition to the thirteen amplified photometer signals, the Fly's Eye includes an Applied Geomagnetics two-axis electronic clinometer used to record automatically the viewing elevation angle, and receives one or two sferic channels from an ELF/VLF (30 Hz to 25 kHz) receiver (Figure 3-7). Using custom software developed in Visual C++, these sixteen signals (or any chosen subset) are sampled continuously in a circular buffer by two National Instruments PCI-MIO-16E-1 data acquisition boards using differential inputs in a Windows NT computer. Sample periods for each channel varied from 30 μs in 1996 to 10 μs in 1999 as the computer hardware was upgraded each year. Acquisition cycles (one per event) are started using a global positioning system (GPS) 1 Hz pulse for precise time synchronization. Trigger circuitry for several photometers and a sferic channel is used to trigger the software to save a specified portion of pre-trigger and post-trigger data from the circular buffer. In 1999 the sferic trigger circuitry included a high-pass filter and rectifier in order to respond to VLF pulses of either polarity. Typically 1 to 2 seconds of data are recorded for each trigger event. After a trigger, the data acquisition system does not record data until the next GPS second begins.

3.4.1 Pointing Calibration

The pointing direction of each photometer is mechanically fixed with respect to the Fly's Eye's base. The focal plane screen on each photocathode sets the size and shape of the field-of-view. Small adjustments can be made to its position by means of the adjustment screws holding the photomultiplier assembly (Figure 3-8).

In order to quantify the actual fields-of-view once the array was built, the photometer angular responses and fields-of-view were calibrated by scanning the Fly's Eye in azimuth and elevation past a fixed light source. Because the Fly's Eye photometers are mounted up to >50 cm apart from each other, parallax (i.e., the difference in the apparent direction of an object as seen from two different points) is more significant than 0.1° for light sources closer than ∼300 m. The calibration light source with small (1 cm×1 cm) aperture and steady output was placed ∼360 cm from the Fly's Eye. Intensities in each photometer were recorded for a large number of electronically recorded elevations and at azimuths every 0.5°. Knowledge of the precise geometry of the Fly's Eye photometers was used to correct for parallax. The position of each aperture with respect to the elevation (θ) and azimuth (ϕ) rotation axes was used to calculate, for each measurement and each photometer, the effective elevation and azimuth for a light source at infinite range. Figure 3-10 shows an example of the parallax in photometer 1 for one position of the Fly's Eye. The rotated locations $\mathbf{r}'_{\mathrm{i}}$ of the apertures were calculated in a cartesian coordinate system centered at the intersection of the rotation axes. Positions $\mathbf{r}_{\mathrm{i}}$ of the apertures for zero elevation and at a reference azimuth were measured, and

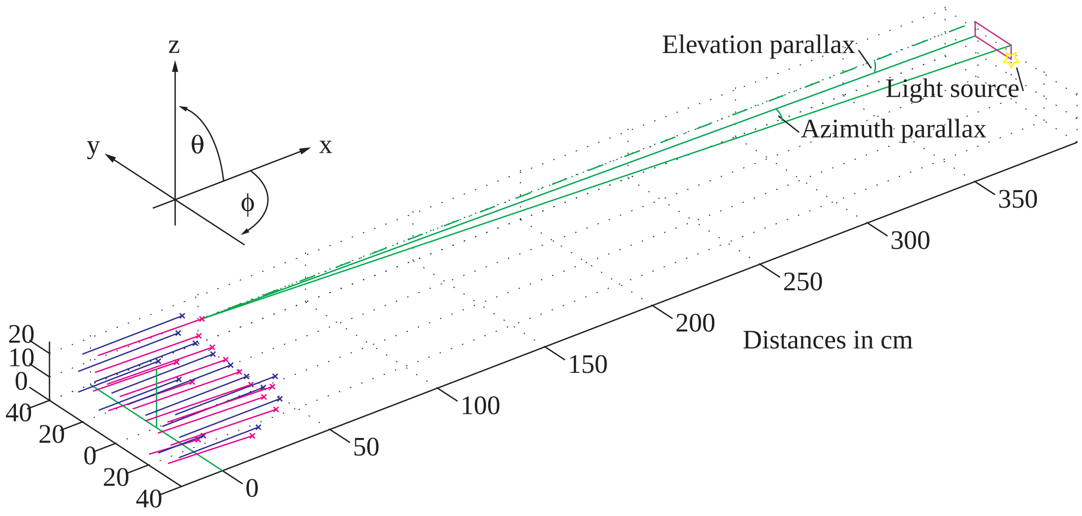

Figure 3-10: Parallax in pointing calibrations. The blue lines terminated with ×'s show the locations of photometer apertures for ϕ=0, θ=0. Altered positions after a sample rotation of the Fly's Eye are shown in magenta. For nearby light sources parallax occurs due to the finite separation of the apertures.

$\mathbf{r}'_{\rm i}$ were calculated as

$$\mathbf{r}'_{\rm i} = \begin{pmatrix} \cos\theta\cos\phi & \sin\phi & \sin\theta\cos\phi \\ -\cos\theta\sin\phi & \cos\phi & -\sin\theta\sin\phi \\ -\sin\theta & 0 & \cos\theta \end{pmatrix} \mathbf{r}_{\rm i}$$

The effective azimuth $\phi^i_{\rm eff}$ and elevation $\theta^i_{\rm eff}$, corrected for parallax, are then given by

$$\begin{aligned} \cos\phi^i_{\rm eff} &= \frac{\hat{\mathbf{x}} \cdot \mathbf{P}_{\rm xy}(\mathbf{r}_{\rm s} - \mathbf{r}'_{\rm i})}{\|\mathbf{P}_{\rm xy}(\mathbf{r}_{\rm s} - \mathbf{r}'_{\rm i})\|} \\ \cos\theta^i_{\rm eff} &= \frac{\hat{\mathbf{x}} \cdot P_{xz}(\mathbf{r}_{\rm s} - \mathbf{r}'_{\rm i})}{\|\mathbf{P}_{\rm xz}(\mathbf{r}_{\rm s} - \mathbf{r}'_{\rm i})\|} \end{aligned}$$

for each photometer i. Here $\mathbf{r}_{\rm s}$ is the position of the light source; $\hat{\mathbf{x}}$ is a unit vector pointing along the direction of $\phi = 0$, $\theta = 0$; $\mathbf{P}_{\rm xy}(\mathbf{r})$ denotes a projection of $\mathbf{r}$ onto the plane where $\theta = 0$; and $\mathbf{P}_{\rm xz}(\mathbf{r})$ denotes a projection of $\mathbf{r}$ onto the plane where $\phi = 0$.

The resulting data giving measured photometric intensities at viewing directions ($\phi^i_{\rm eff}$, $\theta^i_{\rm eff}$) were gridded for each photometer and contours of the measured sensitivity are shown in Figure 3-11. The fields-of-view do not quite correspond to the ideal design arrangement. However, once characterized, the particular field-of-view arrangement can be taken into account in detailed data analysis such as that given in Sections 4.3 and 5.1.4. Figure 3-11 shows the fields-of-view in 1998. Prior to 1998, the blue photometers P10 and P12 roughly overlaid P2 and P8, respectively, but were ~3 times as large.

Figure 3-12 shows a cross-section along the azimuth and through the peak of each photometer response in order to demonstrate the low "cross-talk" attained with the focal plane masks. Outside the ~2° horizontal fields-of-view of the narrow photometers P1 to P9 the response remains below the peak response by a factor of 25 to more than 100. P4 satisfies this criterion but is highly saturated at the levels used in this calibration.

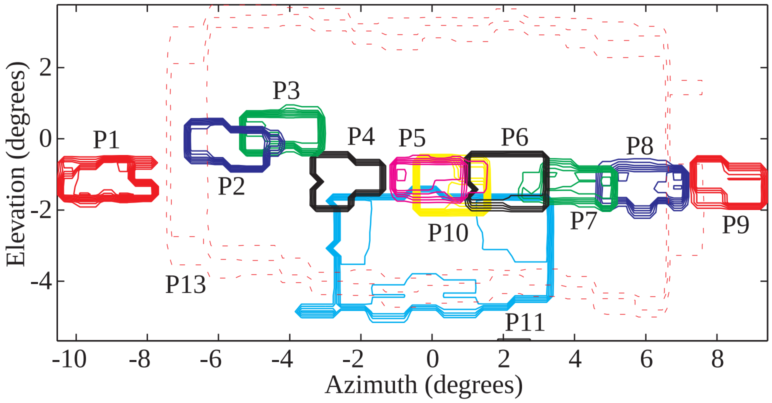

Figure 3-11: Calibrated photometer fields-of-view in 1998. The data have been gridded to 0.5°×0.5° resolution. The elevation corresponds to that read by the electronic clinometer.

3.4.2 Intensity Calibration

Overall gains in the Hamamatsu PMT assemblies, as tested by the manufacturer, varied by two orders of magnitude from one unit to another. Values for $\alpha_{700\,\mathrm{nm}}$ and $\alpha_{400\,\mathrm{nm}}$ were determined in accordance with equation (3.7). A calibrated Hoffman Engineering Corporation Spectral Radiance Standard with known spectrum was used as a light source, and the integral in equation (3.7) was carried out over the filter responses shown in Figure 3-6. The values for Ω_{obs} were taken from the pointing calibration described above.

Surface brightnesses are subsequently expressed in kiloRayleighs (kR) at 700 nm for photometers bearing a red filter (P1 to P9, P11, and P13) and at 400 nm for those with a blue filter (P10 and P12).

3.5 Intensified CCD video recordings

The photometer array was bore-sighted with an image intensified (Varo Noctron V) black and white Pulnix video system with a field of view of $\sim 20° \times 14°$. The video frames were time coded with a True Time GPS timing system and recorded on standard VHS videotape. The bore-sighted video recordings were essential to documenting the location in the sky viewed by the Fly's Eye photometers in all of the observations presented in this dissertation. In this section, we describe essential features of the video recordings.

3.5.1 GPS time stamping

NTSC video cameras can be clocked in "frame" or "field" mode. The Fly's Eye CCD camera operates in the frame mode. As shown in Figure 3-13, each field, consisting of even or odd interlaced scan lines, is exposed for ~33 ms, and the two fields composing a frame overlap by ~17 ms and together encompass ~51 ms.

Before being recorded to video tape, the video signal is passed through a GPS-based time marking system, which imprints the date and time at the end of the first field's exposure onto both fields of each frame.

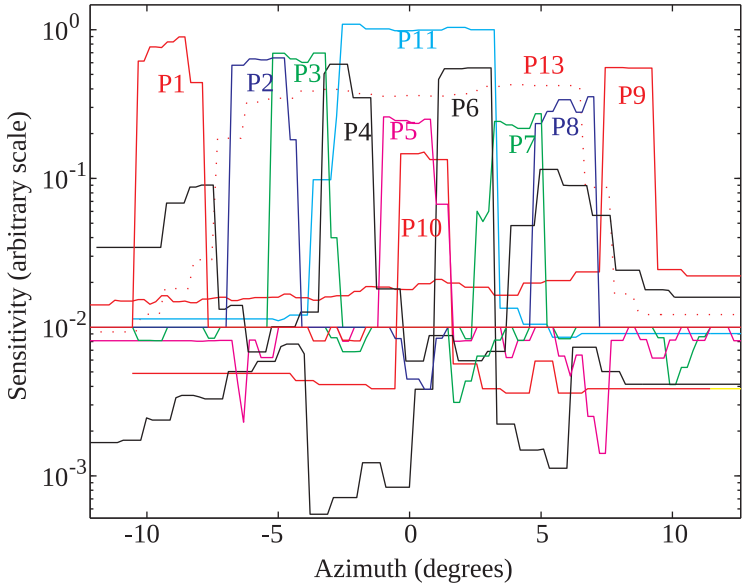

Figure 3-12: Cross-section of the Fly's Eye photometer responses.

3.5.2 High speed video

Data obtained with a variable-speed, triggered, image-intensified video system are presented in Section 5.1. This system was borrowed and operated in 1997 by Mark Stanley of the New Mexico Institute of Mining and Technology. Observations were made using frame rates of up to 4000 s^{-1} in a manually-triggered mode. The camera and an overview of observations are described in *Stanley et al.* [1999].

3.5.3 Star-field matching

While the Fly's Eye electronically measures and records its pointing elevation, the pointing azimuth was recorded by hand, and any roll in the camera alignment was not recorded during typical observations.

A more direct method of determining the pointing is through post-processing of the video images in conjunction with a star catalogue. A Matlab software package named VIDEOTOOL was written to partially automate the matching of stars in a video sequence taken at a known time and location with stars from an electronic catalogue. The relationship between video pixel coordinates (x, y) and azimuth/elevation coordinates (ϕ, θ) is determined using a number of star positions approximately satisfying

$$\begin{pmatrix}\phi\\ \theta\end{pmatrix} \simeq \begin{pmatrix} a & b\\ c & d\end{pmatrix}\begin{pmatrix}x\\ y\end{pmatrix} + \begin{pmatrix}\phi_o\\ \theta_o\end{pmatrix}. \tag{3.9}$$

This transformation allows the pointing elevation and azimuth, the video field-of-view height and width, and any axial rotation of the camera to be determined. It does not allow for lens distortions or edge effects, nor a determination of atmospheric refraction as a function of elevation. It addition it should be noted that at high viewing elevations, a rectilinear mapping of image coordinates to azimuth and elevation is inappropriate [Mark Stanley, *private communication*, 1997].

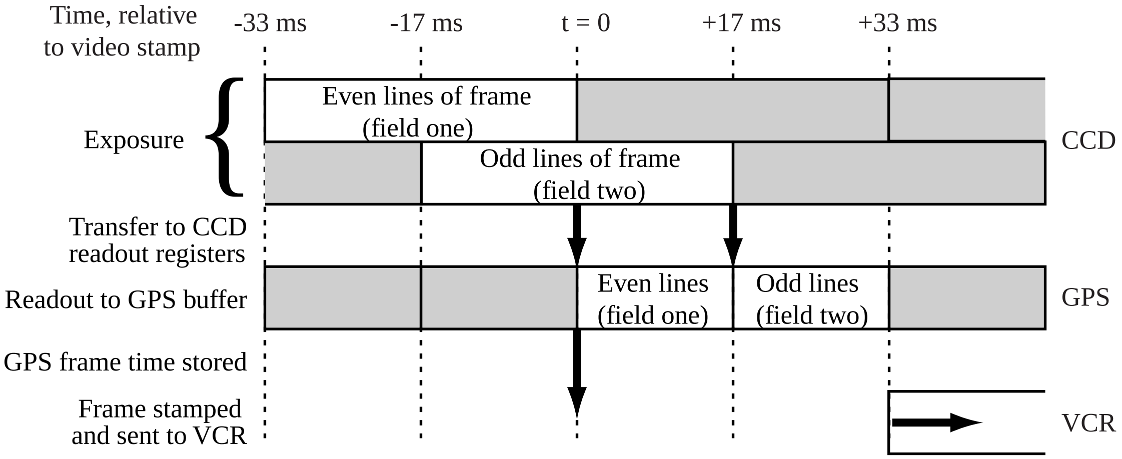

Figure 3-13: CCD exposure timing for a frame-mode camera.

Star positions were obtained from the PPM (positions and proper motion) Star Catalogue, including a 1993 Bright Stars Supplement. This catalogue is available from the Astronomical Data Center and includes 378,000 stars. Star elevations and azimuths from the observation site are calculated for each video event time, assuming a simple form for atmospheric refraction (Section 3.2.3). The videoTool program helps the user graphically select a set of matching stars in the the starfield projection and in a video image. Six or more stars are used in a least-squares fit to equation (3.9).

To increase the signal to noise ratio in the video image, at least ten frames not containing sprites or elves are averaged before the fit. Figure 3-14 shows an example of this procedure. Because the Fly's Eye records the pointing elevation of its photometric array, which is not subject to the axial rotation sometimes present in the camera, the measured photometer fields-of-view (Figure 3-11) can be plotted over the video image when the pointing azimuth of the Fly's Eye's mount is also precisely recorded during observations. In addition, if a lightning discharge located by NLDN has been associated with the video event, an altitude scale showing the local vertical directly overlying the lightning is plotted (Figure 3-14d). These altitudes refer only to events directly overlying the cloud-to-ground discharge, whereas sprites are known to occur with horizontal displacements of up to 50 km from temporally proximal lightning [e.g., *Lyons*, 1996].

Optical calibration of intensified video recordings using crude stellar luminosity data in the PPM catalogue was attempted without success. However, *Heavner* [2000, p. 93 and *private communication*] has successfully implemented such a strategy using the stellar databases of *Johnson and Mitchell* [1975] and *Jacoby et al.* [1984]. These databases can easily be integrated into existing videoTool software to allow *post facto* video intensity calibration without knowledge of the intensifier high voltage setting. In this dissertation, we extract absolute intensities based on photometer calibration data as described in Section 3.3.

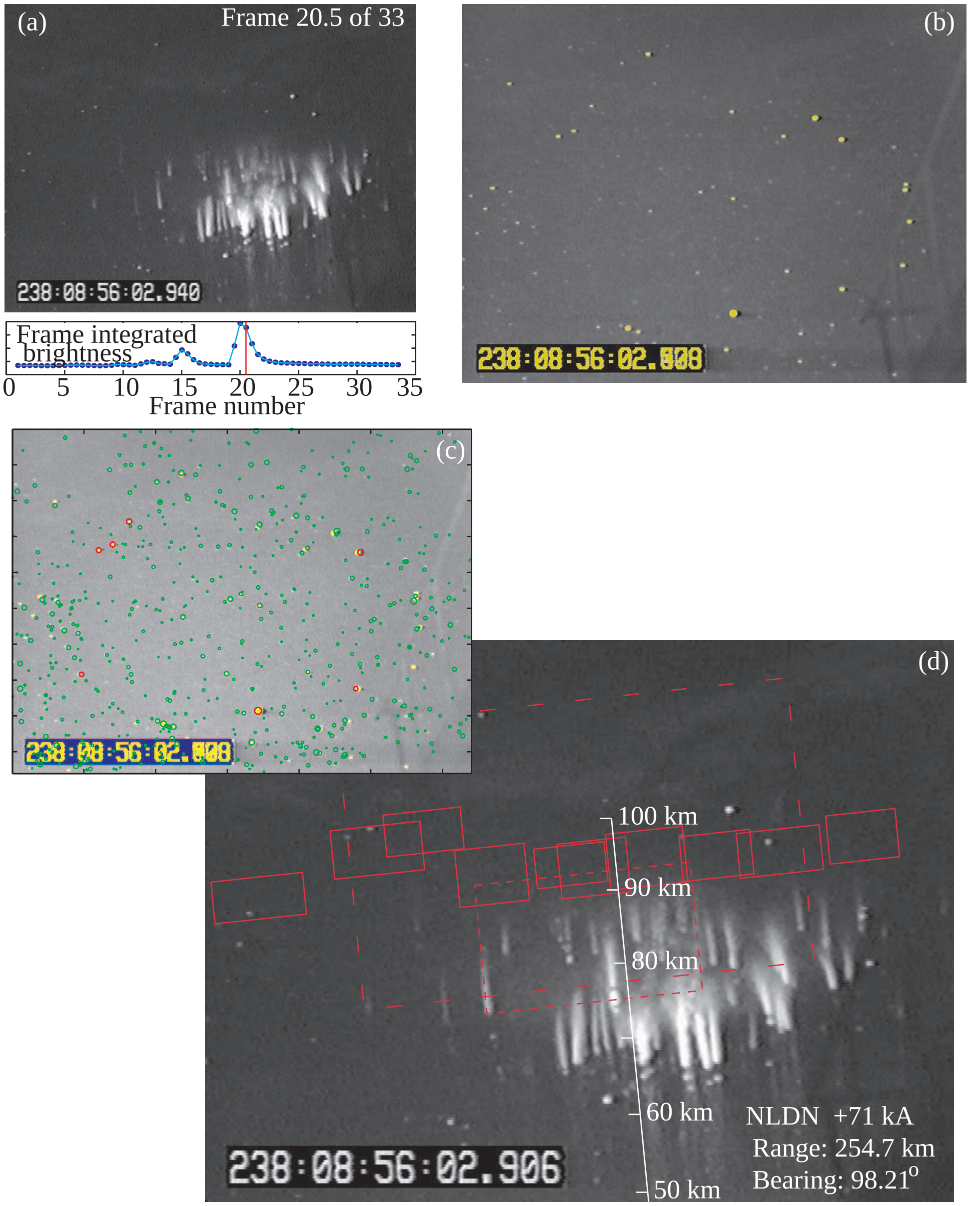

Figure 3-14: Pointing determination using star fields. (a) A single video field of a sprite sequence. In order to resolve the stars visible at this time, ~10 frames from before the event are averaged to produce (b). A starfield matching program is used to interactively select and fit known stars to the image. In (c), known star positions are overplotted in green, and those used in the least-squares fit are shown in red. (d) The original image with superposed pointing information.

Chapter 4

Photometry of Elves

In this chapter we describe the application of the Fly's Eye (Section 3.4) to the detection and characterization of elves. Section 4.1 deals with methods of identifying elves based on their optical characteristics, and subsequent sections report statistical data on observed elves. Results are fully consistent with the theoretical model described in Section 2.5 and suggest a lightning peak current threshold near ∼60 kA for the excitation of optically detectable elves.

4.1 Identification of lightning, elves, and sprites

Previously elves were identified only using video imagery or wide field-of-view photometry [*Fukunishi et al.*, 1996b], allowing limited information on their characteristics and providing poor discrimination between elves and the optical flash due to scattered light from the parent lightning (Section 3.2.1). With wide field-of-view photometers, both of these phenomena appear as a ∼1 ms flash, while with video systems they may appear as broad luminosity in a single field or frame.

In this work a more detailed and unique signature of elves in a horizontal photometric array is deduced from the model predictions described in Section 2.5. In the following sections, the discovery of the signature in 1996 is discussed, and its features are contrasted with those of scattered lightning flashes. A comparison between signatures of elves and sprites in the Fly's Eye and other photometric arrays is deferred until Chapter 5.

4.1.1 Modeled optical signatures

Due to the competing factors of obscuration by the causative storm clouds and extinction at the horizon, elves and sprites have been most frequently observed from the ground at ranges of 300 to 800 km. At such ranges, the causative storm system is well below the observer's horizon, and lightning is not directly visible. Nevertheless, sprites, elves, and scattered light from lightning may be detected optically, and ELF/VLF impulsive electromagnetic emissions (sferics) from lightning and possibly sprites may be detected with radio receivers (Section 3.1). Simple geometric considerations shown in Figure 4-1 indicate that the radio emission (sferic) due to the lightning, propagating in the Earth-ionosphere waveguide essentially at the speed of light, reaches an observer before any optical flash originating in the mesosphere or ionosphere. Moreover, in the case of elves, light from the outer limb of an elve reaches the observer before emissions from the elve's inner portion, even though photons from the inner region are emitted first. An equivalent description of this interesting effect is that the edge of the luminous elve expands outward at a speed greater than that of light.

For an observer with a limb view, this property causes "temporal focusing" of the front half ("front") of the flash and "temporal defocusing" in the distant half ("back") of the elve [*Inan et al.*, 1996c].

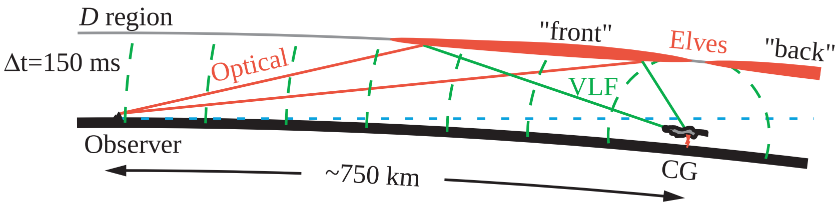

Figure 4-1: Geometry for photometric observations of elves at 500 to 900 km range. Of the two VLF/optical paths shown, the one seen by the observer at a higher elevation angle is shorter. Light from this path arrives ~150 μs after the radio sferic but before light from the longer, lower elevation path. The thunderstorm is beyond the observer's horizon, which is indicated by the straight dashed line. The EMP pulse due to lightning is very short compared with the propagation time across the radius of the elve, so that the luminous region is at any instant actually in the form of a thin annulus rather than a disc.

For an observer on the ground, the flash appears to drop in altitude and spread outward with time. While the EMP pulse, and therefore the optical flash emitted at any location, may last only tens of microseconds, light is emitted from different regions for >1 ms as the EMP propagates radially outward (see Figure 2-5 on page 28).

Using the modeled optical emissions described in Section 2.5, a detailed prediction can be made for the optical form of an elve observed from any location. By taking into account the propagation delays and the contribution to each viewing direction at each point in time, the evolution shown in Figure 4-2 was predicted for the event described in Figure 2-5.

4.1.2 Observed photometric signatures

A telltale signature based on the rapid development of the flash shown in Figure 2-5 was documented using the "Fly's Eye" [*Inan et al.*, 1997]. By aiming well above the ionospheric *D* region overlying a strong CG, this array is used to identify unambiguously the optical emissions from elves. Based on the short (~150 μs) delay between reception of the sferic, and reception of the first photometric signature from the ionosphere, the optical emission can be located to be hundreds of km from the lightning (see discussion in Section 4.3). This timing constrains the physical mechanism to be one involving speed-of-light propagation only [*Inan et al.*, 1997].

Observations on 24 July 1996

Observations carried out with the Fly's Eye on 22 July 1996 were particularly clear and were the first reported results [*Inan et al.*, 1997] from the Fly's Eye instrument, and are described in this section.

On 22 July 1996, a large mesoscale convective system ~650 km southeast of the Yucca Ridge Field Site (40.67°N, 104.93°W) produced many sprites and was observed at Yucca Ridge unimpeded by any intervening clouds. At this distance the ground under the storm was ~35 km below the horizon from Yucca Ridge (see Figure 4-1) so that neither the cloud-to-ground nor intracloud flashes produced by the storm, nor their cloud-scattered light, were visible from Yucca Ridge. Figure 4-4 shows the first video frame of a sprite event observed coincident in time (within ~30 ms) with a positive CG discharge of estimated peak-current +150 kA occurring at 669 km from Yucca Ridge at 07:17:38.767 UT, as recorded by the National Lightning Detection Network.

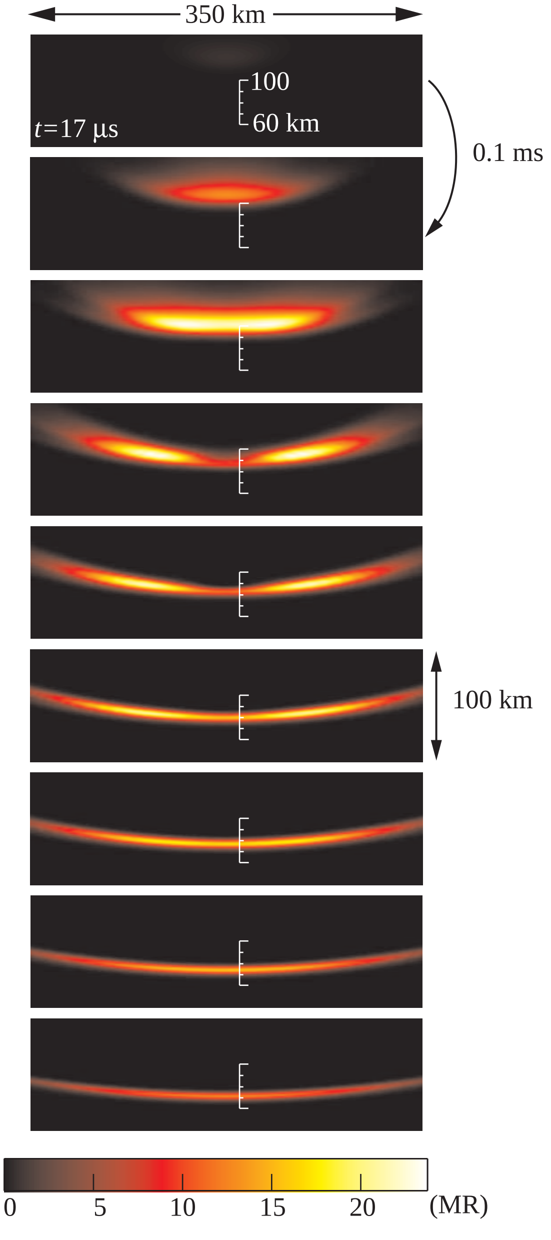

Figure 4-2: Modeled view of elves from the ground. Panels show 10 μs-long snapshots (every 100 μs) of the modeled luminosity in the event detailed in Figure 2-5 as seen from the ground 745 km away from the causative lightning. The color scale shows intensity of emission in the N_2(1P) band. The first snapshot begins 17 μs after the lightning sferic is received at the observer location.

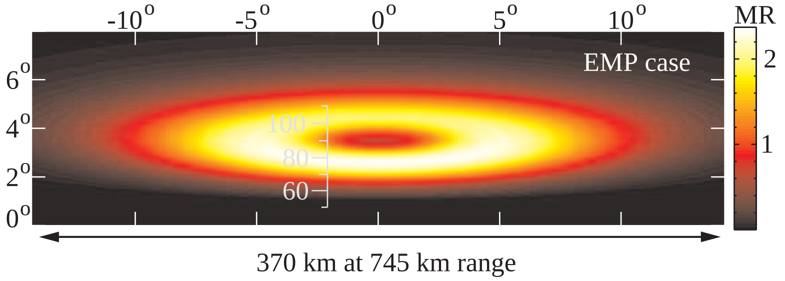

Figure 4-3: Integrated model view of elves from the ground. The modeled flash of Figure 4-2 is shown integrated over 2 ms.

At 07:17:38.769 UT the onset of an intense VLF radio atmospheric ('sferic' for short) was observed (Figure 4-5, top panel) followed in ∼150 μs (in agreement with the path length difference as discussed above) by a bright pulse in the center of the top row of photometers (Figure 4-5, middle panel). Photometer 11 detected the same event (Figure 4-5, lower panel) but also showed a less intense but longer lasting luminous event starting ∼7 ms after the sferic onset. This second event is interpreted as the sprite itself, occurring over a time scale of tens of ms [*Pasko et al.*, 1996b] and filling part of the field-of-view of photometer 11 (Figure 4-4a), consistent with past observations [*Fukunishi et al.*, 1996b].

Although intense, the initial pulse observed in the top row of photometers lasting for <1 ms is only visible in the video image as a diffuse glow due to the 33 ms integration time of the video camera. Simultaneous observation of the temporal signatures in all nine photometers resolves the rapid lateral expansion as shown in Figure 4-6.

The left column shows the first 0.6 ms of optical signals following the sferic onset ($t = 0$) for the event shown in Figures 4-4 and 4-5. The top-row photometers P1−P9, all pointed at 6.4° elevation, share time and luminosity scales in Figure 4-6, while the less bright but longer-lived signal from P11 is plotted with separate scaling. The increasing delay of the flash onset with pixel distance from the center, ranging from ∼150 μs for pixel 5 to ∼220 μs for P1 and P9, is clearly apparent. The peak intensities of the pulses generally decrease with lateral distance from the center. At a distance of 670 km, the fields-of-view are ∼25 km across for the top row of photometers. The luminosity lasts longer as observed by P11 due to its larger field-of-view, which includes the distant half ("back") of the expanding ring (Figure 4-1).

A second event exhibiting similar lateral expansion is shown in the same format in the center column of Figure 4-6. This event was associated with a 120 kA +CG lightning discharge occurring at 666 km distance from Yucca Ridge at 07:10:14.100 UT on the same day.

The luminosity scales in Figure 4-6 range from 0 to the MegaRayleigh (MR) value inset in each column for P1−P9 and, separately, for P11. These values represent photon intensities assuming the incident radiation is at 700 nm, as described in Section 3.3. Based on the predicted spectral distribution [*Taranenko et al.*, 1993b] of lightning-EMP-produced optical emissions, and on the wavelength-dependence of atmospheric Rayleigh-scattering, and on the spectral response of the photomultiplier tubes (which peaks at ∼350 nm), the signal is expected to come primarily (95%) from the short-wavelength portion of (N_2(1P)). The peak intensities for P4, and in the first event for P11, are uncertain due to saturation of the photomultipliers.

The features exhibited in Figures 4-5 and 4-6 are consistent with those expected to be produced by the electrodynamic interaction with the lower ionosphere of lightning EMP (Section 2.5). To illustrate, we calculate the light output in the N_2(1P) and N_2(2P) bands as would be measured by

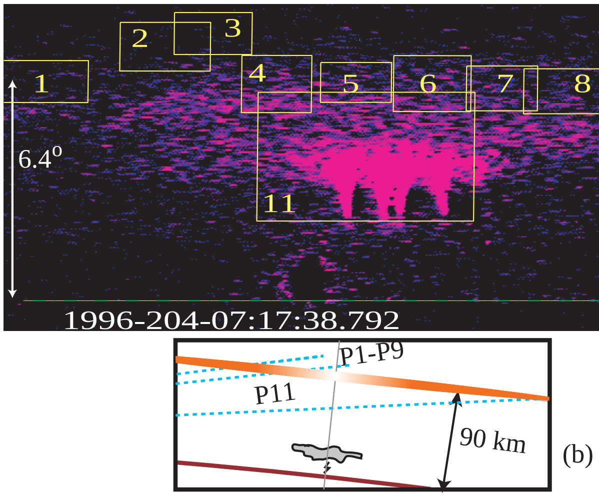

Figure 4-4: Video image showing a sprite and elve. (a) The video camera and approximate photometer array views of the sky during the 07:17:38 UT event on 22 July 1996. The cluster of sprites with columnar structure is at the center. The single video field (33 ms long, ending at 07:17:38.792 UT) has been enhanced (by subtracting a previous field and by thresholding its intensity) to highlight the diffuse emissions constituting the elves. The dashed line indicates the horizon. (b) The observation geometry for the two cases reported here. The dashed lines show the viewing altitudes of P1 through P9 and P11.

the Fly's Eye photometers pointed at 6.4° elevation and their individual azimuths, for a source CG lightning discharge at 669 km range. These theoretical predictions, shown in the righthand column of Figure 4-6 (plotted with the same time scale as the data and with $t = 0$ corresponding to the time of arrival of the sferic at Yucca Ridge) are in good agreement with the observations. The observed onset delay, the speed of lateral expansion, the general form of the apparent vertical development as manifested in P11, and the broadening of pulse widths and reduction of peak intensities at wider angles are all represented in the model predictions. For the model calculations, the intensity of the lightning flash was taken to correspond to a peak electric field intensity at 100 km horizontal distance of 44 V-m^{-1}, empirically consistent with an NLDN-estimated peak current of 150 kA [*Inan et al.*, 1996d]. The width and shape of the shortest (P5) modeled pulse reflects the current waveform of the modeled lightning. The actual durations of the causative lightning flashes for the observed events were not independently measured, and were thus not entered in the model. The spectral distribution of the N_2(1P) and N_2(2P) bands, and the wavelength-dependent Rayleigh-scattering and photometer response, were taken into account to predict voltage levels in the photomultipliers. These were in turn expressed in Rayleighs assuming a 700 nm source for direct comparison with the observations in Figure 4-6.

The calculated response of P11 shown in the solid line is for an elevation angle of 3.1°, which is ~1.1° lower than the actual recorded elevation of this pixel. At the recorded elevation, the computed response is very similar except for an additional initial peak (shown as a dashed line), due to the front part of the elve (see Figure 4-1). The fact that such an initial peak is not observed in the 07:10:14 UT event data can well be explained by a small difference in the lower altitude limit of the luminosity, or by the refractive bending of the light rays travelling nearly tangential to the surface. Indeed, a slightly higher altitude for the latter event is suggested by independent estimates based on timing and geometry; these place the two light sources at 90±5 km and 92±5, respectively. As

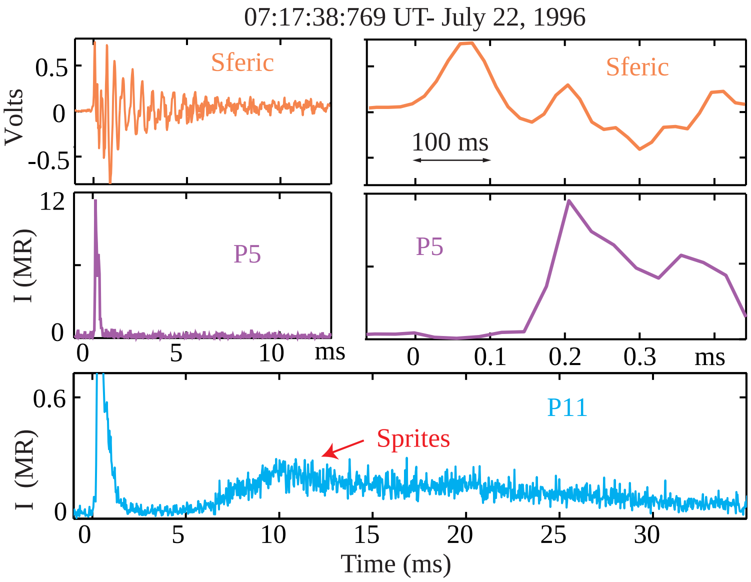

Figure 4-5: Temporal resolution of sprites and elves. The relative timing of the VLF sferic (top row), intensity in P5 (middle row) and that in P11 (bottom row). The expanded sferic and P5 responses (right hand panels) clearly show the delay between the onsets. P11 detects both the fast event (i.e., elves) and the longer and dimmer sprites starting several milliseconds later.

for atmospheric refraction, the bending in an ideal dry atmosphere can be ∼0.3° for the elevation angle of P11 and can greatly exceed this value for a disturbed atmosphere [*Landolt and Hellwege*, 1987, p. 229].

The close agreement between theory and experiment as illustrated in Figure 4-6 supports the predicted structure of elves as consisting of a rapidly expanding ring of luminosity in a narrow altitude range (∼85-95 km). Both the high intensities ($>$ 1 MR) of the optical signals received by the top-row Fly's Eye photometers and the fact that the luminosity is seen in the top-row photometers before P11 indicate that the observed signals are not due to Rayleigh-scattering of light produced by the parent lightning flash.

The 154±30 and 164±30 μs delays respectively for the two events (07:17:38 and 07:10:14 UT) shown in Figure 4-6 between the onsets of the VLF sferic and the first optical pulse (P5) are in close accord with the calculated ∼150 μs delay.

Although the fields-of-view of the Fly's Eye photometers do not extend beyond a full range of ∼234 km (i.e., 117 km radius), the theoretical model (using a broader simulation region than used by *Inan et al.* [1996c]) indicates that, for the 44 V-m^{-1} electric field intensity used here, the lateral extent of the luminous region (defined as the region in which the emission rate exceeds 1% of its peak value) is ∼600 km. The extension of luminosity over such a large region is consistent with the video observations from the Space Shuttle of lightning-associated airglow enhancements (see Figure 2-3 on page 19) with lateral extent ∼ 500 km [*Boeck et al.*, 1992].

4.1.3 Discrimination of elves from Rayleigh-scattered lightning

The submillisecond development of elves in the Fly's Eye's horizontally-spaced photometers, described above, provides an unambiguous signature for the identification of laterally expanding

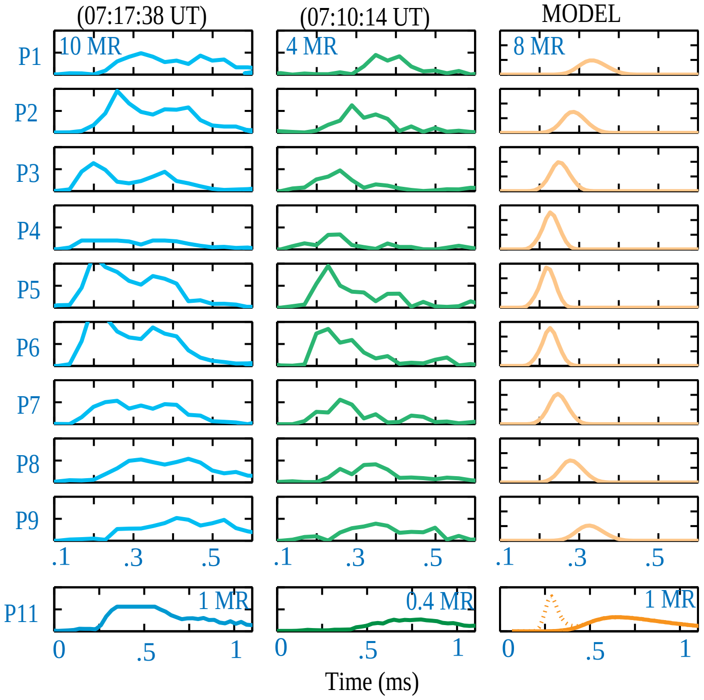

Figure 4-6: Predicted and observed photometric signatures of elves. The two left columns show photometer recordings from two events on 22 July 1996. The responses recorded in the nine top-row photometers as well as P11 are shown. The vertical axes range from 0 to the inset values (in MR) in each column; P1−P9 share a common intensity scale. The time axes for P1−P9 are also identical and show ms after the onset of the associated VLF sferic. The time axes for P11 are compressed (×2) to show the later part of the pulse. The righthand column shows the predicted photometer responses using a two dimensional lightning EMP-ionosphere interaction model [*Inan et al.*, 1996c].

(EMP-caused) flashes, and is used in this dissertation as a means to differentiate elves from the light which originates in the parent lightning. Light from a cloud-to-ground lightning return stroke can be Rayleigh-scattered in the lower atmosphere, but was shown with a Rayleigh-scattering model in Section 3.2.1 to produce neither an onset delay nor a horizontal dispersion greater than ~20 μs.

Figure 4-7 shows examples of the signatures of elves and Rayleigh-scattered lightning recorded with the Fly's Eye. For the case of elves, the VLF/optical path lengths involved in photometric measurements at different azimuths result in a horizontal dispersion among the signal onsets in the photometers. In contrast, Rayleigh-scattered light from lightning appears in the Fly's Eye photometers with an onset that is simultaneous (to within one sample, ~16 μs) amongst the different photometers, and with no more than one sample delay with respect to the associated sferic.

In addition, Rayleigh-scattered light from the continuum emissions of lightning produces emissions in the blue almost as strong as those in the red (being governed only by atmospheric extinction). Not all strong lightning strokes produced a bright 'sky flash,' presumably due to the variability in cloud geometry. Because sky flashes last 500 to 1000 μs, they can obscure any elves that are also present.

All events identified as 'elves' herein exhibit (1) an appropriate onset delay following the parent

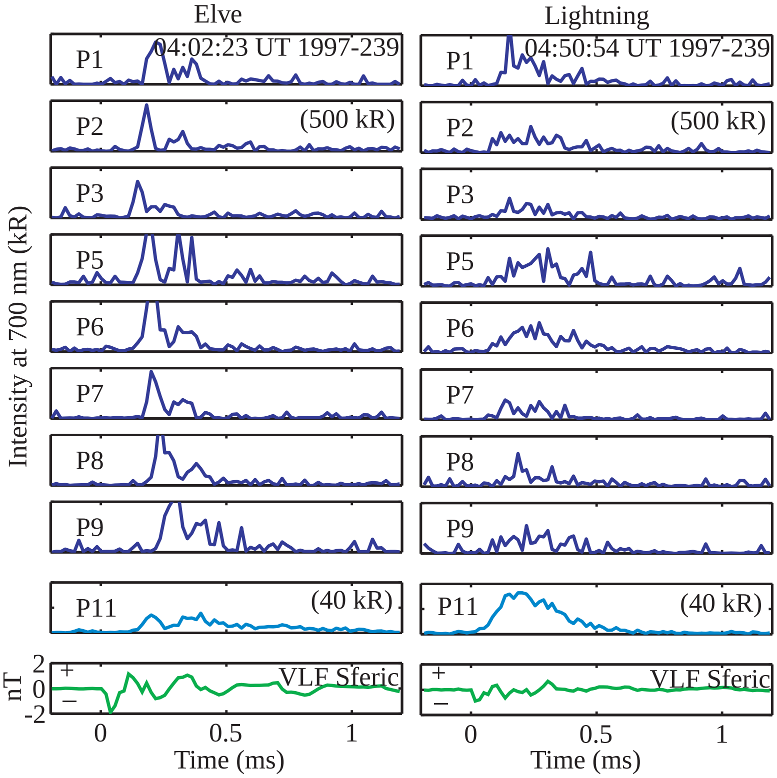

Figure 4-7: Photometric distinction between elves and lightning. Distinctive signatures of elves (with onset delay and dispersion) and scattered light (with neither) as seen in the Fly's Eye. The relative fields-of-view of the narrow (P1-P9) and broad (P11) photometers are shown in Figure 4-4.

lightning sferic (~120 to 160 μs is typical for elves 600 to 800 km away) recorded by the same data acquisition system, (2) fast lateral expansion [*Inan et al.*, 1997], and (3) when recorded, much brighter red emissions than blue. These criteria are used to analyze elves recorded during August 1997 and described in Section 4.2.

4.1.4 Video signatures of elves

It should be noted that in especially rare (i.e., bright) cases elves are detectable in a 17 ms video field. In Figure 4-4a, after significant image enhancement, the broad luminosity due to an elve is visible. Figure 4-8 shows the video record of an even brighter event as seen from the ground. This event was due to an unusually impulsive negative cloud-to-ground stroke. Note the large ($\geqslant$250 km) spatial extent of the luminosity. Without the accompanying photometry, however, one could not unambiguously determine whether this was an elve or scattered light from lightning. Figure 4-9 shows another example of an elve bright enough to register in a video field.

As shown in Figure 4-3 on page 56, the optical signature of an elve caused by the EMP from a strictly vertical lightning current is expected to exhibit a central "hole" corresponding to the minimum in the radiation pattern of a vertical dipole. Such a central dimmed region may be perceptible in Figure 4-8, but it is ambiguous, given the existence of intervening cloud bands. In the

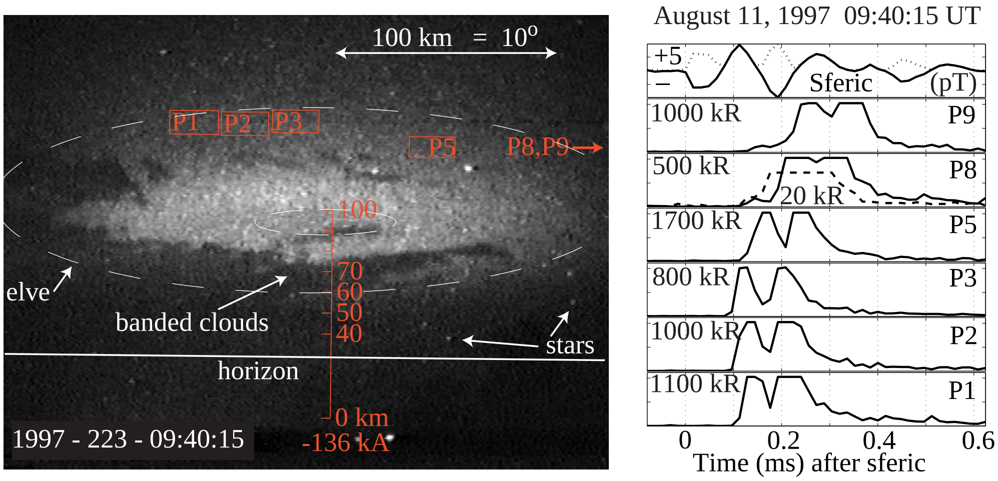

Figure 4-8: Detection of blue emissions in an exceptionally bright elve. A 17 ms field from image-intensified video shows a broad flash, deduced to be an elve from the accompanying photometry. The photometers each saturated, but show the signature of an elve. The image shows altitudes overlying a strong −CG discharge reported by NLDN. P8 and P9 were pointed just to the right of the image. Dashed lines show the approximate extent of the elve and its central minimum. Some dark bands (foreground clouds) obscure part of the elve. The unusually short onset delay for an event 571 km away is indicative of the low vertical extent of this intense flash. The dotted curve is the absolute value of the sferic, showing variations in optical output and causative EMP with similar time scales. The dashed curve accompanying that from P8 shows the signal recorded by P2, a blue photometer which saturated at 20 kR.

extraordinary case shown in Figure 4-9 the shape of the elve as well as the central hole is remarkably evident.

The vertical scale in Figure 4-8, as well as in subsequent video images for which the NLDN located an associated cloud-to-ground stroke, shows the azimuth of the parent lightning and indicates altitudes directly overlying it (see Section 3.5.3). Because the images are taken from the ground and are not in limb view, these altitudes do not necessarily correspond to the altitude of any horizontally-extended luminosity in the image. For a horizontal range uncertainty of ∼50 km, the corresponding uncertainty in the altitude scales is approximately 10 km.

4.2 Correlation with positive and negative lightning strokes

In this and the following two sections, we consider only events in the period 03:00 to 10:00 UT on 27 August 1997, when a large mesoscale convective system was very active 700 to 850 km southwest of the Langmuir Laboratory for Atmospheric Research (107.19° W × 33.98° N × 3200 m) in New Mexico. Instruments deployed at Langmuir included a broadband (300 Hz to 20 kHz) VLF receiver to record sferics, an intensified video system, and the Fly's Eye photometric array. Signals from the sferic receiver and photometers were recorded in data snapshots of ∼2 seconds duration by a pre-trigger buffering system (Section 3.4, with timing synchronized to within 16 μs of GPS time through a parallel New Mexico Tech data stream.

On this night the triggering was done manually, based on observations with the bore-sighted intensified video system. Due to the much longer (∼5 to 150 ms) duration of sprites as compared

Figure 4-9: Bright elve viewed from an aircraft. An image of an elve over Europe captured by M.J. Taylor and L.C. Gardner of the Space Dynamics Lab., Utah State University, during the 18 November 1999 Leonids meteor storm at 02:10:00 UT. The luminosity is similar in scale to that shown in Figure 2-3. From `http://leonid.arc.nasa.gov/leonidnews.html`

with elves (<1 ms), sprites are better suited for detection at a video frame rate than are elves, and many elves are not detectable above the night sky background with our video imaging system. Consequently our manual triggering method was biased towards events associated with sprites, and thus towards large positive cloud-to-ground lightning discharges [*Boccippio et al.*, 1995]. On the other hand, manual triggering was not exclusively selective of events with sprites, since occasionally bright Rayleigh-scattered light from the parent flash and brighter than usual elves were also evident in video. Photometric signatures of sprites were never confused with the onset of elves, in part because sprites begin at least ∼500 to 2000 μs after any closely associated sferic.

The identification of elves in this study does not rely either on recordings from the 30 frame-per-second video which was bore-sighted with the photometer array, nor on the microsecond timing provided by the NLDN. During the period 03:00 to 10:00 UT on August 27, at least 39 flashes were identified as elves, based on the criteria described above on page 59 (Section 4.1.3). Figure 4-10 shows a histogram of these events sorted by the peak-to-peak intensity of their associated sferics. While most of the +CG events in Figure 4-10 were associated with sprites, it is remarkable that a considerable fraction (31%) of the events were associated with −CG flashes, in spite of the fact that the manual triggering method used on this day was highly biased towards sprite-associated discharges and towards the very brightest of elves.

The fact that −CG flashes also produce elves is consistent with our theoretical understanding of collisional heating by the lightning electromagnetic pulse, a process which is independent of the polarity of the field. During the period 03:00 to 10:00 UT, 90% of the CG flashes recorded by NLDN from the Mexican MCS and with peak current greater than 25 kA were −CG. Based on the occurrence rate of highly energetic −CG and +CG discharges the above result indicates that EMP-induced heating and ionization of the lower ionosphere (as manifested by elves) above nighttime thunderstorm systems may well be much more prevalent than sprites.

To further assess the prevalence of elves, we surveyed all the NLDN flashes with peak current over 38 kA that were within the Fly's Eye field-of-view and which occurred during one of the 261 recorded data samples, each lasting about 2 seconds. Of the 86 NLDN events in this set, the photometric records for 13 events were dominated by the Rayleigh-scattered light due to the parent lightning

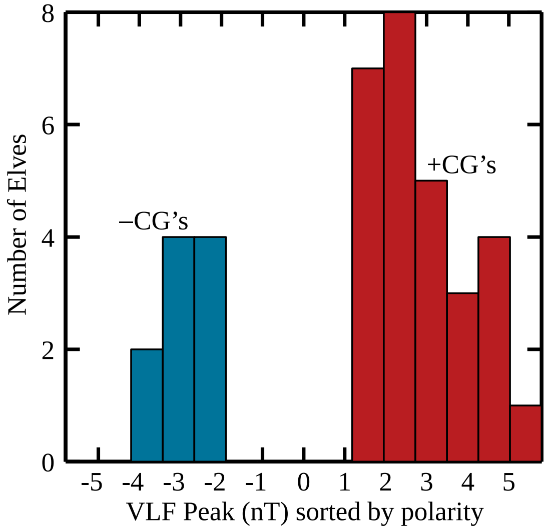

Figure 4-10: Correlation between elves and lightning polarity. Histogram of elves detected versus the strength of their causative VLF sferic, sorted by CG polarity.

flash. Of the remaining 73 flashes, 52% (38) exhibited the telltale signature of elves. Above 45 kA in the NLDN record, this fraction was 73% (37); above 57 kA, all (34) of the flashes had accompanying elves.

These statistics are necessarily affected by our manual triggering method. Nevertheless, Figure 4-11 shows a good correlation between the peak VLF fields produced by lightning and the maximum optical intensity seen by any of the Fly's Eye photometers, even though the photometers were not necessarily looking at the same part of the flash in different events. The scale on the top of Figure 4-11 shows NLDN peak current values based on a linear fit to the good correlation between VLF peak and NLDN peak which was found for all but a few outliers among these events. This fit is shown in Figure 4-12. The model of Section 2.4 was run for cloud-to-ground lightning 10 km high and reaching its peak current in 30 μs. The maximum $N_2(1P)$ optical intensity as would be seen from the ground at 745 km distance for a range of peak current values was calculated and is plotted as a dotted line in Figure 4-11. The shape of this curve agrees well with previous calculations which did not take into account the viewing geometry [*Taranenko et al.*, 1993b]. A threshold in the VLF peak is evident; this results from a combination of the instrument background signal level and the highly nonlinear dependence of $N_2(1P)$ optical output on the instantaneous field strength.

All elves events as identified by the Fly's Eye have been found in direct association with the sferic signature of a cloud-to-ground, rather than intracloud, discharge. Furthermore, the timing always indicates that the elve is caused by the CG rather than by any associated sprite (as suggested by *Taranenko et al.* [1997] and *Roussel-Dupre et al.* [1998]).

4.3 Determination of flash location using high-resolution timing

The time-resolved optical features of elves as measured in the Fly's Eye not only discriminate elves from other flashes, but also provide quantitative information regarding the location of each elve

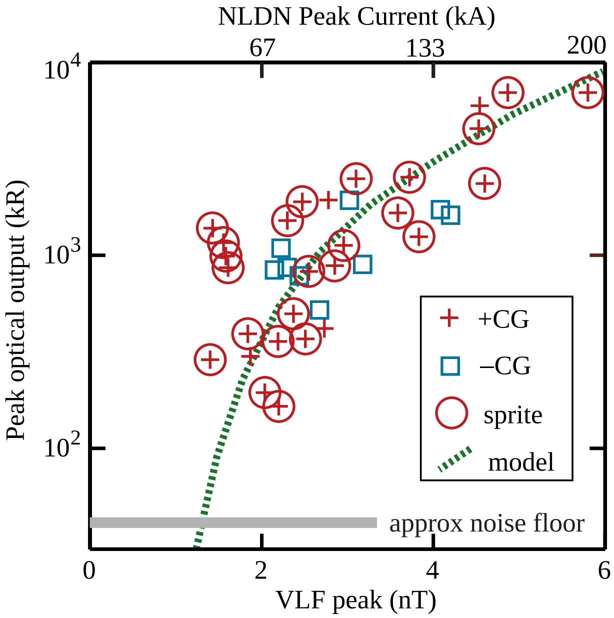

Figure 4-11: Theoretical and observed correlation between peak brightness and causative lightning intensity. Squares and crosses show −CG and +CG events, respectively. A circle indicates that sprites were associated (within 100 ms) with the event. The dotted line shows the theoretical calculated $N_2(1P)$ emissions multiplied by 0.075 to account for atmospheric and filter transmittance and incomplete coverage by the photometers.

with respect to its causative CG lightning stroke. The field-of-view of each Fly's Eye photometer was measured precisely (Figure 3-11 on page 49), and the pointing elevation and azimuth at any time during observations were recorded by an electronic clinometer and a compass-adjusted, graduated mount. This knowledge, coupled with the lightning locations given by the NLDN and the delay in each photometer between the sferic and the flash onset, constrain in three dimensions the source of the first light seen in each photometer [*Inan et al.*, 1997].

Figure 4-1 shows how this is possible for the case of a photometer pointed directly over the causative CG. The VLF radio pulse from the CG return stroke constitutes a ground wave propagating at very nearly the speed of light (c). It reaches points on the surface of the Earth a time $t{=}s/c$ after the return stroke occurs; here, s is the great circle path length from the lightning location.

The onset of an optical flash in a photometer which is colocated with the VLF receiver is due to a VLF pulse propagating to an ionospheric point, and the resulting optical wavelengths propagating from that point to the photometer, both at the speed of light. The segment length l between a point near the ground (observer or lightning) and one in the ionosphere for a spherical Earth is

$$l = (R_\mathrm{E} + h)\frac{\sin\left(\dfrac{s}{R_\mathrm{E}}\right)}{\cos\left(\theta + \dfrac{s}{R_\mathrm{E}}\right)}$$

where R_E is the Earth radius, h is the observer's altitude, and θ is the observer's viewing elevation angle above horizontal. Because the source of the photon production is constrained to be along the

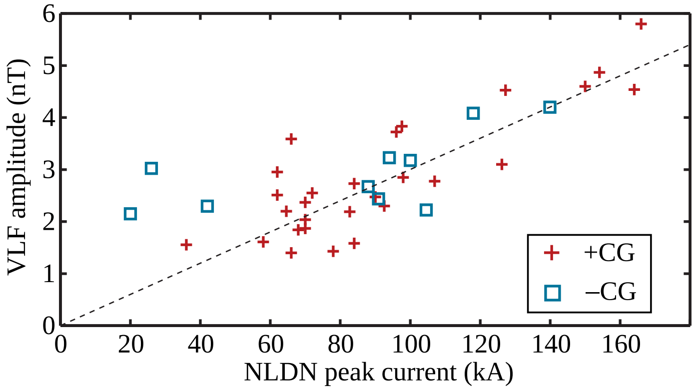

Figure 4-12: Correlation between VLF intensity and NLDN reported peak current. VLF sferic peak-to-peak intensity (measured in equivalent wave magnetic field) is shown versus NLDN peak current for the same elves events shown in Figure 4-11.

line of sight of the observer, the time difference between arrival of the sferic and an optical pulse in a photometer constrains the optical source location.

The onset delays in each photometer for all the events ranged from 97 μs to 620 μs, where the longer times correspond to parts of the elves located behind the source lightning or far to the side of it. However, the first appearance of each event in any photometer occurred almost exclusively between 100 μs and 200 μs after reception of the associated sferic.

Figure 4-13 shows a top-down view of source locations determined in this way for a bright flash. The uncertainty due to the extent of the fields-of-view is shown by the dotted quadrilaterals. We performed this analysis for all identified elves associated with an NLDN flash, and in a majority of cases, flashes were localized at a distance of over 100 to 200 km from the source lightning. In several cases this distance was well over 300 km, as predicted for strong discharges [*Inan et al.*, 1997].

While both the altitude and the geographic location of the initial observed point of each flash are determined in this way, the altitude is not as tightly constrained for very low elevation angles (about 4° on the 27th of August). Nevertheless, the deduced lower altitudes of each flash source remained roughly consistent with the predicted 85-95 km [*Inan et al.*, 1996c] and served as a sanity check for the discrimination of elves from Rayleigh-scattered light, which, due to its short onset delay, would have a deduced altitude near zero (see page 38).

4.4 Distribution of elves throughout large storm systems

Elves are optical signatures of strong energetic coupling of lightning EMP to a narrow altitude range in the D region of the ionosphere. Detecting elves in association with negative lightning discharges implies the ubiquity of this phenomenon, since negative CG discharges are known to be much more common than positive discharges [e.g., *Orville*, 1994]. Indeed, our results indicate that nearly all discharges with EMP intensity above a certain threshold may trigger elves. Our results further indicate that the spatial extent of the ionospheric disturbance from a single discharge is as large as anticipated in Figure 2-5. While the optical emissions in elves are expected to be strongly dependent on the strength of the causative discharge, transient electron heating should occur for smaller discharges which may not produce detectable optical output.

Moreover, the possibility of the superposition of electron density changes due to successive CG

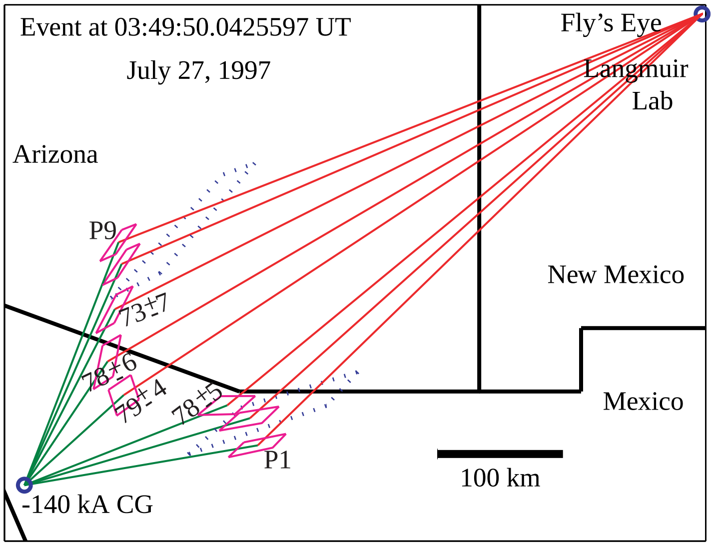

Figure 4-13: Location of luminosity in elves. Quadrangles show the deduced source locations of the first elves luminosity in each photometer. Constrained lower altitudes are also shown for some photometers.

strokes described by *Taranenko et al.* [1993a] and in Section 2.5.3 seems cogent given the large area (~3 × 10^5 km^2) shown here to be affected by a single EMP. Ionization changes decay over time scales on the order of 10 to 100 s in the *D* region (see Section 1.3), so that the accumulated effect of successive strong cloud-to-ground strokes occurring at different points in a large storm system may profoundly affect the nighttime *D* region. As an example, within a 770 km length of the Mexican mesoscale convective system of August 27, NLDN recorded 310 CGs with peak current greater than 45 kA during the period 03:00 to 10:00 UT (an average of one per 80 s), with much more intense local clustering during some periods.

4.5 Two-color photometry

The small total optical output of elves makes spectroscopic studies at high time resolution exceedingly difficult, as mentioned in Section 3.3. For instance, an N_2(1P) surface brightness between 650 and 750 nm wavelength of 1 MR lasting 0.1 ms, or an integrated energy of ~2 pJ/cm^2/str, amounts to 10^1 to 10^4 photons for each spectral peak shown in Figure 3-6 on page 42 for an aperture similar to those of the Fly's Eye but for a field-of-view encompassing the entire elve. For a narrow slit field-of-view, the counts are much fewer.

Instead of resolving the details of the shape of the emission spectrum, two-color photometric observations have been made (see Section 3.3.3). For instance, the ratio between emissions from the first positive and second positive bands of N_2 is much higher for elves (and sprites) than for the broadband emissions of lightning. Such spectral ratios have been used [*Armstrong et al.*, 1998a; *Barrington-Leigh and Inan*, 1999; *Uchida et al.*, 1999; *Armstrong et al.*, 2000] as another criterion for discriminating between elves and scattered light from lightning.

Figure 4-8 shows the sferic and photometric signals recorded for an elve event at 09:40:15 UT on 11 August 1997. The NLDN simultaneously recorded a negative CG discharge with current 155 kA, located 571 km away at a bearing of 82° east of geographic north. The central pixel (P5) of the

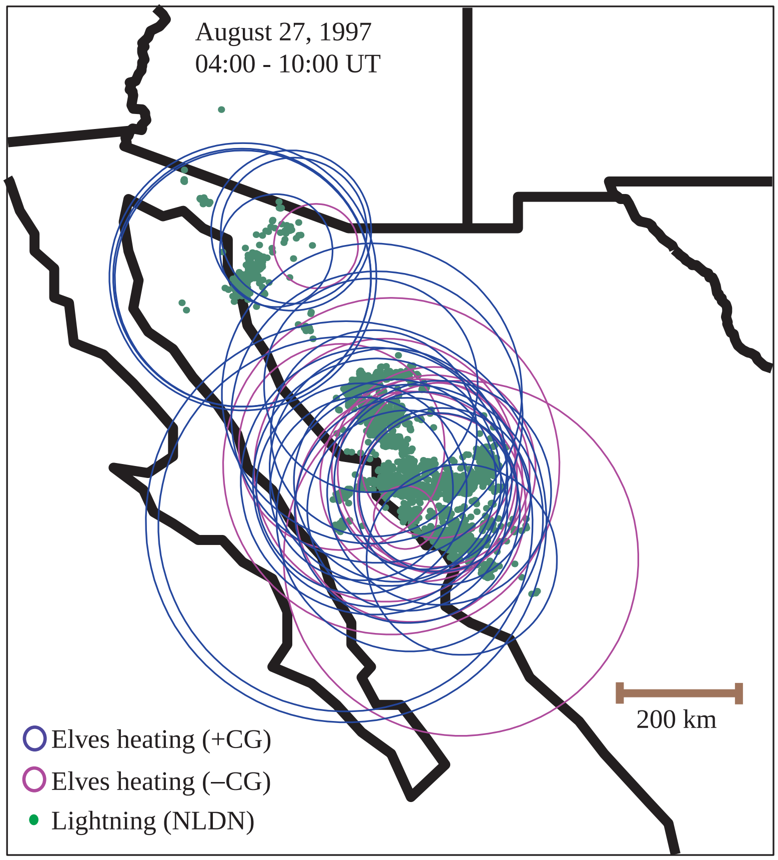

Figure 4-14: Horizontal extents of optical emissions in 38 elves from one mesoscale convective system observed over northwestern Mexico.

Fly's Eye was pointed at a bearing of 86° and an elevation of 11°. The polarity of the CG lightning is unambiguously confirmed by that of the received sferic.

This event exhibits an interesting double-pulse structure and is unusually bright, showing strong emission outside the N_2(1P) band. The dotted trace in the top panel of Figure 4-8 shows the absolute magnitude of the greater than 1 kHz component of the sferic, to emphasize that the optical pulses occur on the same time scale as the amplitude variations in the sferic. This result suggests that the fine structure of the EMP electric field waveform may be manifested in the optical emission signature.

The dashed trace shown in Figure 4-8 is the response of P12, a blue photometer with a rectangular field-of-view containing that of P8, but approximately 3 times as large in each dimension. A second blue photometer, P10, had a similar relationship to the red photometer P2. Only a handful of events during the study period were bright enough to be detected by our blue photometers and, as shown below, the data are inadequate for determination of *in situ* parameters. Because this was a significant experimental shortcoming, some relevant details of the spectral band comparison are included below.

In order to make a comparison between optical signal levels seen in the bandpasses of the blue and red filters, we consider the spectral bands N_2(1P) and N_2(2P). The dashed line in Figure 4-15

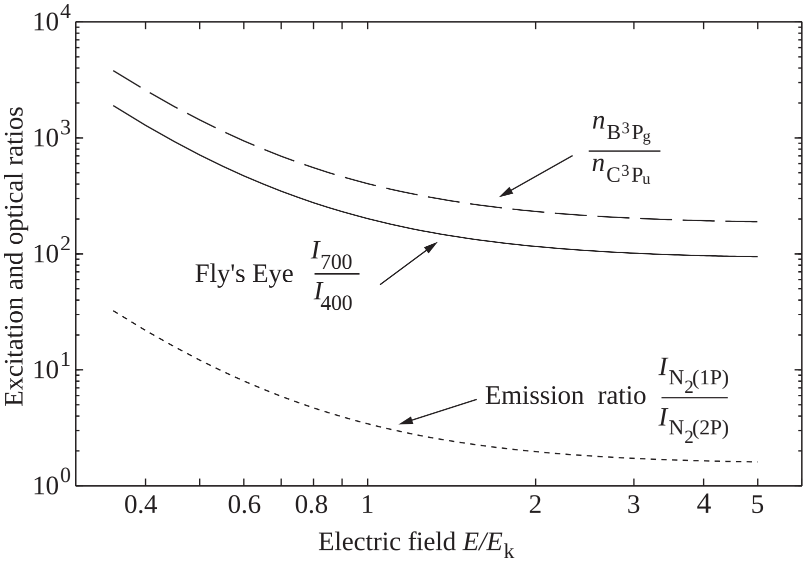

Figure 4-15: Predicted optical ratio of blue to red photometer signals as a function of electric field. Optical transmission was calculated for a viewing elevation of 3.5°

shows the state excitation ratio $n_{\mathrm{B}^3\Pi_\mathrm{g}}/n_{\mathrm{C}^3\Pi_\mathrm{u}}$ predicted by equation (2.18) for different electric fields, with the effects of quenching neglected. The dotted line shows the ratio of emissions $I_k = A_k n_k$ from these states. The solid line shows the ratio of predicted signal intensities in the red and blue photometers of the Fly's Eye for a viewing elevation of 3.5°. This ratio results from performing the integrations in equation (3.8), and takes into account the shape of the spectra, the filter transmittances, the photocathode response, and the atmospheric transmission. The considerable variation of the observed ratio of the intensities in the two bands over the electric field values shown indicates that the Fly's Eye's two-colored photometry is a promising tool for remotely probing the electric field that is the ultimate cause of the optical emissions.

Unfortunately, the observed ratio of the intensities in the two bands also varies strongly as a function of viewing elevation. Figure 4-16 shows the relationship between photometer signal intensity and the source band brightness for different viewing elevations typical for measurements of elves. Here the varying atmospheric attenuation as experienced from the altitude of Langmuir Laboratory is calculated using the MODTRAN3 model described in Section 3.2.2. The solid line gives the ratio between the dashed and dotted lines and represents the transformation between the red to blue signal ratio in the Fly's Eye and the deduced source emission ratio. It varies by an order of magnitude over 3° of elevation, equivalent to the elevation span in the fields-of-view of P10 and P12.

At low viewing elevations the attenuation of blue light becomes extreme and is also highly dependent on atmospheric conditions and aerosol content. As a result, refraction effects may also play a large role. Several bright elve events from 27 August 1998 produced a measureable signal in one or both blue photometers and are listed below. The intensities shown in Table 4.1 are averaged over the respective fields-of-view, which are ∼9 times larger in the case of the blue photometers, and the elevations correspond to the center of the fields-of-view. The lightning events occurred at ranges of approximately 650 km to 750 km. The deduced band emission ratio varies primarily in accordance with the viewing elevation angle, suggesting that the fields-of-view are too large in elevation or that

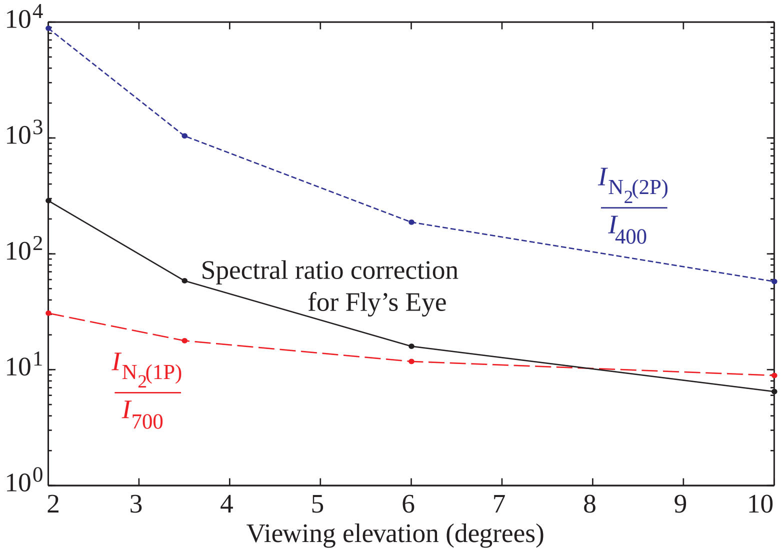

Figure 4-16: Sensitivity of the Fly's Eye to N_2(1P) **and** N_2(2P) **as a function of viewing elevation angle.**

the atmosphere (aerosol content) was not well described by the MODTRAN calculation.

Table 4.1: Inconclusive spectral ratio data for elves.

Event (UT)	Photometers	Red	Blue	Elevation	Emission ratio $\left(\frac{I_{N_2 1P}}{I_{N_2 2P}}\right)$
03:49:49	P2/P10	1190 kR	1.3 kR	6.8°	68.8
03:49:49	P8/P12	1175 kR	1.1 kR	5.8°	62.1
06:24:36	P8/P12	996 kR	1.2 kR	2.2°	3.5
06:34:39	P2/P10	292 kR	1.2 kR	3.2°	3.0
08:17:15	P2/P10	2314 kR	2.8 kR	3.6°	14.8
08:17:15	P8/P12	1803 kR	3.3 kR	2.6°	3.6
08:36:25	P2/P10	1622 kR	1.8 kR	3.6°	16.0
08:36:25	P8/P12	1782 kR	2.9 kR	2.6°	4.0
08:41:38	P2/P10	622 kR	1.1 kR	3.6°	10.1
08:41:38	P8/P12	1419 kR	2.0 kR	2.6°	4.5

Chapter 5

Combined Photometry and Imagery of Sprites

Confusion in the interpretation of standard-speed video observations of optical flashes above intense cloud-to-ground lightning discharges has persisted for a number of years. In Section 5.1, much of which has been published by *Barrington-Leigh et al.* [2000], high speed (3000 frames per second) image-intensified video recordings taken in 1997 are used along with theoretical modeling to elucidate the optical signatures of elves and sprites in video and in photometric arrays. In particular, the brief diffuse flash sometimes observed to accompany or precede more structured sprites in standard-rate video is shown to be a natural component of sprite electrical breakdown and to be due entirely to the quasi-electrostatic thundercloud field (sprites), rather than the lightning electromagnetic pulse (elves). This portion of a sprite has been named the "sprite halo" [*Barrington-Leigh et al.*, 2000].

Section 5.2 relates the observation of sprites in close association with negative cloud-to-ground lightning ($-$CG) on at least two occasions above an unusual storm on 29 August 1998, as reported by *Barrington-Leigh et al.* [1999a]. Data from high speed photometry, low-light-level video, and receivers of lightning electromagnetic signatures in the frequency range 10 Hz to 20 kHz are used to establish the association and indicate that the causative $-$CG discharges effected unusually large vertical charge moment changes ($\Delta \mathrm{M_{Qv}}$) of up to 1550 C-km in 5 ms. The existence of sprites caused by $-$CGs, rather than the regularly associated +CGs, has implications for sprite models and for strategic choices made while undertaking sprite observations.

Section 5.3 discusses different time scales evident in photometric measurements of sprites. Observed features imply the existence of electric fields that are kept constant over times ranging from ~1 ms to tens of milliseconds. In addition, they may provide a means to remotely sense the electric field within sprites.

5.1 Sprite halos

Classification of high-altitude optical flashes caused by tropospheric lightning as "sprites" and "elves" has been guided as much by theorized physical causes as it has by distinct sets of observed phenomena. The electric field which causes heating, ionization, and optical emissions in sprites is caused by the charge moment changes (e.g., 250 to 3250 C-km according to *Cummer and Inan* [1997]) associated with the movement of large thundercloud charges, usually in association with intense positive cloud-to-ground lightning. On the other hand, the electric field causing heating, ionization, and optical emissions in elves is that of an electromagnetic wave which is launched by, and occurs in proportion to, changing current moments associated with very impulsive (>60 kA) return stroke currents [e.g., *Barrington-Leigh and Inan*, 1999]. As a result, elves last no longer than ~1 ms, while the durations of sprites vary greatly, ranging from a few to many tens of milliseconds.

Due to their fleeting (<1 ms) existence, elves have been somewhat harder to study optically than have sprites, whose lifetime is more on par with the exposure time of standard video fields (~17 ms). As described in Chapter 4, a high speed photometric array lends itself well to the identification of elves. In recent years ostensible elves have also routinely been identified by others based on the existence of diffuse glows, often preceding or accompanying more filamentary "sprites," in intensified video recordings. While *Barrington-Leigh and Inan* [1999] did not claim to identify any elves without the photometric evidence described in Section 4.1, these diffuse glows seem generally to occur when the photometric signature of elves also exists.

For instance, Figure 5-1 shows a (dim) diffuse optical emission which was associated with a negative cloud-to-ground lightning return stroke and with the photometric signature of elves, but without any subsequent streamer-type sprites. These optical flashes are very rarely observed on more than one successive video field, indicating that the luminosity persists for much less than 17 ms.

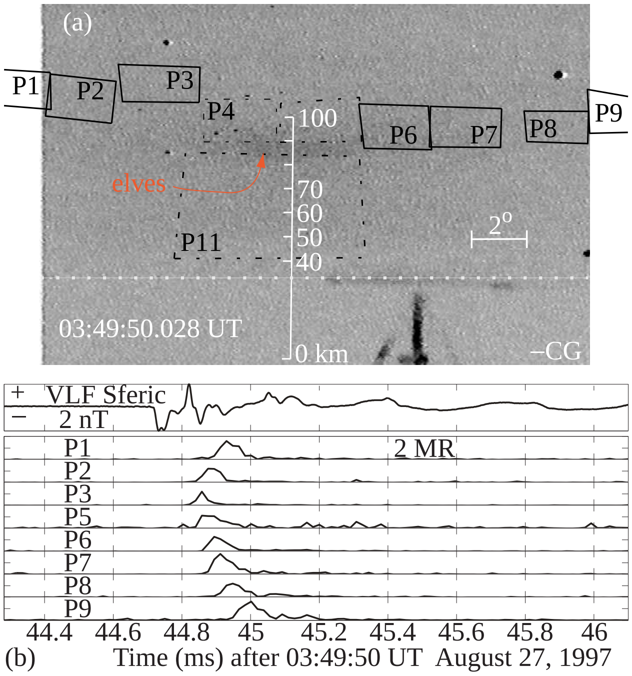

Figure 5-1: Misinterpreted diffuse glow in video observations. (a) Figure from *Barrington-Leigh and Inan* [1999], showing what was at the time thought to be the video signature of a (−CG) elve (shown in inverse video for clarity). In retrospect, and based on the discussion in the present section, this diffuse glow is probably not an elve but instead the "sprite halo" produced entirely by QE heating. (b) The photometric signature of elves, not apparent in the video, was also seen for this event.

However, upon critical inspection, these rather compact (~40 km horizontal extent) flashes do not bear a strong resemblance to the expected form of an elve, which is predicted (Figure 4-3 on page 56) and observed (see Sections 4.1.2 and 4.1.4) to be relatively uniform in brightness over a horizontal scale of >150 km.

Below we demonstrate that the diffuse glows previously misidentified as elves are well described by models of electrical breakdown in sprites due to the thundercloud quasi-electrostatic (QE) field. The recent analysis of the temporal and spatial scales which characterize the electrical breakdown at different altitudes above sprite producing thunderstorms has demonstrated that the upper extremities of sprites are expected to appear as amorphous diffuse glows, while the lower portions exhibit a complex streamer structure [*Pasko et al.*, 1998a]. We refer to the diffuse region of sprite breakdown, especially as observed optically, as a "sprite halo"* and to the lower portion as the streamer region of sprites.

In Figure 5-1 the intensified video shows the signature of a sprite halo while the photometric array shows primarily that of an elve for the same lightning event, reflecting the complementary capabilities of each instrument. The difficulty of recording luminosity due to elves was discussed in Section 4.1.4 on page 60. Elves are largely undetectable using video equipment with a 17 ms or 33 ms temporal resolution.

5.1.1 Modeled optical signatures

A computer simulation of the effects of tropospheric currents on the lower ionosphere was described in Section 2.4 and applied in Section 2.5 to two cases in which the electric field in the upper atmosphere was dominated by either the quasi-static (QE) component or the radiated (EMP) component. In Section 4.1.1 optical signatures as seen from the ground were predicted for the case of elves (EMP). Below, the same electromagnetic model is used in an analogous way to predict ground observations of emissions for the QE case in order to compare with observations and with the EMP results already shown in Figures 4-2 and 4-3.

5.1.2 High speed video observations

Stanley et al. [1999] reported the use of a high-speed triggered image-intensified video system for sprite observations which included recordings of several cases of diffuse flashes preceding streamer formation in sprites. The recordings reported here were acquired at 3000 frames/second on 6 October 1997 from Langmuir Laboratory while observing the atmosphere above a storm ∼875 km to the south. These data provide an opportunity to compare in more detail the appearance of diffuse video flashes with the predictions of a numerical model.

Figure 5-2a shows VLF sferic, wide field-of-view photometer, and high speed video recordings from Langmuir Laboratory for an event at 05:00:04.716 UT on 6 October 1997. The data are time-tagged and co-aligned to <50 μs accuracy. Less than 0.5 ms after the arrival of the sferic, a photometric enhancement corresponds to a diffuse, descending glow in the imagery. Following this by ∼1 ms, a group of sprite columns develops and subsequently brightens in a manner similar to that described by *Cummer and Stanley* [1999].

Figure 5-2b shows the two hypothetical lightning currents used to model emissions resulting predominantly from the EMP and QE fields. While all fields are encompassed within the same fully electromagnetic model, the slow and fast input currents will be referred to as the "QE case" and the "EMP case," respectively. The EMP case has a 30 μs current rise time and thus radiates ∼10 times as intensely as the QE case which has a 300 μs rise time. However, on time scales >0.2 ms the QE case brings about a much larger vertical charge moment change.

The three sequences shown in Figure 5-2c compare observations of the diffuse flash with video signatures predicted by the model, given the lightning currents shown in (b) and the precise video frame timing (with respect to the lightning return stroke) and viewing geometry in effect during the observations. Scales show altitude above the source lightning discharge. The optical signature for the EMP case is that of elves, but the field-of-view shown reveals only a small part of the elve around its center. A wider field-of-view would reveal that the elve extends over hundreds of

---

[*] This name may be an unfortunate one, since the shape of elves seen in diagrams, some models (Figure 4-3), and some images (Figure 4-9) exhibits a central hole and thus resembles a halo more than the diffuse region of sprites.

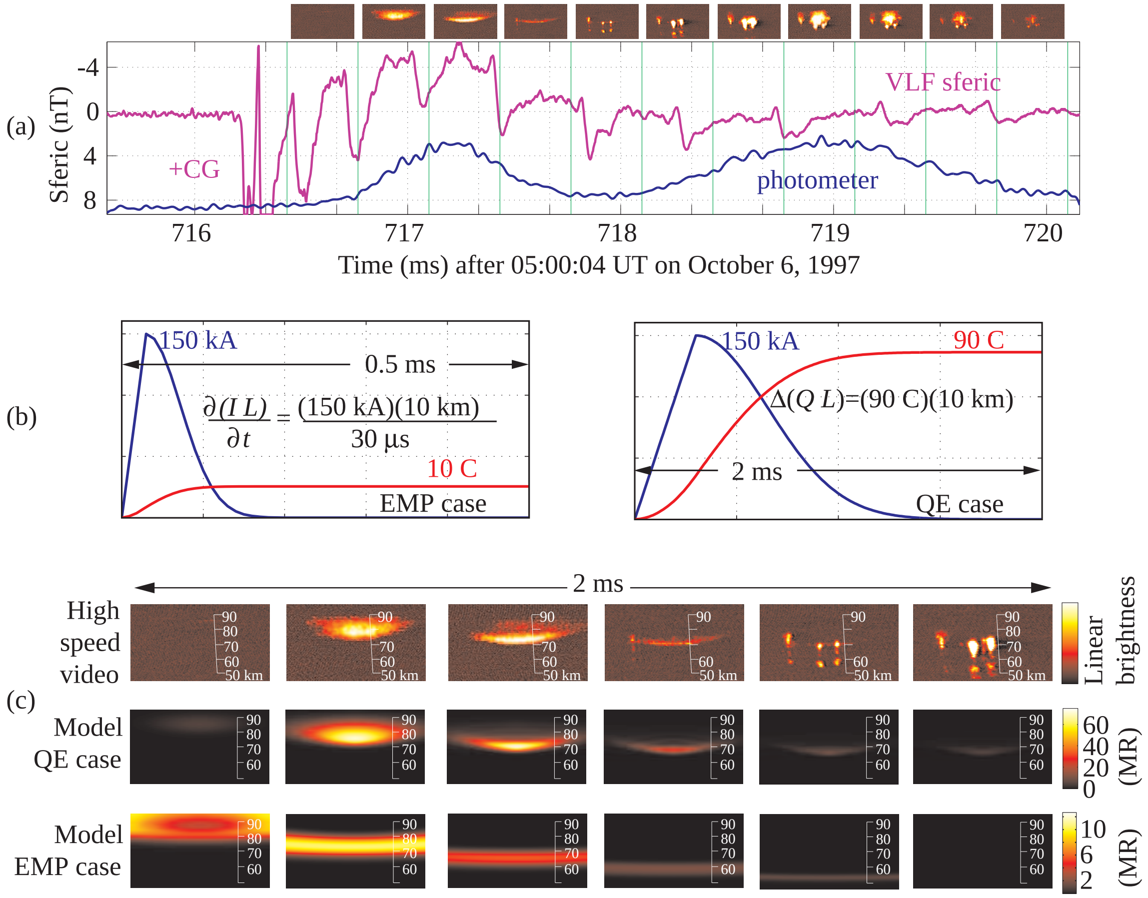

Figure 5-2: Modeled and observed diffuse flash at 05:00:04.716 UT. (a) A time-resolved sprite halo, with VLF sferic and photometer data; (b) theoretical lightning currents used as input to the model; and (c) comparison of observations (false color) and the modeled QE and EMP cases, which show emissions in the N_2(1P)band.

km horizontally and begins before the luminosity recorded in high speed video and well above the recorded field-of-view.

A more realistic lightning current profile may have a fast rise time, like that of our EMP case, but a slow relaxation, like the QE case. For the parameters used in the model, the elve (EMP case) is less than one sixth as bright as the diffuse flash of the QE case. Thus, even if both optical emissions were produced in the observed event, the elve may not have been bright enough to be detected by the high speed imager. Nevertheless, the timing, altitude, shape (including upward curvature), and development of the observed luminosity match closely those of the modeled response to a slow lightning current producing a charge moment change of ~900 C-km in ~1 ms.

By comparison with the model, it can be inferred that this luminosity occurs at altitudes of 70 to 85 km, localized (~70 km wide) over the source currents, and descends in altitude in rough accordance with the local electrical relaxation time $\tau_E = \epsilon_0/\sigma$ [*Pasko et al.*, 1997b]. In contrast, the luminosity in elves is confined to higher (80 to 95 km) altitudes and its time dynamics are dominated by an outward expansion in accordance with the speed of light propagation of the lightning EMP,

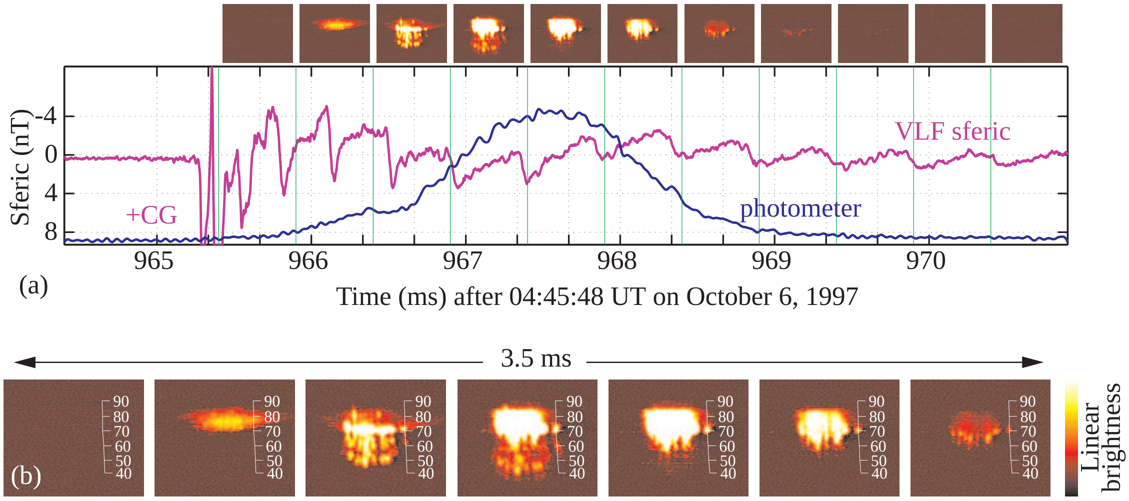

Figure 5-3: Sprite halo following lightning at 04:45:48.962 UT. 6 October 1997

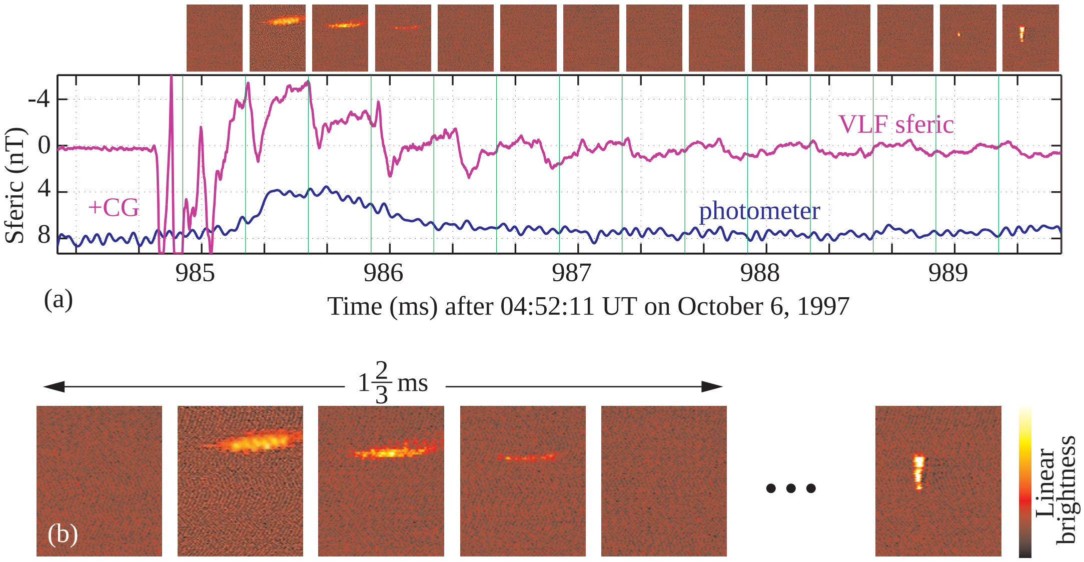

Figure 5-4: Sprite halo following lightning at 04:52:11.981 UT.

as described in Section 2.5.

Modeling also indicates that the upward curvature apparent in the luminosity (Figure 5-2c) after its first appearance is due to the ‘expulsion’ of the electric field by the enhanced ionization. The ionization enhancement for this modeled event was presented in Figure 2-7. While optical luminosity, especially at the higher altitudes (>80 km) of the diffuse upper portion of a sprite, can occur without extra ionization, the upwardly-curved shape of the observed event indicates that significant ionization did occur.

Two other similar events were observed in high-speed video recordings from 6 October 1997 and are shown in Figures 5-3 and 5-4. The three events showed varying delays between the beginning of the sprite halo and the first development of streamer structure. In particular, in the two events not shown in Figure 5-2, the streamers initiated ∼0.3 ms and ∼3.6 ms after the halo onsets, based on the high speed video.

Altogether, 42 sprite clusters were recorded at video frame rates of 1000 to 4000 s^{-1} during observations on October 3, 6, and 7, 1997. Sprite halos were recorded by the high speed video for only four of these events. All four of the lightning events which did produce sprite halos exhibited unusually large vertical charge moment changes during the initial $\leqslant$1 ms of the return stroke, as inferred from ELF filtering of the sferics measured at Langmuir Laboratory.[†] This time scale is fast enough for the electric field to penetrate to lower ionospheric altitudes (see Section 5.1.6).

5.1.3 Sprite halos in normal-rate video

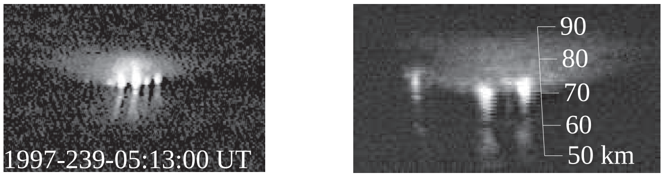

One 17 ms field of normal video.

High speed video frames integrated over 2 ms.

Figure 5-5: Comparison of two sprite halos observed in normal and high speed video.

When averaged over 2 ms, the observed sprite of Figure 5-2 appears as a diffuse halo capping a cluster of columnar features. Figure 5-5 compares this averaged image to a commonly observed form for sprites in normal-speed video, and suggests that broad upper halos occasionally seen in video of sprites are also sprite halos preceding the onset of streamer formation. When the frames of this high speed video sequence are averaged over the entire duration of the sprite (∼4 ms, still much less than a normal video frame) the sprite halo is mostly washed out and becomes hard to perceive. It is thus likely that only in exceptionally bright cases are the diffuse upper portions of sprites visible in a normal video field as sprite halos.

5.1.4 Sprites and elves in photometry

No elves were recorded by the high speed video system in the three mentioned nights of observation in 1997. With much higher temporal resolution than that afforded by even this system, one may be able to resolve in two dimensions the dynamic temporal evolution of an elve, dominated

---

[†] Determination of lightning current moments is not possible for these events because the sferics each saturated in the first half-millisecond.

by the propagation time between the source of optical emissions and the observer. As shown in Figure 4-1, these dynamics result in later emissions being observed before earlier ones, and in an apparent downward and outward development of the flash, consistent with the predictions of *Inan et al.* [1996c].

Figure 5-6a shows the same model events as in Figure 5-2 but as seen from 745 km away with a broader field-of-view and with a higher time resolution. Both sequences show a flash which descends over the course of about 1 ms and exhibits the same upwardly concave curvature that was noted in connection with Figure 5-2. While the descent and curvature of the sprite halo represent true descent and curvature of the optical source, these features in elves are instead a result of the propagation geometry between the highly extended source and the observer.

Figure 5-6b shows $28^\circ\times8^\circ$ images of the predicted emissions from the QE and EMP cases, as would be observed from 745 km away by an instrument integrating over 2 ms. Modeled optical intensities shown here and in Figure 5-2 correspond to the total output of the first positive band of N_2 over its entire spectrum from 570 to 2310 nm. About 15% of this intensity would reach the Fly's Eye's red-filtered photometers in their passband of 650 to $\sim$780 nm. For the lightning parameters used here, the elve is only 8% as bright as the sprite halo when integrated over 2 ms. This example illustrates the fact that sprite halos are much easier to image with a 17 ms video field than are elves. However, the intensity of each phenomenon varies strongly with electric field strength, so either emission could be much brighter or dimmer than the cases modeled here, depending on the characteristics of the causative lightning current.

It has previously been established (see Section 4.1.2) that a horizontal photometer array with time resolution $\ll$1 ms is well suited for identifying elves. We now show how the photometric signatures of sprite halos compare to those of elves. Overlaid on the model images in Figure 5-6b are the fields-of-view of the Fly's Eye array (in blue) and of a $16\times(0.5^\circ\times9^\circ)$ multianode photometer (in green) similar to that used by *Fukunishi et al.* [1998].

Predicted photometric signatures are shown in Figure 5-7 in corresponding colors for EMP (solid lines) and QE (dashed lines) emissions. In both the vertical and horizontal photometer arrays, the initial signature of the "front" of the elve (i.e., luminosity produced at a point nearer than the CG to the observer — see Figure 4-1) is unambiguous. However, at later times, the "back" of the elve (i.e., luminosity produced beyond the CG, as seen by the observer) may be confused with that due to the upper part of the sprite. This feature could make it somewhat difficult to measure the downward propagation of the sprite halo in the vertical array,[‡] and also makes the horizontal array (Fly's Eye) configuration very sensitive to its viewing elevation angle. The modeled response of the Fly's Eye array takes into account the imperfect array alignment. This imperfection is reflected in the fact that photometers P1, P2, and P3 are viewing the "front" of the elve in Figures 5-6b and 5-7a, while P5 through P9 view the "back."

Figure 5-8 shows normal-speed video and photometric responses for three events recorded with the Fly's Eye using slightly different pointing elevations with respect to the observed flash. All three events produced elves and sprite halos. The event in Figure 5-8a includes an elve and sprites with a halo, but all the photometers are pointing high enough to observe the front of the elve. In Figure 5-8b the sprite halo, which occurred without any further sprite development, may be contributing to the enhanced brightness in P5 and P6. In Figure 5-8c the response of P5 and P6 is clearly dominated by that of the sprite halo, which again occurred without any apparent streamer breakdown.

In the most energetic sprites, any sprite halo is often followed very closely (<1 ms) by the much brighter filamentary sprite breakdown, so that all these emissions may not appear as distinct peaks in the photometric record.

[‡] Indeed, events previously identified as elves based on their downward progression in the vertical array used by Tohoku University are now being reanalysed as sprite halos [Rina Miyasato, *private communication,* 2000].

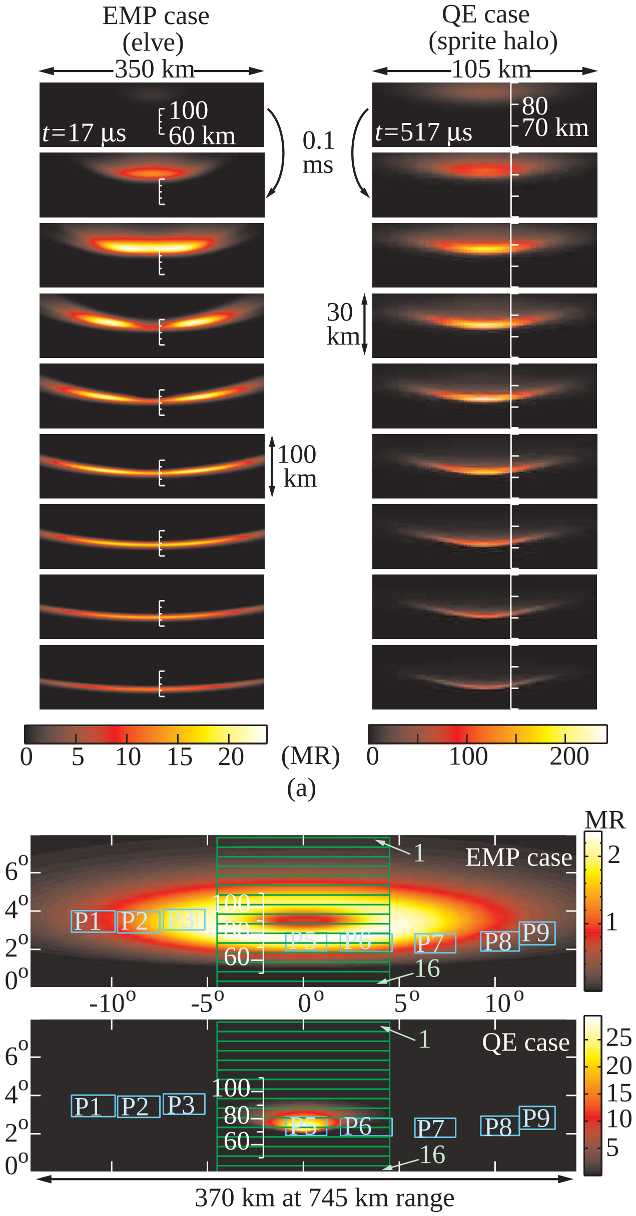

(a)

(b)

Figure 5-6: Modeled temporal development of elves and sprite halos. (a) 10 μs-long snapshots every 100 μs, viewed from ground level 745 km from the causative CG (from Figure 4-2). The QE and EMP sequences begin 17 μs and 517 μs after the lightning sferic would be received by the observer. Note the horizontal and vertical scale difference. (b) The flashes are shown integrated over 2 ms. Superimposed are the fields-of-view of two typical photometer arrays. The EMP cases were already shown in Figures 4-2 and 4-3.

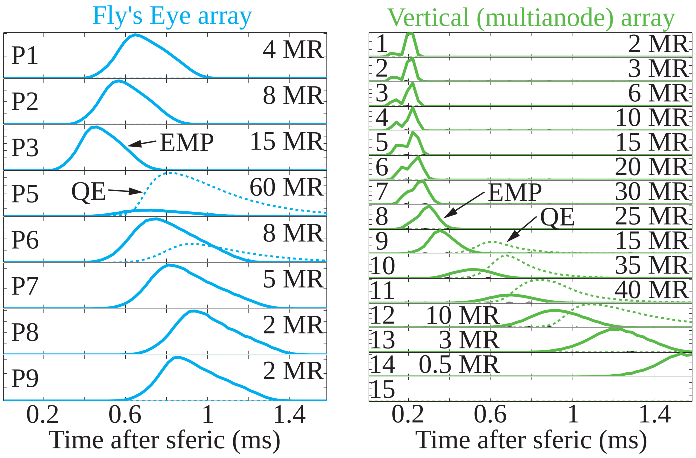

Figure 5-7: Predicted photometric array signatures. Predicted contributions from both EMP (solid lines) and QE (dotted lines) emissions are given for the horizontal and vertical arrays shown in Figure 5-6b.

5.1.5 Dependence on the ambient electron density

The distinctive shape, motion, and altitude range of the sprite halo of Figure 5-2 represents the first instance of an observed large-scale feature of sprites which can be accurately modeled in detail. These detailed features can potentially serve as a diagnostic tool for the ambient electron density profile at the time of the discharge. Figure 5-9 shows the modeled luminosity for three initial electron density profiles, using the lightning parameters and timing of the QE case in Figure 5-2. The ambient electron density n_e at altitude h follows the form [*Wait and Spies*, 1964]

$$n_e(h) = 1.43 \times 10^7 \text{ cm}^{-3} \exp\left[\left(-0.15 \text{ km}^{-1}\right) h'\right] \exp\left[\left(\beta - 0.15 \text{ km}^{-1}\right)(h - h')\right]$$

where we use $\beta = 0.5$ km^{-1} for each effective reflection height (for VLF signals) h' shown in Figure 5-9. For numerical efficiency, the ambient profiles were capped at 5×10^3 cm^{-3}. Both the intensity and shape of optical emissions vary with the D region height. Following well characterized lightning discharges, these optical emissions could reveal information about the local electron density profile over a thunderstorm. The case of h'=85 km was chosen as a best match for the observed sprite halo development in Figure 5-2c, remarkably consistent with the well known nighttime VLF reflection height of ~85 km [*Bickel et al.*, 1970].

5.1.6 Independence of sprite halos and streamer breakdown

The diffuse region of sprites has been previously described in the context of a QE model [*Pasko et al.*, 1995, 1997b] with the shape, size, and dynamics of optical emissions closely resembling those observed in the high speed video presented here, and is modeled with a more general fully electromagnetic model and more realistic viewing geometry in this work. The direct large scale (~100 km) modeling of the lower portion of sprites dominated by streamers using the QE model or the electromagnetic model used in this study is computationally not possible at present due to the extremely fine spatial resolution which is required to resolve individual streamer channels [*Pasko et al.*, 2000].

Ionization and optical emissions in the diffuse region and in the lower streamer region of sprites are observed to occur both as fairly separate events and as closely-coupled processes. The upper

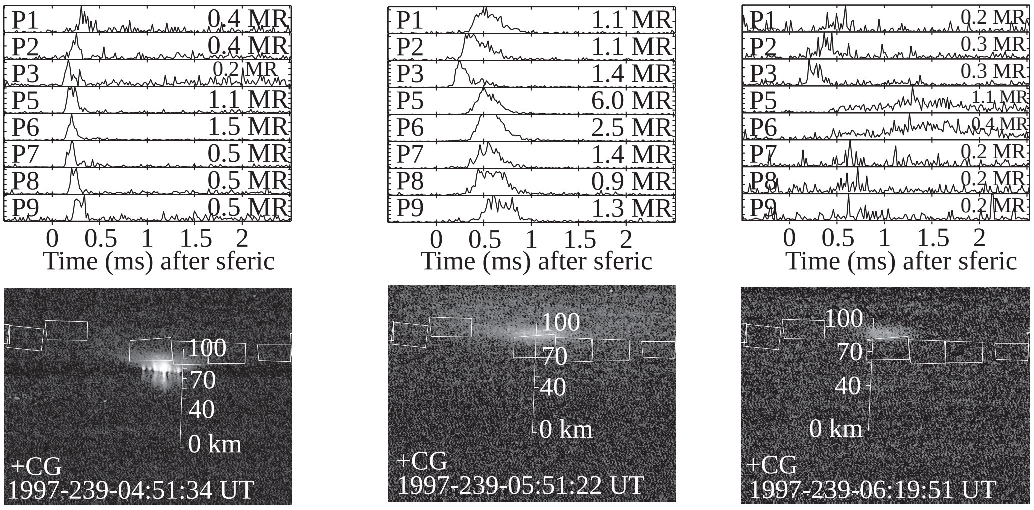

(a) (b) (c)

Figure 5-8: Photometry and enhanced video images from the Fly's Eye for three events exhibiting sprite halos. A sprite halo caused by a −CG is shown in Figure 5-1.

diffuse region of sprites [*Pasko et al.*, 1998a] is characterized by very fast relaxation of the driving electric field due to the high ambient conductivity associated with electrons at the lower edge of the ionosphere. The ionization process in this region of high electron concentration is theorized to be simple collective multiplication of electrons. In the lower streamer region of sprites, formation of streamer channels follows strong dissociative attachment of electrons (e.g., Figure 2-7 on page 30). The upwardly concave shape sometimes evident in sprite halos is due to enhanced ionization in the descending space-charge region. This extra ionization enhances the electric field outside (below) the region and appears to affect the formation of streamers.

However, because the time scale for electrical relaxation varies strongly with altitude, breakdown in the two regions can occur somewhat independently. A lightning discharge with a fast (<1 ms) charge moment change may be sufficient to cause diffuse emssions at higher altitudes, where the threshold for ionization and optical excitation is lower, but if lightning currents do not continue to flow, there may not be sufficient electric field to initiate streamers below $\sim$75 km. Conversely, slow continuing currents may cause a (delayed) sprite with streamers but without a significant initial flash in the diffuse region.

Although sprite halos in high speed video can be compared in detail with modeled luminosity, single-site recordings do not allow a robust experimental determination of their altitude distribution. Two-site triangulation of sprite halos was accomplished for the first time by *Wescott et al.* [1999], and further measurements using triangulation and high-speed imagers may be necessary to statistically characterize the initial development of either the halo or streamer regions of sprites.

5.2 Sprite polarity

Sprites have often been described as an electric discharge or breakdown at mesospheric altitudes occurring above large positive cloud-to-ground (+CG) lightning. While sprites are known to be associated with +CG discharges [*Sentman et al.*, 1995; *Winckler et al.*, 1996; *Lyons*, 1996], not all sprites closely follow such a discharge, or any recorded discharge at all [*Franz et al.*, 1990; *Boccippio*

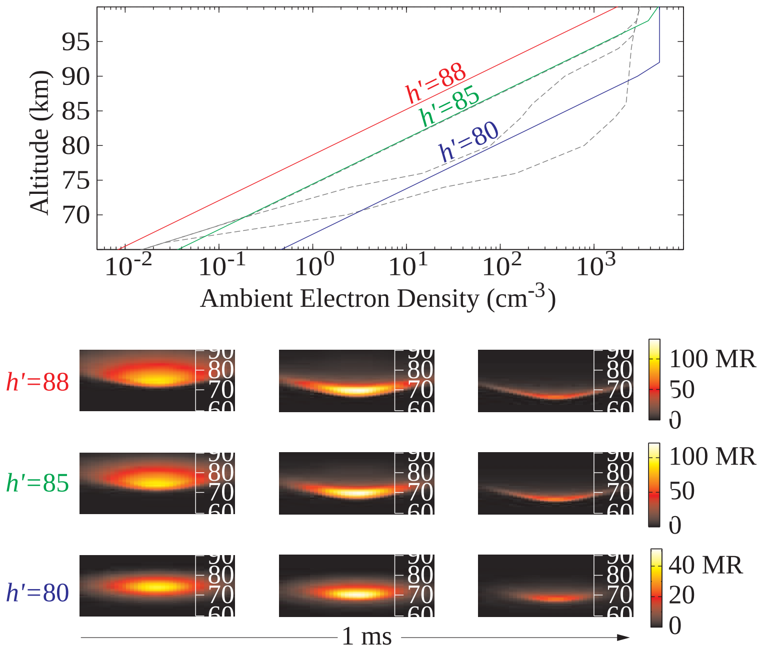

Figure 5-9: Ambient electron density profiles for three values of h', and the resulting modeled sprite halos. The $h' = 85$ km case corresponds to Figure 5-2c. Each image shows a region 30 km high by 105 km wide at a range of 875 km. Dashed lines show profiles used by *Pasko et al.* [1997b].

et al., 1995; *Winckler*, 1995]. *Winckler* [1998] reports three sprites each occurring within one second of nearby −CGs, but provides no specific evidence of an association closer than one second or 2° (∼11 km) of viewing azimuth. In our observations we regularly recorded sprites associated with a sequence of CGs spaced by 10 to 50 ms. More often, sprites are closely associated with a large +CG which moves a large positive charge (ΔM_{Qv} of 250 to 3250 C-km according to *Cummer and Inan* [1997]; 200 to 1100 C-km according to *Bell et al.* [1998]), and in the case of especially impulsive lightning (>60 kA; see Section 4.2) the CG is followed by elves. In this section, we report evidence of at least two sprites that are closely associated with negative cloud-to-ground (−CG) lightning strokes. Among our observations, these events are unique.

We use three lines of evidence to show that a storm over northwestern Mexico produced two −CG-associated sprites. Intensified broad-spectrum CCD video observations, triggered high-speed (60 kHz per channel) photometric array recordings, and both triggered and continuous ELF/VLF (350 Hz to 20 kHz) recordings were made in association with the Fly's Eye instrument stationed at Langmuir Laboratory on the night of 29 August 1998. The ELF/VLF antenna was oriented in a vertical plane 23° east of north. In addition, a calibrated ELF/VLF (10 Hz to 20 kHz) continuous recording with the same timing system was made at Stanford (37.42°N×122.17°W). These data were time aligned with the Langmuir Laboratory data and allowed a determination of the vertical currents flowing on time scales of 1 to 10 ms.

Table 5.1: NLDN-recorded large CG events (>60 kA) clustered around the −CG sprites, between the times 05:49:00 UT and 06:49:00 UT. Charge moment refers to the change in the first 5 ms after the onset of the sferic. Events 2, 15, 17, and possibly 18 were associated with observed sprites.

Event	Time (UT)	NLDN current (kA)	charge moment change (C-km)
1	05:49:13	−73	−230
2	05:49:23	+69	**+480**
3	05:49:31	−64	−110
4	05:52:39	−62	−120
5	05:52:51	−71	−140
6	05:53:07	−79	−370
7	05:53:30	−69	−280
8	05:54:23	−78	−80
9	05:56:47	−64	−140
10	05:58:28	−69	−120
11	05:59:22	−71	−130
12	06:01:00	−91	−270
13	06:09:36	−73	−310
14	06:10:02	−79	−200
15	06:11:14	−93	**−1550**
16	06:13:39	−64	−300
17	06:15:16	−97	**−1380**
18	06:18:14	−110	**−1340**
19	06:48:04	+120	+1000

5.2.1 Observations

A thunderstorm system centered at 112.7°W×29.8°N (inset, Figure 5-10) that was part of a major mesoscale convective system (MCS) over the northern Gulf of California in Mexico produced mainly −CG lightning on August 29. Figure 5-10 shows the +CG (+) and −CG (∘) discharges recorded by the National Lightning Detection Network with peak current >10 kA between 05:49 and 06:49 UT. The largest events (peak currents over 60 kA) in the storm region of interest are numbered and listed in Table 5.1. According to NLDN, no +CGs (>10 kA) occurred in this region during the 22 minutes prior to each of the two unusual events recorded at 06:11:14.808, and 06:15:16.305. Indeed, over the entire duration of the storm NLDN recorded only five +CG flashes from this active region, constituting ∼1.5% of the total flashes. In contrast, the larger MCS surrounding this region exhibited a +CG occurrence of ∼ 6%.

Figure 5-11a shows one of these unusual events, each of which consists of a closely associated −CG flash, an elves event, and accompanying sprites. NLDN recorded a −97 kA stroke (event 17 in Figure 5-10) at 06:15:16.305 UT. The polarity of the sferics recorded at Langmuir and at Stanford (Figure 5-11) is unambiguous at this range and confirms the polarity of the lightning. The bearing to this stroke and the altitudes overlying its location are shown on the video image. The video's pointing direction was determined with star field alignment (see Section 3.5.3). Photometers 1 through 9 show the distinctive signature (Section 4.1, *Inan et al.* [1997], and *Barrington-Leigh and Inan* [1999]) of elves, in the form of rapid lateral expansion and, along with P11, the characteristic onset delay after reception of the sferic, in this case ∼135 μs. After the luminosity due to elves abates (∼1 ms), however, P11 shows a distinct second pulse lasting until at least ∼5 ms after the

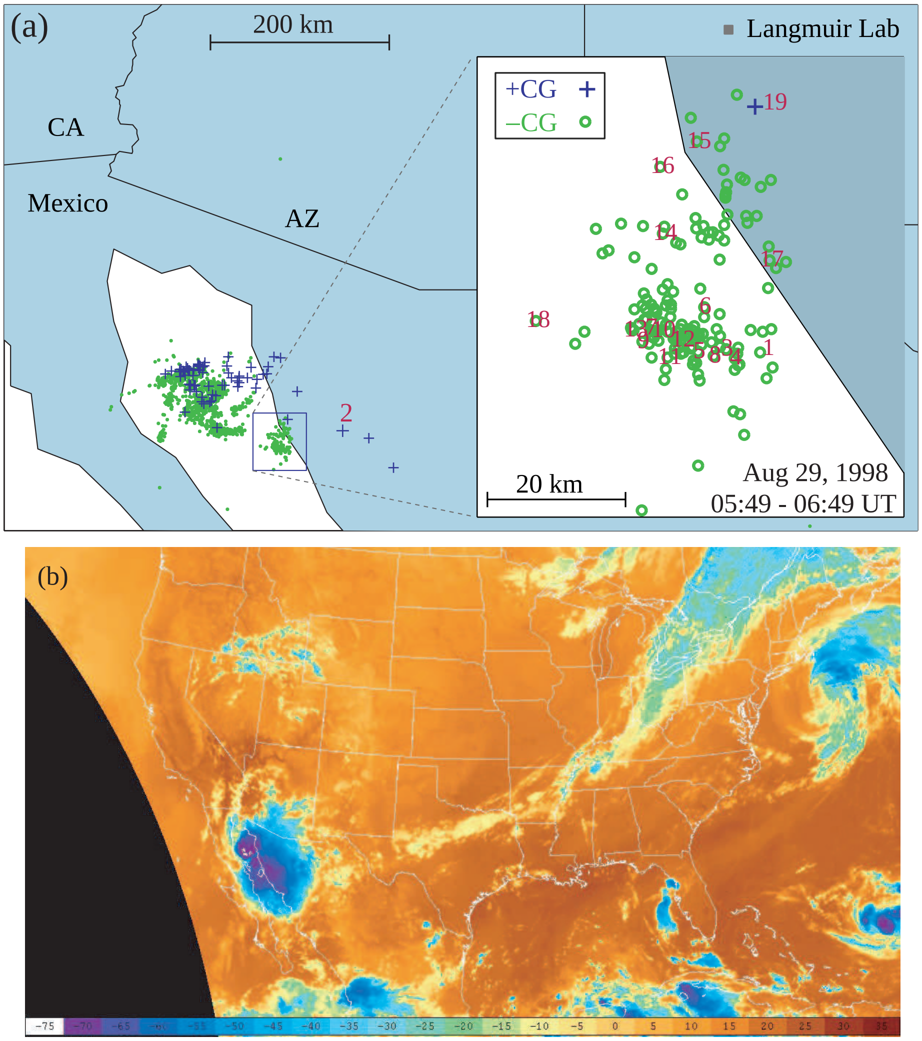

Figure 5-10: NLDN-recorded flashes from a nighttime MCS on 29 August 1998. The inset (a) shows the storm which produced many large −CGs. Numbered events are detailed in Table 5.1. (b) An infrared weather map for the same time.

onset of the sferic. In our recordings such a photometric signature from a distant storm is always accompanied by video observations of sprites, and indeed the video frame for this time (Figure 5-11b and 5-11c) shows clear evidence of sprites with vertical (columnar) structure, despite intervening cloud cover and the large distance (694 km) of the storm from Langmuir Laboratory. The full vertical extent of the sprites is difficult to ascertain, as their apparent lower limit may be due to a foreground cloud. Figure 5-11 also shows the vertical current moment and cumulative vertical charge moment change ΔM_{Qv} extracted from the calibrated sferic receiver at Stanford with the method described in *Cummer and Inan* [1997] and (in improved form) *Cummer and Inan* [2000]. By 5 ms after the arrival of the sferic, $\Delta M_{Qv} \simeq 1380$ C-km, indicating an abnormally high continuing current for a −CG [*Uman*, 1987, p. 172 and 341]. The charge moment change before the onset of the second optical peak, or by about 1.38 ms after the onset of the sferic, is 750 C-km, well above the 250 C-km threshold observed for the production of sprites associated with +CGs in *Cummer and Inan* [1997].

Figure 5-12 shows another similar event, corresponding to a −CG recorded by NLDN at 06:11:14.808 UT with peak current of −93 kA. This discharge (event 15 in Figure 5-10) produced similar unambiguous video recording of columnar sprite luminosity between 70 and 80 km through an opening in the foreground clouds. The photometric channels and ELF sferic also exhibit evidence of elves and a high current moment, respectively. None of the photometers are pointed directly at this sprite, however, so none of the photometers shows an obvious second pulse in luminosity for the event.

Event 18, recorded at 06:18:14.239 UT, has very similar properties as the two others, but because the region below ~80 km altitude was blocked by clouds, only diffuse light reached the video or P11 (Figure 5-13). Nevertheless, the photometry and localized brightness in the video image is suggestive of a sprite event similar to those of Figures 5-11 and 5-12.

5.2.2 Discussion

The interpretation of these observations is not limited by the detection efficiency of the NLDN. While the NLDN analysis algorithms occasionally (less than once in 1000 flashes) misplace a CG by up to 50 km, they more typically assign a location with an accuracy of ~500 m [*Cummins et al.*, 1998b]. Also, the stroke detection efficiency, while low for peak currents <5 kA, improves markedly for peak currents >15 kA within the network [*Cummins et al.*, 1998b]. Regardless, the continuous wideband VLF recordings at Langmuir and Stanford record all sferics without exception, and these data preclude the possibility of a significant +CG having been missed by NLDN and having contributed to the sprites. No sferics caused by +CGs with peaks >0.07 nT as measured at Stanford were recorded within 200 ms of event 17, within 800 ms of event 15, or within 200 ms of event 18.

Each of the two −CGs accompanied by observed sprites, as well as the −CG of event 18, transferred remarkably large charges as determined from the first 5 ms of the sferic. Within 5 ms of each lightning stroke, downward charge moment changes of −1550 C-km, −1380 C-km, and −1340 C-km were brought about by the discharges in the three cases shown in Figure 5-11, 5-12, and 5-13. Based on the shape of the current-moment waveforms, which have a large initial pulse, these values of vertical charge moment change are likely mostly due to the cloud-to-ground stroke rather than the sprites themselves [*Cummer et al.*, 1998b].

Current-moment extractions were also performed for the other large (>60 kA) lightning strokes recorded by NLDN in the vicinity of the sprites and during the time period 05:49 UT to 06:49 UT. Event 2, a +69 kA CG shown in Figure 5-10, was due to a different storm but also produced sprites. Nevertheless, this return stroke sent only +480 C-km to ground in its first 5 ms. Interestingly, event 19, a +120 kA CG which occurred after 20 minutes of inactivity in the storm studied, led to an elve and produced a 5 ms charge moment change of +1000 C-km but no recorded sprites (if any occurred, they must have been optically weak). Several other moderately large (−70 to −90 kA)

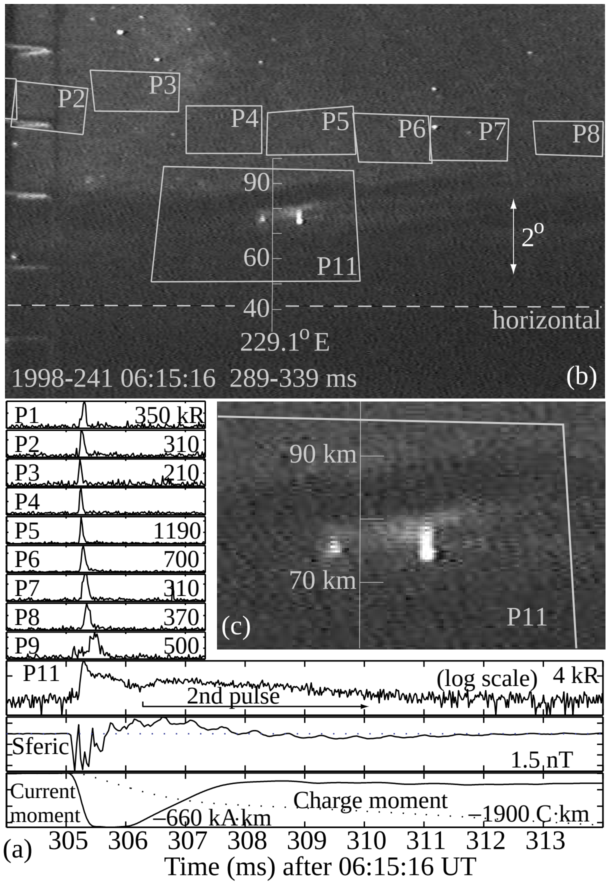

Figure 5-11: Sprite associated with a large −CG return stroke and continuing current. (a) Photometer responses, recorded lightning sferic, and the inferred current moment for event 17 from Table 5.1. Scales are linear, except for that of P11. The wide field video view in (b) shows the measured fields-of-view of the photometers, including the observed sprite within the field-of-view of P11. The image consists of two interlaced fields, exposed from 289 ms to 322 ms and from 306 ms to 339 ms, both of which show the sprite. A closeup of the sprite is shown in (c). Vertical altitude scales indicate the azimuth of the −CG according to NLDN.

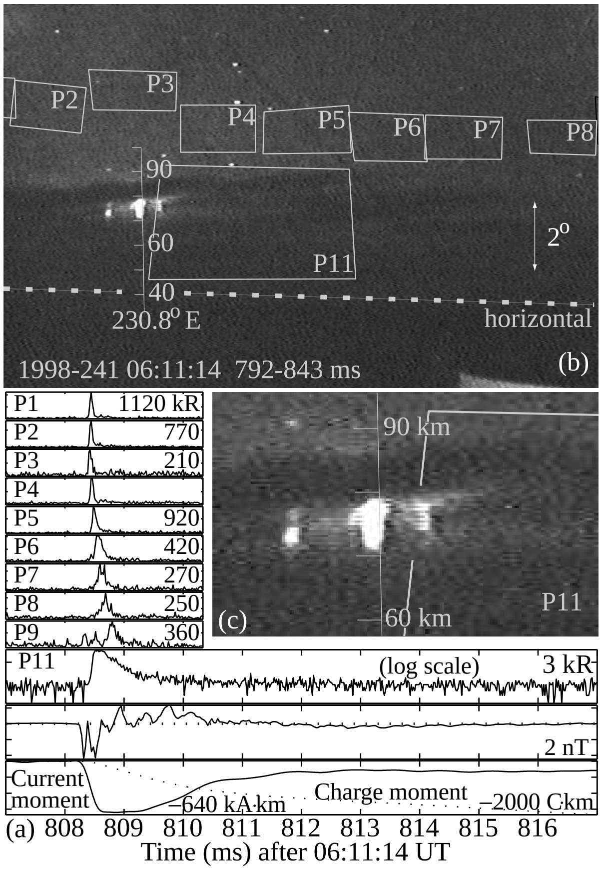

Figure 5-12: Negative sprite at 06:11:14 UT. Like Figure 5-11, but for event 15. P11 may have missed the light due to the sprite.

−CG strokes listed in Table 5.1 produced charge moment changes of ∼300 C-km or more within 5 ms.

In contrast, values of vertical charge moment change for −CGs in the rest of the MCS were considerably smaller. The two largest −CG return strokes recorded during the period 05:49 to 06:49 UT in the very active system northwest of the storm studied (*i.e.* in the rest of the MCS) were listed by the NLDN with peak currents of −120 kA and −156 kA, but had charge moment changes of only −190 C-km and −180 C-km, respectively, within 5 ms.

Our method of current-moment extraction is sensitive only to vertical currents on timescales less than ∼10 ms. Nevertheless, the existence of the −CG-associated sprites documented here leads to several important conclusions:

Sprite polarity asymmetry: Sprites are not uniquely associated with +CGs and therefore are apparently not uniquely associated with downward electric fields in the upper atmosphere. By analogy to the vertical electric field direction associated with +CGs and −CGs, we can classify sprites as “positive sprites” (downward electric field) and “negative sprites” (upward electric field). Our observations of “negative sprites” apparently eliminate the relativistic runaway breakdown mechanism [e.g., *Roussel-Dupre and Gurevich*, 1996; *Lehtinen et al.*, 1997] as an explanation for the optical emissions in at least a subset of sprites, since this mechanism requires a downward

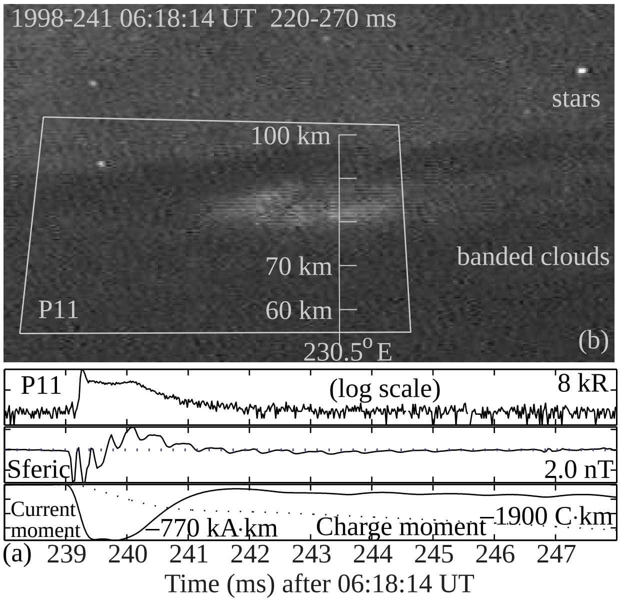

Figure 5-13: Negative sprite at 06:18:14 UT. Like Figure 5-11, but for event 18. Photometers P1-P9, not shown for brevity, recorded a signature of elves, similar to the other events.

directed electric field. The association between relativistic runaway breakdown and optical emissions in sprites has also been refuted theoretically by *Lehtinen et al.* [1999]. On the other hand, our observations are in accord with conventional air breakdown models of sprites, and suggest that the most important distinguishing feature of +CG strokes for sprite production is simply their unusually large continuing current as compared with most of the typical −CG strokes. Figure 5-14 shows examples of positive and negative streamers in positive sprites, supporting the same conclusions.

Determining sprite polarity: Sprites which occur without an unambiguous association with a CG return stroke cannot be automatically assumed to be positive sprites. Instead, a measurement of the sprite current moment from ELF recordings would be necessary to unambiguously determine sprite polarity in these cases. High-resolution imagery may also help to determine sprite polarity, as suggested by the observation of qualitative differences in characteristics of faint, broad positive streamers and brighter, more structured negative streamers in telescopic video recordings from 1998, as exemplified by the events shown in Figure 5-14. It remains to be seen whether higher resolution images of negative sprites similarly exhibit streamers in both directions and whether their vertical extents are comparable to those of positive sprites.

Exception proves the rule: Except in the storm described here, our observed sprites (and even those described by *Winckler* [1998]) have occurred in storms producing large-current +CGs. While we often see sprites which appear to be associated more with a “spider lightning” (intracloud) propagating series of CGs (usually mostly +CG, but often with some −CGs too) rather than with the precise azimuth and time of any particular (+)CG, the negative sprites observed here were centered in azimuth over the respective −CGs, which in turn occurred in isolation. In particular, there was no other NLDN-recorded lightning within ∼10 s and ∼60 km of the causative flashes, nor were there any other candidate sferics preceding the sprites in wideband data. Ultimately, an understanding of how charge-transfer processes can lead to sprites from propagating series of modest-current +CGs but rarely from even large multi-stroke −CG clusters may lie almost entirely

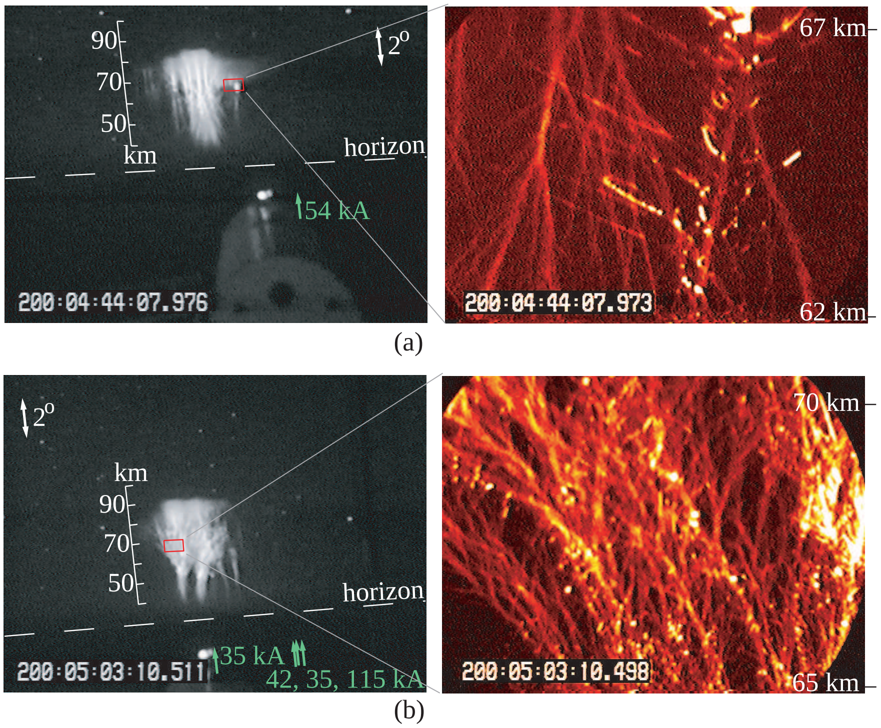

Figure 5-14: Positive and negative streamers in positive sprites. The right hand panels show telescopic video views (see *Gerken et al.* [2000] for a description of equipment) regions identified in the Fly's Eye images on the left. The cloud-to-ground strokes were all positive, implying a downward electric field in the high atmosphere. (a) These downward branching structures can be deduced to be formed by positive streamers in a downward electric field. (b) These upward branching structures must be formed by negative streamers.

in cloud physics rather than in any asymmetry in mesospheric breakdown processes. This difficulty is compounded experimentally by the problem of measuring horizontal (intracloud) ELF/VLF currents, which do not produce vertical electric fields nor horizontal magnetic fields in the near-field (except above and below the discharge) and do not efficiently couple to Earth-ionosphere waveguide modes below ~1.5 kHz (see Section 3.1). Electric field measurements above or below storms producing recorded sprites are a worthy goal in this regard.

5.3 Exponential optical decay and steady electric fields

Several criteria used for the identification of elves in narrow field-of-view photometers are discussed in Chapter 4. One additional criterion not mentioned there is the fast relaxation time scale ($<100\ \mu$s) which is often a characteristic of optical pulses due to elves. Such fast relaxation is not typical for scattered light from lightning [*Thomason and Krider*, 1982; *Guo and Krider*, 1982], and observations outlined below show that it is also generally not observed for sprites.

On the night of 19 July 1998 a large mesoscale convective system over northwestern Mexico produced exceptionally bright sprites. Measurements were made from Langmuir Laboratory using the Fly's Eye camera, optical array, and VLF receiver, as well as an image-intensified telescopic video system described by *Gerken et al.* [2000]. In addition, many sprites were bright enough to be visible to the unaided and unadapted eye.

Determination of total sprite luminosity lifetimes has generally been challenging [*Rairden and Mende*, 1995; *Winckler et al.*, 1996]. Video recordings give generally poor time resolution and some systems, such as the image intensifier of the Fly's Eye video, exhibit a phosphor persistence following intensely bright signals. This "afterglow" may last for several frames, making the instrument unreliable for quantifying long sprite durations. On the other hand, photometers designed with high time resolution are not optimized for the measurement of slowly varying, weak signals, especially in the near infrared region of the spectrum [*Winckler et al.*, 1996]. In the Fly's Eye photometers, the slow glow of sprites often appears to decay gradually into the background photometer signal level. Extra bright sprites facilitate the measurement of these longer timescales using the Fly's Eye.

Sprites are known sometimes to occur well after (up to tens of milliseconds) an associated lightning return stroke [*Bell et al.*, 1998]. It has been proposed that this property may be due to slowly-varying currents, possibly undetectable by ELF radio measurements, which may be flowing along the ionized return stroke channel or possibly horizontally within the thundercloud [*Bell et al.*, 1998; *Cummer et al.*, 1998b; *Cummer and Stanley*, 1999]. In some cases, a series of (positive) cloud-to-ground discharges may occur sequentially over a large horizontal distance within a fraction of a second (spider lightning), suggesting the existence of an expansive travelling network of intracloud currents [*Lyons*, 1996]. These events are typically accompanied by a series of sprites mirroring the propagation of the lightning below ("dancing sprites"). In such cases several sprites can occur with continuous luminosity over a large fraction of a second and may appear to be associated with several lightning strokes. This paradigm was typical for the sprites observed on 19 July 1998.

In the following sections, several notable features of sprites are discussed in the context of the observations carried out on 19 July 1998. The extra signal available on this night may have highlighted some hard-to-observe but common features of sprites, or the observations may correspond only to the special case of unusually intense ionization and emissions. Several studies have suggested that the degree of ionization in sprites can vary greatly and somewhat independently of the intensity of luminous emissions [*Armstrong et al.*, 1998b; *Heavner et al.*, 1998; *Armstrong et al.*, 2000].

5.3.1 Timescales in sprite photometry

Figure 5-15 shows a sample photometric record of a bright sprite, and illustrates the existence of more than one time scale in sprites. The inset image shows an intense sprite halo and bright patches near its lower boundary at ~75 km which appear to have initiated downward streamers in a manner similar to that described by *Stanley et al.* [1999]. This event is accompanied by the photometric signature of elves (Section 4.1) in the full array of photometers (not shown). In photometer 4 (shown) the initial optical pulse due to elves becomes very bright and is protracted for >2 ms. This brightness is likely to be due to the sprite halo evident in the video image. Approximately 6 ms after the event onset a pulse with characteristic rise and fall times both of ~2 ms appears and then relaxes into >50 ms of less intense glow.

This example highlights several features of sprites which were frequently observed on 19 July 1998 and in the course of the annual sprite campaigns conducted by the author. Many events exhibit a bright peak which is often only a few ms in duration and tends to grow and decay with similar timescales. In addition, overall photometric durations much larger than 10 ms were found to be normal on this day, in contrast to the observations of *Winckler et al.* [1996].

Cummer and Stanley [1999] found that the peak in optical intensity of sprites occurred after the propagation of streamers to their lowest altitudes was complete. The same phenomenology is observed for the event shown in Figure 5-2 and may be analogous to the luminous return stroke of lightning following the connection of a leader channel to ground. In this analogy, the slower sprite

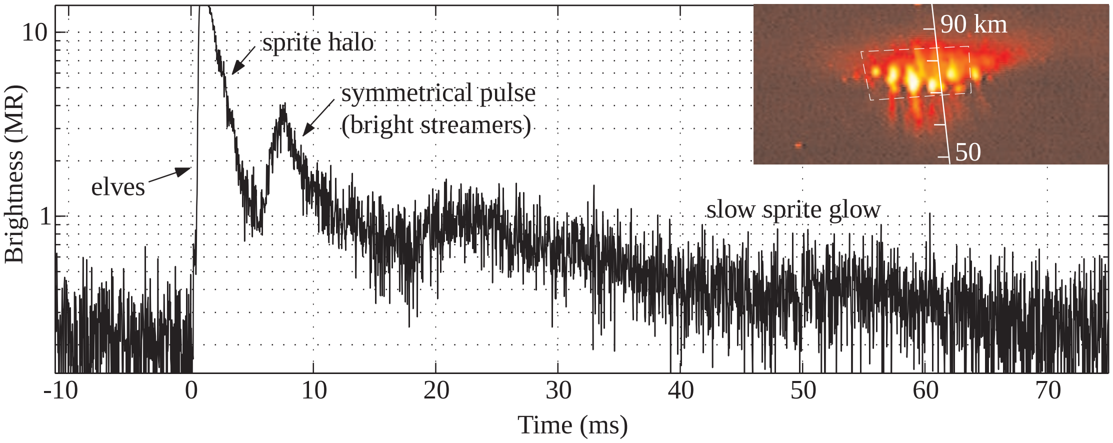

Figure 5-15: Photometric features of a bright sprite. The signal from photometer 4 is shown for part of an event at 04:38:27 UT on 19 July 1998. This sprite occurred 0.5 s after a series of intense sprites associated with a series of positive cloud-to-ground lightning discharges. The inset shows a video field of the sprite from the Fly's Eye camera, superposed by a box showing the approximate field-of-view of the photometer and a scale showing altitudes overlying a causative CG.

glow evident in Figure 5-15 may correspond to lesser excitation of the channel during the analogue of the continuing current phase in lightning.

5.3.2 Observations of exponential optical decay

Measurements from the Fly's Eye's video camera, ELF/VLF sferic receiver, and three photometers, as well as from an ultra low frequency (ULF, <30 Hz) search coil, are shown in Figures 5-16 and 5-17.

Several notable features are apparent in the event shown in Figure 5-16. Two cloud-to-ground discharges cause sprites exhibiting both short, bright features and a longer dimmer luminosity which is not well resolved by the photometers. It is likely that this sprite sustained some luminosity during the entire time between the two lightning discharges. The ULF magnetic field indicates the existence of a vertical current flowing continuously for >140 ms during this period. Figure 5-17 shows the unusual fact that the brightening of the sprite in photometer 11 appears to anticipate the onset of the second cloud-to-ground discharge.

The dashed lines superposed on the photometer traces in Figure 5-17 show curves of the form

$$y(t) = C + Ae^{-t/\tau} \tag{5.1}$$

fit to the data by choosing values of C, A, and τ. The decay of bright optical peaks in sprites is found in a large number of cases to closely follow the exponential form in (5.1) over several time constants τ, although the value of τ varies considerably between different optical peaks. This rather remarkable feature of sprite optical decay has not previously been reported.

An electric field imposed on a conductive medium by a rapid rearrangement of charges is expected to decay exponentially in time (see Section 1.3, page 3). Indeed, the typical timescales τ for the observed decay are comparable to expected electric relaxation times $\tau_{\mathrm{E}} = \epsilon_0/\sigma$ at the observed altitudes. However, according to Figure 2-4 on page 25 the optical emissions should not

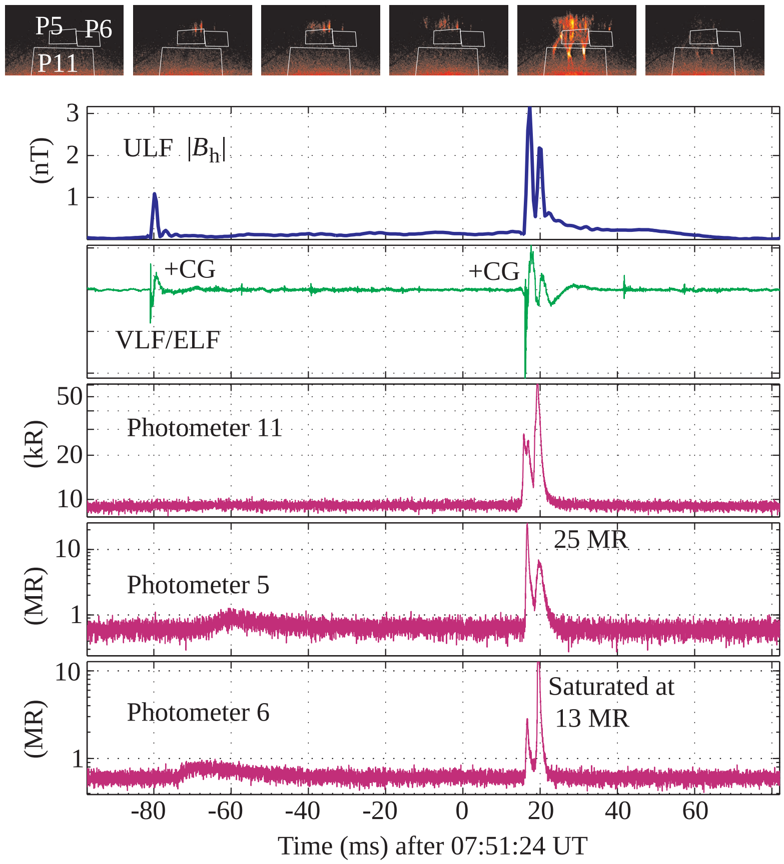

Figure 5-16: Slow sprite development and ULF currents. The ULF magnetic field is obtained by integrating in time data from a magnetic loop receiver. ULF data were data provided by Martin Füllekrug. According to NLDN, the two lightning discharges were 31 km apart.

relax exponentially in such a case because of their highly nonlinear dependence on the electric field strength.

On the other hand, the observed exponential relaxation would be obtained if we adopt the *ad hoc* assumption that the electric field remains constant in time. Such an assumption was first proposed in March 1999 [Victor Pasko, *private communication*].

For an altitude where quenching is insignificant and with the assumptions used for equation (2.18), the optical emission rate is

$$A_k n_k \simeq \nu_k(E) n_e(t), \qquad (5.2)$$

where in this case ν_k for $N_2(1P)$ is effectively equal to $\nu_{B^3\Pi_g} + \nu_{C^3\Pi_u}$ due to cascading. That is, the emission rate is the product of the electron density and a nonlinear function of the electric field, E. However, for $E{=}E_0{=}$constant, $A_k n_k \simeq \nu_k(E_0) n_e(t)$ and we have from equation (2.15),

$$n_e = n_e\Big|_{t=0} e^{[\nu_i(E_0)-\nu_a(E_0)]t}, \qquad (5.3)$$

where $\nu_i - \nu_a$ is shown in Figure 2-4 and is also constant in time for $E = E_0$. For $E_0 < E_k$ in a sprite, this condition would produce an exponential optical relaxation.

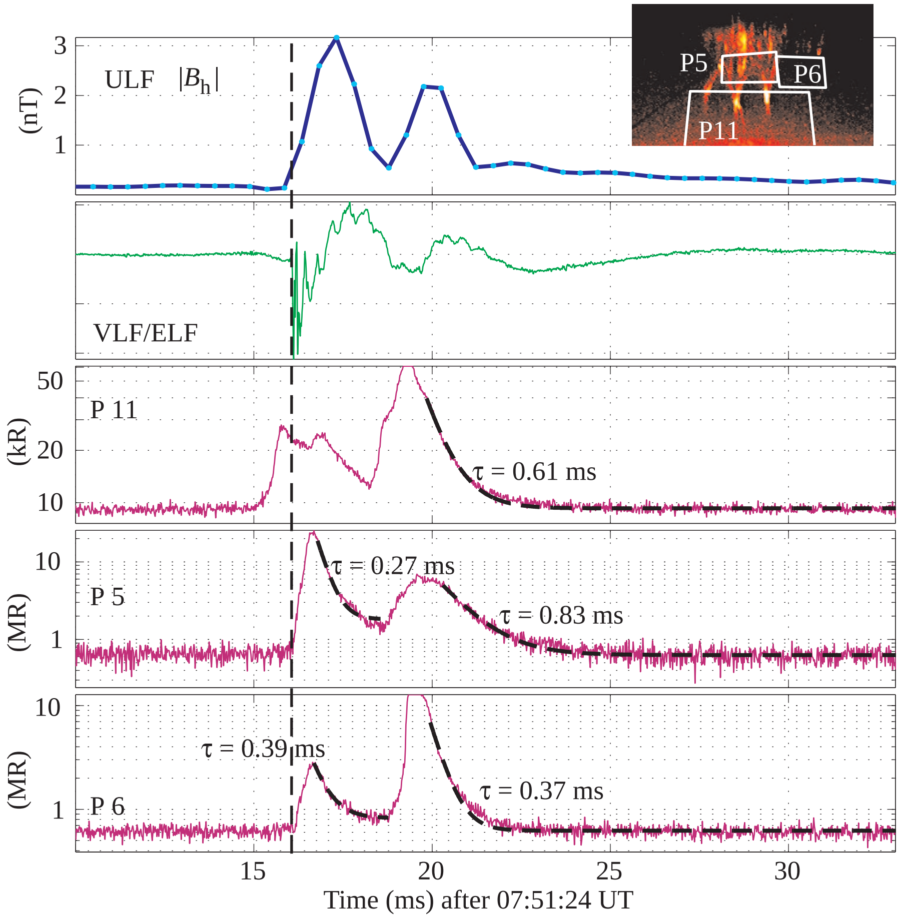

Figure 5-17: Sprite preceding cloud-to-ground lightning. A close-up of Figure 5-16.

It may be cautioned that a wide variety of physical systems may be well approximated by exponential behavior, sometimes due to statistical or geometric reasons rather than those relating to local physics. For instance, in the case of elves the temporal structure of optical emissions is locally determined by temporal properties of the causative lightning pulse, and at a ground observer site is determined largely by geometrical considerations. These geometrical effects can lead to an apparently closely-exponential relaxation of luminosity from the "back" part of elves both in theory and observations for the case of a photometer with a field-of-view as large as that of P11 in the Fly's Eye.

Nevertheless, the exponential decay feature is found in a majority of the bright sprites observed between 04:00 and 06:00 UT on 19 July 1998 and often with a more exact fit than the cases shown in Figure 5-17. Figure 5-18 shows values of the relaxation time constant τ determined for peaks observed in 27 events exhibiting good to excellent closeness of fit between equation (5.1) and the data in narrow field-of-view photometers 1 to 9 (red filter) and 10 (blue filter). The altitudes corresponding to the narrow fields-of-view for these observations were primarily in the range 60 km to 85 km, with considerable uncertainty (±12 km) based on the possible range to the sprites, as explained on page 61 (Section 4.1.4).

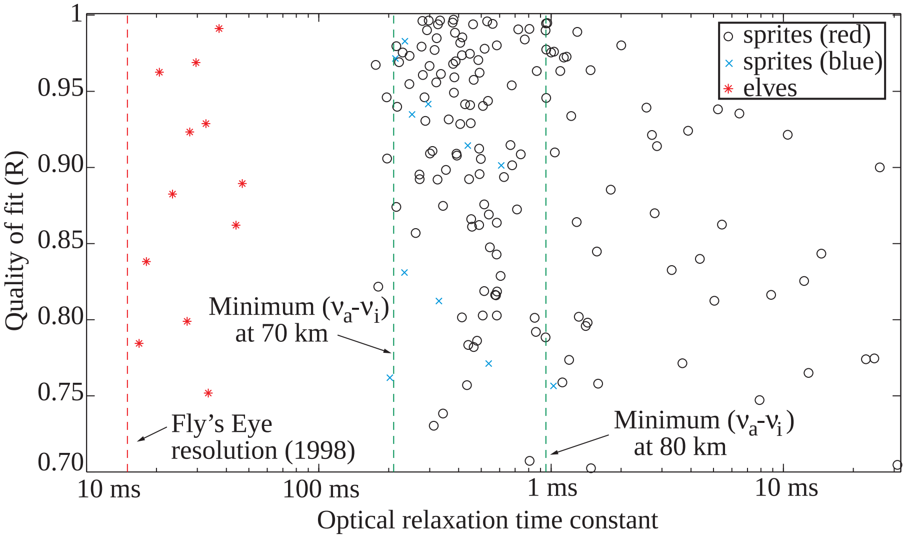

Figure 5-18: Exponential decay times in sprites. Values shown as ×'s and ○'s are from fits giving $R > 0.7$ using data from one or more photometers in each of 27 sprite events. The *'s show the result of fits to photometric signatures of elves.

The curve fitting is done by a nonlinear least squares algorithm for periods chosen by hand to correspond well to a decaying exponential form. In some cases the initial period following a bright peak relaxes faster than the exponential fit, and not all of it is included. Instead, whenever possible, the fit period includes many times the duration of τ so as to appropriately fix the value of C in equation (5.1) to the background luminosity. The quality, or closeness, of fit is then assessed by comparing the values of $\log(y - C)$ from data and fit using the linear correlation parameter R given by *Bevington and Robinson* [1992, p. 199].

Also shown for reference are some time constants determined with the same algorithm and associated with optical pulses from the same storm but which were determined to be due to elves. The apparent close fit in these cases, however, is less significant since the parameter τ is barely resolved by the sample period of the photometer. Nevertheless, the values of τ given for elves in Figure 5-18 do give an indication of the time scales for the optical signals due to elves viewed with a narrow field-of-view. The sample period of the data is shown by a dashed vertical line.

It is apparent that while the instrument and the fitting method are capable of resolving decay constants well below 100 μs, and while the measured variation in τ extends over nearly two orders of magnitude for sprites, a lower limit of $\sim$200 μs exists among the observed sprite cases.

Two more dashed vertical lines show the fastest rate constant expected at two different altitudes for $n_e^{-1}(\partial n_e/\partial t)$ in the region where dissociative attachment dominates over ionization. As shown in Figure 2-4 on page 25, this rate $\tau_{\mathrm{a}}^{\mathrm{min}}$ is reached at $E \simeq 0.8E_k$ and is also the fastest optical relaxation that is predicted for a constant electric field, according to equation (5.2). Figure 5-19 reproduces some time scales previously shown in Figure 1-1 as frequencies. Included is the variation of $\tau_{\mathrm{a}}^{\mathrm{min}}$ with altitude. The suggestion that the observed optical relaxation rate may be bounded by the maximum rate of $(\nu_{\mathrm{a}} - \nu_{\mathrm{i}})$ supports the *ad hoc* assumption of an essentially constant electric field during these times.

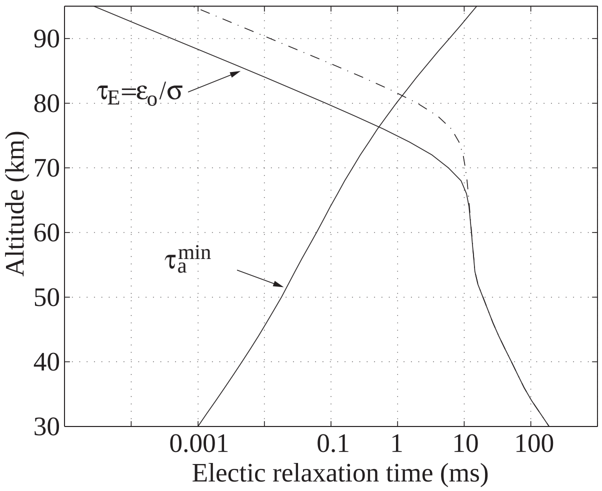

Figure 5-19: Electric relaxation and attachment time scales as a function of altitude. $\tau_{\mathrm{a}}^{\mathrm{min}}$ corresponds to the two-body dissociative attachment rate at $E{\simeq}0.8E_k$; see Figure 2-4. The dashed line shows τ_{E} for $E{=}E_k$.

5.3.3 Steady electric currents

It is remarkable that a constant electric field should arise so frequently in a dynamically driven conducting medium. One likely scenario is the existence of a constant source current term in the troposphere over a time long compared to the local relaxation time τ_{E}. As an example, if a thundercloud vertical charge moment change of 1000 C-km is required for E to exceed E_k at some altitude, then if $\tau_{\mathrm{E}}{\simeq}1$ ms, a steady-state electric field of $E{=}E_k$ could be sustained only by a current moment of 1000 kA-km. This value is comparable to the peak current flowing in a powerful return stroke.

This relationship between current and electric field may be quantified as follows. Because of the finite atmospheric conductivity, an infinitesimal charge moment change $\mathcal{I}(\tau)L\,d\tau$ makes a contribution dE to the instantaneous electric field at time t which decays with time constant τ_{E}. That is,

$$dE(t) = \alpha\,\mathcal{I}(\tau-\Delta)\,L\,e^{(t-\tau-\Delta)/\tau_{\mathrm{E}}}\,d\tau, \quad t > \tau+\Delta \tag{5.4}$$

for some proportionality α, and where Δ is the speed of light propagation time. The total electric field at time t is then

$$E(t) = \alpha\int_{-\infty}^{t-\Delta}\mathcal{I}(\tau-\Delta)\,L\,e^{(t-\tau-\Delta)/\tau_{\mathrm{E}}}\,d\tau \tag{5.5}$$

If the current $\mathcal{I}(\tau)$ is constant (that is, if it has been constant over time $\tau \gg \epsilon_0/\sigma$) then the integral evaluates to

$$E(t) = E_0 = \alpha\,\mathcal{I}_0\,L\,\tau_{\mathrm{E}} = \alpha\,\mathcal{I}_0\,L\frac{\epsilon_0}{\sigma}. \tag{5.6}$$

Theoretical studies [e.g., *Pasko et al.*, 1997b] suggest that sprite breakdown occurs after the integrated charge moment change surpasses a value needed to exceed the breakdown electric field. Judging from Figure 5-19 this "integration" may occur over times of up to ∼5 ms at 75 km altitude, in accordance with equation (5.5). However, once the breakdown threshold is reached the electron density may increase rapidly (for instance through streamer breakdown) on timescales much faster than $\tau_{\mathrm{a}}^{\mathrm{min}}$ and as a result the conductivity may increase drastically and the value of τ_{E} could be reduced to much less than that shown in Figure 5-19 for the ambient electron density. As a result, the electric field would rapidly decay (with time scale τ_{E}) to the steady state value E_0 given in (5.6) and thereafter the electron density and optical emissions would decay exponentially (with time scale τ_{a}) for any case in which $E<E_k$. This entire sequence of events could occur with no temporal variation in the tropospheric source term $\mathcal{I}_0 L$.

With this view, the initial non-exponential decrease following an optical peak before a closely-exponential form is observed may correspond to the establishment of a steady-state electric field E_0. A complication to the interpretation of this sequence of events when streamers are involved is the difficulty of carrying out a theoretical calculation of the ionization level left behind a propagating streamer, where the electric field is expected to be quite low [*Bazelyan and Raizer*, 1998]. In light of the work of *Cummer and Stanley* [1999], the sequence of events described above might occur after the initial propagation of streamers is complete and may apply to the reexcitation of the remnant channels.

In any case, the measurement of exponential optical relaxation constants may constitute a significant new method for remotely sensing the local electric field within a sprite. For a given altitude observed within a narrow field-of-view, and with the assumption that $E<0.8E_k$, the observed relaxation time constant τ determines $\nu_{\mathrm{i}} - \nu_{\mathrm{a}}$ which in turn prescribes E. In addition, according to the interpretation presented here, this observation gives non-spectral evidence of significant ionization changes. However, when taken alone it is likely not useful for measuring absolute electron densities. On the other hand, it does suggest in accordance with equation (5.3) that the free electron population likely becomes almost completely depleted in these regions where the electric field remains constant (and below E_k) for durations several times τ_{a}.

The ULF magnetic field data shown in Figure 5-16 indicate that an essentially time invariant continuing current in lightning is a realistic possibility, even over many milliseconds. Recent unpublished work by Steven Cummer and Martin Füllekrug has used such ULF data to infer the vertical source lightning currents with a method similar to that previously used for ELF recordings [*Cummer and Inan*, 1997; *Cummer et al.*, 1998b; *Cummer and Stanley*, 1999; *Barrington-Leigh et al.*, 1999a; *Cummer and Inan*, 2000]. The inferred vertical current moments were as high as 40 kA-km for 160 ms and may account for sprite breakdown in long-delayed sprites even without appealing to unmeasured horizontal charge motion, an idea which was invoked to explain previous ELF/VLF results.

On the other hand, the occurrence of a sprite just preceding the return stroke in Figure 5-17 suggests that a large (horizontal) charge motion within the cloud may have both led to a sprite and been involved in the initiation of the return stroke, indicating that horizontal currents may indeed be sufficient to initiate sprites without vertical (return stroke) charge motion. According to NLDN, the second return stroke was in a new location from the previous one. The time scale for stepped leader breakdown is >10 ms altogether, and ~ 1 ms for the final leader pulse preceding the return stroke [*Uman*, 1987, p. 14-16], implying that the channel taken by the second return stroke in Figure 5-16 must have been developing well before the onset of the bright optical signature. An alternative interpretation for the peculiar observation of a sprite immediately preceding the second return stroke is that the timing of the sprite onset with respect to the return stroke is coincidental. However, given the 31 km proximity of the two lightning strokes as reported by NLDN, it is likely that they were closely coupled electrically through intracloud currents.

For reasons discussed previously (Section 3.1), it is difficult to determine experimentally the relative contributions of vertical and horizontal charge motions in the production of mesospheric electric fields. The results reported above give evidence of sustained source currents of one kind or another without discriminating between them.

Chapter 6

Conclusions and Suggestions

6.1 Conclusions

The major results of this work may be grouped as follows.

Indirect measurement of ionization

Determining the degree of ionization in sprites has been a recurring theme and point of debate over the last decade, largely due to the difficulty of measuring optical output from emission-lines of ionized molecular states. However, based on the modern understanding of the streamer breakdown process [*Pasko et al.*, 1998a, 2000] it seems incontrovertible that intense ionization occurs when filamentary structure is seen in sprites, although this ionization may occur only briefly [*Armstrong et al.*, 1998a]. In this work we have shown three additional ways to infer the existence and degree of ionization in sprites and elves:

- With the help of modeling, upwardly-concave curvature in sprite halos can be interpreted as a sign of intense ionization augmenting conductivity gradients and preferentially expelling the electric field.
- The exponential relaxation of sprite luminosity appears to manifest ionization changes, typically over more than one order of magnitude. The rapid (mostly <1 ms) relaxation constant may also give insight into why blue (ionized) emissions are only seen briefly near the beginning of sprite optical signals.
- A comparison between the experimentally determined spatial extents of elves and a model of the lightning electromagnetic pulse interaction with the lower ionosphere suggests that the heating effect is often easily large enough to include >200 km regions of enhanced ionization.

Remote sensing of the electric field

In addition, an unexpected new method of remotely sensing the electric field within sprites was found when bright optical pulses were seen to relax exponentially. For a vertically narrow field-of-view for which the optical source altitude can be well constrained, the relaxation time constant may be related directly to the electric field by the curve $\nu_{\mathrm{i}} - \nu_{\mathrm{a}}$ in Figure 2-4. This technique could be combined with the broadband two-color photometric method described in Section 4.5, which does not rely on the detection of weak ionized lines but does also require a well constrained viewing elevation angle in order to determine the electric field at the source.

Discrimination of 1 ms flashes

Following distant, strong cloud-to-ground lightning, at least three classes of optical emissions are observed to have characteristic durations of ∼1 ms. These are scattered lightning flashes, elves, and the diffuse upper portion of sprites, observed as sprite halos. In addition, further sprite development (with streamer breakdown) may be observed to occur for several to many milliseconds.

Telltale signatures of elves, Rayleigh-scattered lightning flashes, and sprites were determined for the Fly's Eye photometric array and used to discriminate between these phenomena and to correctly associate them with their physical causes. Photometry with the Fly's Eye is a robust and sensitive method for identifying elves and determining their horizontal extent and lowest altitude extent.

In addition, the distinction between video signatures of elves and sprite halos was elucidated for the first time, based on measurements from a high speed image-intensified video system. In these measurements sprite halos are observed as a transient descending glow with lateral extent on the order of 40 to 70 km preceding the development of streamer structures at lower altitudes. These characteristics agree well with recent theoretical analysis of electrical breakdown properties at different altitudes [*Pasko et al.*, 1998a], previous sprite modeling using the quasi-electrostatic (QE) model [*Pasko et al.*, 1997b], and our one-to-one fully electromagnetic modeling of sprite driving fields and optical emissions for the observed events.

The introductory comment of *Barrington-Leigh and Inan* [1999] that "video recordings at standard frame rate are an inefficient and sometimes confusing method for identifying elves in comparison with a photometric array" seems now to be even more compelling given the common misidentification of sprite halos. In addition, high temporal resolution is clearly needed for both horizontal and vertical photometer arrays to discriminate between elves and sprite halos.

Verification of theoretical models

Asymmetries previously observed in the polarity of lightning seen to cause elves and sprites contradicted several of the predictions for the EMP and conventional breakdown QE models.

The bias of elves' occurrence towards an association with cloud-to-ground lighting of positive polarity likely disappears when lightning statistics are taken into account and a fair triggering method is used for data acquisition. Indeed, the correspondence between occurrence and optical intensity of elves is shown in Section 4.2 to be fully consistent with the lightning electromagnetic pulse model.

The observation of at least two "negative sprites" shows that conventional, rather than relativistic runaway, breakdown is responsible for the discharge in (at least some) sprites. This observation further suggests that the rarity of negative sprites may result primarily from a rarity of large charge moment changes in association with negative cloud-to-ground lightning. *Pasko et al.* [2000] has recently quantified the slight asymmetry expected between positive and negative streamers forming sprites.

Ubiquity of sprites and elves

The importance of sprites and elves in chemical, charge, and energy balances of global scale is still under investigation. In this work elves were shown to be a ubiquitous phenomenon, not likely to be restricted to large mesoscale convective systems in the way that sprites may be. In addition, elves may cause significant cumulative modification to the nighttime electron density profile near 90 km altitude over large regions of thunderstorm activity.

While negative sprites are reported as a rare event by *Barrington-Leigh et al.* [1999a], occurrence of the sprite halos reported here is not unusual in association with −CGs, based on Fly's Eye and normal-rate video observations (e.g., Figure 5-1). Due to the exponential reduction with altitude of the fields required for ionization and optical excitation, the diffuse region is easier to excite with lower driving fields (i.e., lower thundercloud charge moment changes). It may be more frequently excited by strong negative lightning even though negative strokes do not often carry long-duration continuing currents. Sprite campaigns which are focused on storms producing strong positive cloud-to-ground strokes may not adequately account for the occurrence of what one may call "negative sprite halos."

6.2 Further Research

Below we conclude by outlining some promising future investigations which follow from work detailed in this dissertation.

Three-dimensional modeling of VLF propagation past diffuse sprite regions: Early/fast events

As discussed in Section 2.5.2, the nature of the ionospheric disturbances causing early/fast VLF phase and amplitude changes following cloud-to-ground lightning is still under debate. Our suggestion that modeled ionization changes in observed sprite halos may produce such VLF perturbations with characteristics similar to recorded events can easily be addressed more quantitatively using available models of VLF scattering [*Poulsen et al.*, 1993].

Telescopic high-speed video

Recent high-speed video observation of sprite filamentary development [*Stanley et al.*, 1999] suggests that the apparent continuous filaments often visible in 17 ms video fields may in fact be due to temporal integration of short propagating streamer heads.

Photometers bore-sighted on a video system will accurately record the duration of optical emission of a new streamer channel, but not necessarily resolve whether it glows only during development or persists after the initial breakdown. Recent telescopic video observations [*Gerken et al.*, 1998, 2000] reveal a number of poorly understood features such as "beads", rebrightening regions, and sharply truncated columns in high spatial resolution. An obvious strategy for simultaneously resolving time and spatial scales comparable to those of the development of some of these phenomena [*Stanley et al.*, 1999] is to combine the proven telescopic and high speed techniques. For instance, a high speed camera operated at 4000 frames per second with a 0.7° vertical field-of-view can resolve streamer propagation with velocities between 2×10^5 m/s and 2×10^7 m/s at a range of 500 km. Cameras with variable exposure times shorter than the frame rate are also available now, allowing for "strobe" imagery of streamer propagation and sprite development. High resolution imaging studies may also be applied to negative sprites in order to compare their fine structure to that of positive sprites.

Multi-anode photometric arrays

Since the Fly's Eye's design in 1995, new technology has become available which is perfectly suited to the construction of a photometric array without multiple optics and separately sighted photometers. These multi-anode photomultipliers are available as linear arrays and square arrays of up to 16 or 64 elements. With a single set of optics and a multi-anode photomultiplier, crude imagery could be obtained continuously at rates up to 10^6 s^{-1}. Vertical arrays of this design have been operated since 1996 [*Fukunishi et al.*, 1996a, 1998].

A pair of vertical arrays with fields-of-view of $\sim 4^\circ \times 0.5^\circ$ and two optical filters similar to the red and blue filters used on the Fly's Eye would be well suited to studies of bright sprites exhibiting an exponential optical relaxation. A narrow vertical field-of-view is crucial in constraining the elevation angle used to account for the effects of atmospheric scattering, and in constraining the source altitude for determination of the electric field associated with a measured relaxation time constant. The combination of these techniques could prove complimentary for remotely sensing sprite electric fields and could serve as a powerful probe of the energetics of sprites at high time resolution. Sprite halos could also be resolved and their relationship to any initial pulse in blue emissions could be investigated.

In addition it may be interesting to deploy such a system, possibly oriented as a horizontal rather than vertical array, in a study of storms which have not necessarily been selected as sprite-producing candidates. This effort could help to assess the prevalence of (negative) sprite halos (as well as elves) on a global scale.

Bibliography

Armstrong, R., J. Shorter, M. Taylor, D. Suszcynsky, W. Lyons, and L. Jeong, Photometric measurements in the SPRITES '95 and '96 campaigns of nitrogen second positive (399.8 nm) and first negative (427.8 nm) emissions, *Journal of Atmospheric and Solar-Terrestrial Physics*, *60*, 787–99, 1998a.

Armstrong, R., D. Suszcynsky, W. Lyons, and T. Nelson, Multi-color photometric measurements of ionization and energies in sprites, *Geophysical Research Letters*, *27*, 653–6, 2000.

Armstrong, R. A., D. M. Suszcynsky, R. Strabley, W. A. Lyons, and T. Nelson, Simultaneous Multi-Color Photometric and Video Recording of SPRITES and their parent lightning mechanisms and energy deposition, *EOS Supplement*, *79*, F165, 1998b, fall AGU 1998, A41C-10 talk.

Barrington-Leigh, C., and U. Inan, Elves triggered by positive and negative lightning discharges, *Geophysical Research Letters*, *26*, 683–6, 1999.

Barrington-Leigh, C., U. Inan, M. Stanley, and S. Cummer, Sprites triggered by negative lightning discharges, *Geophysical Research Letters*, *26*, 3605–8, 1999a.

Barrington-Leigh, C. P., U. S. Inan, and M. Stanley, Elves: Photometric and Video Signatures, in *EOS Supplement*, vol. 80, p. F224, 1999b.

Barrington-Leigh, C. P., U. S. Inan, and M. Stanley, Identification of Sprites and Elves with Intensified Video and Broadband Array Photometry, *Journal of Geophysical Research*, in press, 2000.

Bazelyan, E. M., and Y. P. Raizer, *Spark Discharge*, CRC Press, Boca Raton, 1998.

Bell, T., S. Reising, and U. Inan, Intense continuing currents following positive cloud-to-ground lightning associated with red sprites, *Geophysical Research Letters*, *25*, 1285–8, 1998.

Bevington, P. R., and D. K. Robinson, *Data Reduction and Error Analysis for the Physical Sciences*, 2nd ed., McGraw-Hill, Inc., 1992.

Bickel, J., J. Ferguson, and G. Stanley, Experimental observation of magnetic field effects on VLF propagation at night, *Radio Science*, *5*, 19–25, 1970.

Boccippio, D., E. Williams, S. Heckman, W. Lyons, I. Baker, and R. Boldi, Sprites, ELF transients, and positive ground strokes, *Science*, *269*, 1088–91, 1995.

Boeck, W., J. Vaughan, O.H., R. Blakeslee, B. Vonnegut, and M. Brook, Lightning induced brightening in the airglow layer, *Geophysical Research Letters*, *19*, 99–102, 1992.

Boeck, W., J. Vaughan, O.H., R. Blakeslee, B. Vonnegut, M. Brook, and J. McKune, Observations of lightning in the stratosphere, *Journal of Geophysical Research*, *100*, 1465–75, 1995.

Boeck, W., J. Vaughan, O.H., R. Blakeslee, B. Vonnegut, and M. Brook, The role of the space shuttle videotapes in the discovery of sprites, jets and elves, *Journal of Atmospheric and Solar-Terrestrial Physics*, *60*, 669–77, 1998.

Budden, K., *Propagation of radio waves. The theory of radio waves of low power in the ionosphere and magnetosphere*, Cambridge, Cambridge, UK, 1985.

Chalmers, J. A., *Atmospheric Electricity*, 2nd ed., Pergamon Press, 1967.

Chamberlain, J. W., *Theory of planetary atmospheres*, Academic Press, New York, 1978.

Chapman, B. N. (Ed.), *Glow discharge processes*, John Wiley & Sons, 1980.

Charman, W., and J. Jelley, A search for pulses of fluorescence produced by supernovae in the upper atmosphere, *Journal of Physics A (Mathematical and General)*, *5*, 773–80, 1972.

Cho, M., and M. Rycroft, Computer simulation of the electric field structure and optical emission from cloud-top to the ionosphere, *Journal of Atmospheric and Solar-Terrestrial Physics*, *60*, 871–88, 1998.

Cummer, S., and U. Inan, Measurement of charge transfer in sprite-producing lightning using ELF radio atmospherics, *Geophysical Research Letters*, *24*, 1731–4, 1997.

Cummer, S., and M. Stanley, Submillisecond resolution lightning currents and sprite development: observations and implications, *Geophysical Research Letters*, *26*, 3205–8, 1999.

Cummer, S., U. Inan, and T. Bell, Ionospheric D region remote sensing using VLF radio atmospherics, *Radio Science*, *33*, 1781–92, 1998a.

Cummer, S., U. Inan, T. Bell, and C. Barrington-Leigh, ELF radiation produced by electrical currents in sprites, *Geophysical Research Letters*, *25*, 1281–4, 1998b.

Cummer, S. A., Lightning and ionospheric remote sensing using VLF/ELF radio atmospherics, Ph.D. dissertation, Stanford University, 1997.

Cummer, S. A., and U. S. Inan, Modeling ELF radio atmospheric propagation and extracting lightning currents from ELF observations, *Radio Science*, *35*, 385–94, 2000.

Cummins, K., E. Krider, and M. Malone, The US National Lightning Detection Network/sup TM/ and applications of cloud-to-ground lightning data by electric power utilities, *IEEE Transactions on Electromagnetic Compatibility*, *40*, 465–80, 1998a.

Cummins, K., M. Murphy, E. Bardo, W. Hiscox, R. Pyle, and A. Pifer, A combined TOA/MDF technology upgrade of the U.S. National Lightning Detection Network, *Journal of Geophysical Research*, *103*, 9035–44, 1998b.

Dhali, S., and P. Williams, Numerical simulation of streamer propagation in nitrogen at atmospheric pressure, *Physical Review A (General Physics)*, *31*, 1219–21, 1985.

Dowden, R., J. Brundell, and W. Lyons, Are VLF rapid onset, rapid decay perturbations produced by scattering off sprite plasma?, *Journal of Geophysical Research*, *101*, 19,175–83, 1996.

Dowden, R., S. Hardman, C. Rodger, and J. Brundell, Logarithmic decay and Doppler shift of plasma associated with sprites, *Journal of Atmospheric and Solar-Terrestrial Physics*, *60*, 741–53, 1998.

Erlick, C., and J. Frederick, Effects of aerosols on the wavelength dependence of atmospheric transmission in the ultraviolet and visible. 2. Continental and urban aerosols in clear skies, *Journal of Geophysical Research*, *103*, 23,275–85, 1998.

Farrell, W., and M. Desch, Cloud-to-stratosphere lightning discharges: a radio emission model, *Geophysical Research Letters*, *19*, 665–8, 1992.

Fernsler, R., and H. Rowland, Models of lightning-produced sprites and elves, *Journal of Geophysical Research*, *101*, 29,653–62, 1996.

Feynman, R. P., R. B. Leighton, and M. L. Sands, Electricity in the Atmosphere, in *The Feynman Lectures on Physics*, vol. 2, Addison-Wesley, Redwood City, Calif, 1989.

Fishman, G., et al., Discovery of intense gamma-ray flashes of atmospheric origin, *Science*, *264*, 1313–16, 1994.

Franz, R., R. Nemzek, and J. Winckler, Television image of a large upward electrical discharge above a thunderstorm system, *Science*, *249*, 48–51, 1990.

Fukunishi, H., Y. Takahashi, M. Fujito, Y. Watanabe, and K. Sakanoi, Fast imaging of elves and sprites using a framing / streak camera and a multi-anode array photometer, in *EOS Supplement*, vol. 77, p. F60, 1996a, fall AGU Meeting Abstracts.

Fukunishi, H., Y. Takahashi, M. Kubota, K. Sakanoi, U. Inan, and W. Lyons, Elves: lightning-induced transient luminous events in the lower ionosphere, *Geophysical Research Letters*, *23*, 2157–60, 1996b.

Fukunishi, H., Y. Takahashi, M. Sato, A. Shone, M. Fujito, and Y. Watanabe, Ground-based observations of ULF transients excited by strong lightning discharges producing elves and sprites, *Geophysical Research Letters*, *24*, 2973–6, 1997.

Fukunishi, H., Y. Takahashi, Y. Watanabe, A. Uchida, M. Sato, and W. A. Lyons, Frequent Occurrences of Elves Discovered by Array Photometer Observations, *EOS Supplement*, *79*, F164, 1998, fall AGU 1998, A41C-03 talk.

Gerken, E. A., U. S. Inan, C. P. Barrington-Leigh, and M. Stanley, Results from a New Telescopic Imager: A Survey of Sprite Structures, *EOS Supplement*, *79*, F137, 1998, a31A-16.

Gerken, E. A., U. S. Inan, and C. P. Barrington-Leigh, Telescopic imaging of sprites, *Geophysical Research Letters*, *27*, 2637–40, 2000.

Glukhov, V., and U. Inan, Particle simulation of the time-dependent interaction with the ionosphere of rapidly varying lightning EMP, *Geophysical Research Letters*, *23*, 2193–6, 1996.

Glukhov, V., V. Pasko, and U. Inan, Relaxation of transient lower ionospheric disturbances caused by lightning-whistler-induced electron precipitation bursts, *Journal of Geophysical Research*, *97*, 16,971–9, 1992.

Goldstein, H., *Classical Mechanics*, 2nd ed., Addison Wesley, 1980.

Green, B., et al., Molecular excitation in sprites, *Geophysical Research Letters*, *23*, 2161–4, 1996.

Guo, C., and E. Krider, The optical and radiation field signatures produced by lightning return strokes, *Journal of Geophysical Research*, *87*, 9813–22, 1982.

Hampton, D., M. Heavner, E. Wescott, and D. Sentman, Optical spectral characteristics of sprites, *Geophysical Research Letters*, *23*, 89–92, 1996.

Heavner, M. J., Optical spectroscopic observations of sprites, blue jets, and elves: Inferred microphysical processes and their macrophysical implications, Ph.D. dissertation, University of Alaska Fairbanks, 2000.

Heavner, M. J., et al., Ionization in Sprites, *EOS Supplement*, *79*, F165, 1998, fall AGU 1998, A41C-12 talk.

Huang, E., E. Williams, R. Boldi, S. Heckman, W. Lyons, M. Taylor, T. Nelson, and C. Wong, Criteria for sprites and elves based on Schumann resonance observations, *Journal of Geophysical Research*, *104*, 16,943–64, 1999.

Inan, U., VLF heating of the lower ionosphere, *Geophysical Research Letters*, *17*, 729–32, 1990.

Inan, U., D. Shafer, W. Yip, and R. Orville, Subionospheric VLF signatures of nighttime D region perturbations in the vicinity of lightning discharges, *Journal of Geophysical Research*, *93*, 11,455–72, 1988.

Inan, U., T. Bell, and J. Rodriguez, Heating and ionization of the lower ionosphere by lightning, *Geophysical Research Letters*, *18*, 705–8, 1991.

Inan, U., J. Rodriguez, and V. Idone, VLF signatures of lightning-induced heating and ionization of the nighttime D-region, *Geophysical Research Letters*, *20*, 2355–8, 1993.

Inan, U., T. Bell, V. Pasko, D. Sentman, E. Wescott, and W. Lyons, VLF signatures of ionospheric disturbances associated with sprites, *Geophysical Research Letters*, *22*, 3461–4, 1995.

Inan, U., V. Pasko, and T. Bell, Sustained heating of the ionosphere above thunderstorms as evidenced in "early/fast" VLF events, *Geophysical Research Letters*, *23*, 1067–70, 1996a.

Inan, U., S. Reising, G. Fishman, and J. Horack, On the association of terrestrial gamma-ray bursts with lightning and implications for sprites, *Geophysical Research Letters*, *23*, 1017–20, 1996b.

Inan, U., W. Sampson, and Y. Taranenko, Space-time structure of optical flashes and ionization changes produced by lightning-EMP, *Geophysical Research Letters*, *23*, 133–6, 1996c.

Inan, U., A. Slingeland, V. Pasko, and J. Rodriguez, VLF and LF signatures of mesospheric/lower ionospheric response to lightning discharges, *Journal of Geophysical Research*, *101*, 5219–38, 1996d.

Inan, U., C. Barrington-Leigh, S. Hansen, V. Glukhov, T. Bell, and R. Rairden, Rapid lateral expansion of optical luminosity in lightning-induced ionospheric flashes referred to as elves', *Geophysical Research Letters*, *24*, 583–6, 1997.

Inan, U. S., and A. S. Inan, *Engineering Electromagnetics*, Addison-Wesley, 1999.

Jacoby, G., D. Hunter, and C. Christian, A library of stellar spectra, *Astrophysical Journal Supplement Series*, *56*, 257–81, 1984.

Johnson, H., and R. Mitchell, Thirteen-color photometry of 1380 bright stars, *Revista Mexicana de Astronomia y Astrofisica*, *1*, 299–324, 1975.

Johnson, M., U. Inan, S. Lev-Tov, and T. Bell, Scattering pattern of lightning-induced ionospheric disturbances associated with early/fast VLF events, *Geophysical Research Letters*, *26*, 2363–6, 1999.

Jordan, E. C., and K. G. Balmain, *Electromagnetic Waves and Radiating Systems*, 2nd ed., Prentice Hall, 1968.

Krider, E., On the electromagnetic fields, Poynting vector, and peak power radiated by lightning return strokes, *Journal of Geophysical Research*, *97*, 15,913–17, 1992.

Landolt, H., and K. H. Hellwege, *Numerical data and functional relationships in science and technology. Comprehensive index for 6th edition 1950-1980 and New series 1961-1985*, Springer-Verlag, 1987.

Lauben, D., U. Inan, and T. Bell, Poleward-displaced electron precipitation from lightning-generated oblique whistlers, *Geophysical Research Letters*, *26*, 2633–6, 1999.

Lehtinen, N., T. Bell, V. Pasko, and U. Inan, A two-dimensional model of runaway electron beams driven by quasi-electrostatic thundercloud fields, *Geophysical Research Letters*, *24*, 2639–42, 1997.

Lehtinen, N., T. Bell, and U. Inan, Monte Carlo simulation of runaway MeV electron breakdown with application to red sprites and terrestrial gamma ray flashes, *Journal of Geophysical Research*, *104*, 24,699–712, 1999.

Lehtinen, N. G., Relativistic runaway electrons above thunderstorms, Ph.D. dissertation, Stanford University, 2000.

Li, Y. Q., R. H. Holzworth, H. Hu, M. McMarthy, R. D. Massey, P. M. Kintner, J. V. Rodriguez, U. S. Inan, and W. C. Armstrong, Anomalous Optical Events Detected by Rocket-Borne Sensor in the WIPP Campaign, *Journal of Geophysical Research*, *96*, 1315–1326, 1991.

Llewellyn-Jones, F., *The Glow Discharge*, Methuen & Co., 1966.

Lyons, W., Characteristics of luminous structures in the stratosphere above thunderstorms as imaged by low-light video, *Geophysical Research Letters*, *21*, 875–8, 1994.

Lyons, W., Sprite observations above the U.S. High Plains in relation to their parent thunderstorm systems, *Journal of Geophysical Research*, *101*, 29,641–52, 1996.

Lyons, W., M. Uliasz, and T. Nelson, Large peak current cloud-to-ground lightning flashes during the summer months in the contiguous United States, *Monthly Weather Review*, *126*, 2217–33, 1998.

Marshall, T., M. Stolzenburg, and W. Rust, Electric field measurements above mesoscale convective systems, *Journal of Geophysical Research*, *101*, 6979–96, 1996.

Meek, J. M., and J. D. Craggs (Eds.), *Electrical Breakdown of Gases*, John Wiley & Sons, 1978.

Mende, S., R. Rairden, G. Swenson, and W. Lyons, Sprite spectra; N_2 1 PG band identification, *Geophysical Research Letters*, *22*, 2633–6, 1995.

Milikh, G., K. Papadopoulos, and C. Chang, On the physics of high altitude lightning, *Geophysical Research Letters*, *22*, 85–8, 1995.

Milikh, G., J. Valdivia, and K. Papadopoulos, Model of red sprite optical spectra, *Geophysical Research Letters*, *24*, 833–6, 1997.

Milikh, G., J. Valdivia, and K. Papadopoulos, Spectrum of red sprites, *Journal of Atmospheric and Solar-Terrestrial Physics*, *60*, 907–15, 1998.

Montenbruck, O., and T. Pfleger, *Astronomy on the personal computer*, SDpringer-Verlag, Berlin, Germany, 1998.

Morrill, J., E. Bucsela, V. Pasko, S. Berg, M. Heavner, D. Moudry, W. Benesch, E. Wescott, and D. Sentman, Time resolved N_2 triplet state vibrational populations and emissions associated with red sprites, *Journal of Atmospheric and Solar-Terrestrial Physics*, *60*, 811–29, 1998.

Nemiroff, R., J. Bonnell, and J. Norris, Temporal and spectral characteristics of terrestrial gamma flashes, *Journal of Geophysical Research*, *102*, 9659–65, 1997.

Nemzek, R., and J. Winckler, Observation and interpretation of fast sub-visual light pulses from the night sky, *Geophysical Research Letters*, *16*, 1015–18, 1989.

Ogelman, H., Millisecond time scale atmospheric light pulses associated with solar and magnetospheric activity, *Journal of Geophysical Research*, *78*, 3033–9, 1973.

Orville, R., Cloud-to-ground lightning flash characteristics in the contiguous United States: 1989-1991, *J. Geophys. Res. (USA), Journal of Geophysical Research*, *99*, 10,833–41, 1994.

Pasko, V., U. Inan, Y. Taranenko, and T. Bell, Heating, ionization and upward discharges in the mesosphere due to intense quasi-electrostatic thundercloud fields, *Geophysical Research Letters*, *22*, 365–8, 1995.

Pasko, V., U. Inan, and T. Bell, Blue jets produced by quasi-electrostatic pre-discharge thundercloud fields, *Geophysical Research Letters*, *23*, 301–4, 1996a.

Pasko, V., U. Inan, and T. Bell, Sprites as luminous columns of ionization produced by quasi-electrostatic thundercloud fields, *Geophysical Research Letters*, *23*, 649–52, 1996b.

Pasko, V., U. Inan, and T. Bell, Sprites as evidence of vertical gravity wave structures above mesoscale thunderstorms, *Geophysical Research Letters*, *24*, 1735–8, 1997a.

Pasko, V., U. Inan, T. Bell, and Y. Taranenko, Sprites produced by quasi-electrostatic heating and ionization in the lower ionosphere, *Journal of Geophysical Research*, *102*, 4529–61, 1997b.

Pasko, V., U. Inan, and T. Bell, Spatial structure of sprites, *Geophysical Research Letters*, *25*, 2123–6, 1998a.

Pasko, V., U. Inan, T. Bell, and S. Reising, Mechanism of ELF radiation from sprites, *Geophysical Research Letters*, *25*, 3493–6, 1998b.

Pasko, V., U. Inan, and T. Bell, Thermal runaway electrons in sprites, in *1999 URSI National Radio Science Meeting, Program and Abstracts*, p. 152, Boulder, Colorado, 1999a.

Pasko, V., U. Inan, and T. Bell, Mesospheric electric field transients due to tropospheric lightning discharges, *Geophysical Research Letters*, *26*, 1247–50, 1999b.

Pasko, V., U. Inan, and T. Bell, Fractal structure of sprites, *Geophysical Research Letters*, *27*, 497–500, 2000.

Poulsen, W., T. Bell, and U. Inan, The scattering of VLF waves by localized ionospheric disturbances produced by lightning-induced electron precipitation, *Journal of Geophysical Research*, *98*, 15,553–9, 1993.

Rairden, R., and S. Mende, Time resolved sprite imagery, *Geophysical Research Letters*, *22*, 3465–8, 1995.

Raizer, Y., G. Milikh, M. Shneider, and S. Novakovski, Long streamer in the upper atmosphere above thundercloud, *Journal of Physics D (Applied Physics)*, *31*, 3255–64, 1998.

Rees, J. A. (Ed.), *Electrical Breakdown in Gases*, John Wiley & Sons, 1973.

Reising, S., U. Inan, T. Bell, and W. Lyons, Evidence for continuing current in sprite-producing cloud-to-ground lightning, *Geophysical Research Letters*, *23*, 3639–42, 1996.

Reising, S., U. Inan, and T. Bell, ELF sferic energy as a proxy indicator for sprite occurrence, *Geophysical Research Letters*, *26*, 987–90, 1999.

Rodger, C., Red sprite, upward lightning, and VLF perturbations, *Reviews of Geophysics*, *37*, 317–36, 1999.

Rodriguez, J., U. Inan, and T. Bell, D region disturbances caused by electromagnetic pulses from lightning, *Geophysical Research Letters*, *19*, 2067–70, 1992.

Roussel-Dupre, R., and E. Blanc, HF echoes from ionization potentially produced by high-altitude discharges, *Journal of Geophysical Research*, *102*, 4613–22, 1997.

Roussel-Dupre, R., and A. Gurevich, On runaway breakdown and upward propagating discharges, *Journal of Geophysical Research*, *101*, 2297–311, 1996.

Roussel-Dupre, R., E. Symbalisty, Y. Taranenko, and V. Yukhimuk, Simulations of high-altitude discharges initiated by runaway breakdown, *Journal of Atmospheric and Solar-Terrestrial Physics*, *60*, 917–40, 1998.

Rowland, H., Theories and simulations of elves, sprites and blue jets, *Journal of Atmospheric and Solar-Terrestrial Physics*, *60*, 831–44, 1998.

Rowland, H., R. Fernsler, J. Huba, and P. Bernhardt, Lightning driven EMP in the upper atmosphere, *Geophysical Research Letters*, *22*, 361–4, 1995.

Rowland, H., R. Fernsler, and P. Bernhardt, Breakdown of the neutral atmosphere in the D region due to lightning driven electromagnetic pulses, *Journal of Geophysical Research*, *101*, 7935–45, 1996.

Sampath, H., U. Inan, and M. Johnson, Recovery signatures and occurrence properties of lightning-associated subionospheric VLF perturbations, *Journal of Geophysical Research*, *105*, 183–91, 2000.

Sentman, D., and E. Wescott, Observations of upper atmospheric optical flashes recorded from an aircraft, *Geophysical Research Letters*, *20*, 2857–60, 1993.

Sentman, D., and E. Wescott, Red sprites and blue jets: thunderstorm-excited optical emissions in the stratosphere, mesosphere, and ionosphere, *Phys. Plasmas (USA), Physics of Plasmas*, *2*, 2514–22, 1995.

Sentman, D., E. Wescott, D. Osborne, D. Hampton, and M. Heavner, Preliminary results from the Sprites94 aircraft campaign. 1. Red sprites, *Geophysical Research Letters*, *22*, 1205–8, 1995.

Sipler, D., and M. Biondi, Measurements of O(^{1}D) quenching rates in the F-region, *Journal of Geophysical Research*, *77*, 6202–12, 1972.

Stanley, M., P. Krehbiel, M. Brook, C. Moore, W. Rison, and B. Abrahams, High speed video of initial sprite development, *Geophysical Research Letters*, *26*, 3201–4, 1999.

Stanley, M., M. Brook, P. Krehbiel, and S. Cummer, Detection of daytime sprites via a unique sprite ELF signature, *Geophysical Research Letters*, *27*, 871–4, 2000.

Stanley, M. A., Sprites and their Parent Discharges, Ph.D. dissertation, New Mexico Institute of Mining and Technology, 2000.

Stanton, P., and R. St John, Electron excitation of the first positive bands of N_2 and of the first negative and Meinel bands of ${N_2}^+$, *Journal of the Optical Society of America*, *59*, 252–60, 1969.

Sturrock, P. A., *Plasma Physics: an introduction to the theory of astrophysical, geophysical, and laboratory plasmas*, Cambridge University Press, 1994.

Sukhorukov, A., E. Rudenchik, and P. Stubbe, Simulation of the strong lightning pulse penetration into the lower ionosphere, *Geophysical Research Letters*, *23*, 2911–14, 1996.

Suszcynsky, D., R. Roussel-Dupre, W. Lyons, and R. Armstrong, Blue-light imagery and photometry of sprites, *Journal of Atmospheric and Solar-Terrestrial Physics*, *60*, 801–9, 1998.

Taflove, A., *Computational Electrodynamics: The Finite-Difference Time-Domain Method*, Artech House, Inc., 1995.

Taranenko, Y., and R. Roussel-Dupre, High altitude discharges and gamma-ray flashes: a manifestation of runaway air breakdown, *Geophysical Research Letters*, *23*, 571–4, 1996.

Taranenko, Y., U. Inan, and T. Bell, Optical signatures of lightning-induced heating of the D region, *Geophysical Research Letters*, *19*, 1815–18, 1992.

Taranenko, Y., U. Inan, and T. Bell, Interaction with the lower ionosphere of electromagnetic pulses from lightning: heating, attachment, and ionization, *Geophysical Research Letters*, *20*, 1539–42, 1993a.

Taranenko, Y., U. Inan, and T. Bell, The interaction with the lower ionosphere of electromagnetic pulses from lightning: excitation of optical emissions, *Geophysical Research Letters*, *20*, 2675–8, 1993b.

Taranenko, Y., R. Roussel-Dupre, V. Yukhimuk, and E. Symbalisty, Generation of elves by sprites and jets, in *XXIII International Conference on Phenomena in Ionized Gases, ICPIGProceedings. Contributed Papers*, pp. 8–9 vol.3, 1997.

Thomason, L., and E. Krider, The effects of clouds on the light produced by lightning, *Journal of the Atmospheric Sciences*, *39*, 2051–65, 1982.

Tsunoda, R., R. Livingston, J. Buonocore, W. Lyons, T. Nelson, and M. Kelley, Evidence of a high-altitude discharge process responsible for radar echoes at 24.4 MHz, *Journal of Atmospheric and Solar-Terrestrial Physics*, *60*, 957–64, 1998.

Uchida, A., Y. Takahashi, H. Fukunishi, and W. A. Lyons, Energies of electrons for inducing elves estimated from N_2 1P/2P ratio observation, in *EOS Supplement*, vol. 80, p. F225, 1999.

Uman, M., *Lightning discharge*, Academic Press, London, UK, 1987.

Vaughan, J., O. H., and B. Vonnegut, Recent observations of lightning discharges from the top of a thundercloud into the clear air above, *Geophysical Research Letters*, *94*, 13,179, 1989.

Veronis, G., V. Pasko, and U. Inan, Characteristics of mesospheric optical emissions produced by lightning discharges, *Journal of Geophysical Research*, *104*, 12,645–56, 1999.

Wait, J. R., and K. P. Spies, Characteristics of the Earth-ionosphere waveguide for VLF radio waves, *Tech note 300*, National Bureau of Standards, Boulder, Colorado, 1964.

Watanabe, Y., A Study on Space-time Structures of Sprites based on Photometric Observations, Master's thesis, Tohoku University, 1999.

Wescott, E., D. Sentman, D. Osborne, D. Hampton, and M. Heavner, Preliminary results from the Sprites94 aircraft campaign. 2. Blue jets, *Geophysical Research Letters*, *22*, 1209–12, 1995.

Wescott, E., D. Sentman, M. Heavner, D. Hampton, W. Lyons, and T. Nelson, Observations of columniform' sprites, *Journal of Atmospheric and Solar-Terrestrial Physics*, *60*, 733–40, 1998.

Wescott, L. W., E. M. Wescott, H. C. Stenbaek-Nielsen, D. D. Sentman, D. R. Moudry, M. T. Heavner, and F. T. Sao Sabbas, Triangulation of sprites and elves from the NASA 1999 sprites balloon campaign, in *EOS Supplement*, vol. 80, p. F224, 1999.

Wettlaufer, J. S., and J. G. Dash, Melting below zero, *Scientific American (International Edition)*, *282*, 50–3, 2000.

Williams, E., The positive charge reservoir for sprite-producing lightning, *Journal of Atmospheric and Solar-Terrestrial Physics*, *60*, 689–92, 1998.

Wilson, C. T. R., The electric field of a thundercloud and some of its effects, *Proc. Phys. Soc. London*, *37*, 32D–37D, 1925.

Winckler, J., Further observations of cloud-ionosphere electrical discharges above thunderstorms, *Journal of Geophysical Research*, *100*, 14,335–45, 1995.

Winckler, J., Optical and VLF radio observations of sprites over a frontal storm viewed from O'Brien Observatory of the University of Minnesota, *Journal of Atmospheric and Solar-Terrestrial Physics*, *60*, 679–88, 1998.

Winckler, J., R. Franz, and R. Nemzek, Fast low-level light pulses from the night sky observed with the SKYFLASH program, *Journal of Geophysical Research*, *98*, 8775–83, 1993.

Winckler, J., W. Lyons, T. Nelson, and R. Nemzek, New high-resolution ground-based studies of sprites, *Journal of Geophysical Research*, *101*, 6997–7004, 1996.

Yukhimuk, V., R. Roussel-Dupre, E. Symbalisty, and Y. Taranenko, Optical characteristics of blue jets produced by runaway air breakdown, simulation results, *Geophysical Research Letters*, *25*, 3289–92, 1998.

Index